修士論文

# A spectroscopic study of dual quasars with the Hyper Suprime-Cam Subaru Strategic Survey (すばる望遠鏡HSCサーベイで観測された二重クェーサーの分光研究)

2020 年 08 月 13 日 提出


指導教員 相原　博昭 教授

東京大学理学系研究科 物理学専攻
35-186385 Shenli Tang

# Abstract

Galaxy mergers are thought to play an important role in the galaxy evolution scenario and the growth of supermassive black holes (SMBHs). For instance, they can trigger AGNs (Active Galactic Nuclei). Over the past decade, hydrodynamic simulations have been carried out to study the detailed physics during the merger and predict the occurrence of dual quasars in this co-evolution scenario. To check their results, systematic observations are required. The rich data from SDSS (Sloan Digital Sky Survey) has shed light on these studies with much success. However, spectroscopy from SDSS is limited by its fiber diameter, which is 3" for the earlier surveys and 2" for the later, the minimum fiber to fiber distance is 55". Although some closer pairs can be observed where plates overlapped, such area is limited. Therefore, close quasar pairs are still very rare in the literature.

In this work, taking the advantage of high image quality of HSC (Hyper Suprime Cam), we are able to find a large number of potential cases. We match the SDSS DR14 quasar catalog with HSC PDR2 catalog and find 34476 SDSS quasars that are imaged by HSC at redshift $0 - 5$. We then run an algorithm to select out possible dual quasar candidates which are those appear to have a companion source separated from the quasar by 0".6 $\sim$ 4". In total there are 452 such candidates. We reduce the sample size to 401 with further constrains, then followed the candidates up with spectroscopic observation using Keck/LRIS, Gemini/GMOS and Subaru/FOCAS to confirm their quasar origins. As a result, we identified 7 physically-associated quasar pairs (4 from Subaru and Gemini for this thesis), 2 projected quasar pairs and 2 quasar-galaxy pairs out of 33 observed candidates. With the addition of one more case based on spectra from SDSS, we report and provide detailed information on 5 newly discovered dual quasar systems. We discuss the physical properties of our sample, including their black hole mass, bolometric luminosity and Eddington ratio and compare to single quasars in SDSS DR7. We use the stellar masses, measured by team members, and assess the BH-host correlation in such systems. We compare our observational results with that of the Horizon-AGN simulation and find similar values of

the black hole mass and stellar mass of dual quasar systems. On the other hand, there were previous studies based on searches for double peaked [OIII] lines to systematically look for dual quasars. However, most of those features turn out to be formed by outflow. Among the dual quasars we find, we do not see such features.

# Contents

# List of Figures

# List of Tables

# Chapter 1

# Introduction

In this chapter, I summarize the construction and development of ideas in this field based on previous studies. Section 1.1 and 1.2 are general introductions to the concepts of AGN and BH-host coevolution, including physical descriptions with formulas that will be used in later chapters. Section 1.3 is a specific introduction on the work of this thesis: dual AGN. It is a topic constructed from the combination of AGN science, the relation of BHs to their host galaxies, and the tight relation of these two. Section 1.4 gives a guidance of the contents of this thesis.

## 1.1 What is an Active Galactic Nucleus (AGN)

AGN are the nuclei of galaxies which generate non-stellar emission in all wavebands from radio to gamma ray. A galaxy hosting an AGN is called an "active galaxy". The difference of active galaxies from normal galaxies is the presence of an accreting supermassive black hole (SMBH, black hole whose mass is larger than $10^6 M_\odot$) in their centers. It is estimated that at z $\leq 0.1$ (i.e. the local universe), about 1 out of 50 galaxies contains a fast-accreting SMBH and about one thirds contains a slowly accreting SMBH. AGN can generate huge amounts of energy (up to $10^4$ times of a normal galaxy) form a tiny region ($< 1\ pc^3$). The luminosity of ANGs may range from $10^{42}$ to $10^{48}$ erg/s depending on different types. The identification of an AGN is actually ambiguous, especially for the low luminosity ones. Observationally, we may classify an object as an AGN if at least one of the following is fulfilled [1]:

- It contains a compact nuclear region emitting significantly beyond what is expected from stellar processes typical of this type of galaxy.

- It shows the clear signature of a nonstellar continuum emitting process in its center.
- Its spectrum contains strong emission lines with line ratios that are typical of excitation by a nonstellar radition field or very broad emission lines (1000-25000 km $s^{-1}$) that are created by the centeral source at a vicinity region.
- It shows line and/or continuum variations.

Given this definition, the AGN family is not solid, an object can leave the AGN family, quench from an active galaxy to a normal galaxy, and new members may enter, activated via some physical processes from normal galaxy to active galaxy. These features are also used to classify AGN into more detailed groups like Seyfert galaxies, radio galaxies, BL Lac objects, LINERs (Low-Ionization Nuclear Emission-Line Region) and quasars.

### 1.1.1 AGN Structure: from Observation to Physics

From the full-waveband study, people have found many interesting features in AGN spectra, and they require different physical processes to explain. This section will discuss the main components that make up an AGN.

#### The Central Black Hole and Its Accretion Disk

The main component of an AGN is a supermassive black hole, the idea was born in 1964, right after the discovery of the first two quasars. Given their high redshifts, it is hard to explain the enormous luminosities of these quasars by ordinary stars only. Edwin Salpeter suggested that via accretion, a massive object ($> 10^6 M_\odot$, he did not directly say SMBH) may work as a power engine [16].

In 1969, Lynden-Bell suggested that nearby galaxies contain SMBHs at their centers as relics of "dead" quasars, and that black hole accretion was the power source for the non-stellar emission in nearby Seyfert galaxies [17]. Early X-ray astronomy at that time also supported this idea.

At 1973, Shakura and Sunyaev developed the disk model in detail, they suggested four possible shapes of the local spectrum of a disk depending on different physical process:

- Black body radiation: $Q = bT^4$, where b is Wien's displacement constant, equal to $2.897771955 \times 10^{-3}\ m\ K$
- Scattering of an isothermal, homogeneous medium: $Q = \text{const}\ \sqrt{n}T^{2.25}$

- Scattering of an isothermal, exponential medium: $Q = \text{const}\, T^{2.5}$
- Comptonization: $Q = \text{const}\, T^4$

Then they divided the disk into three regions: outer region dominated by black body radiation, intermediate region dominated by scattering and inner region dominated by comptonization. For each region, the temperature distribution of the disk can be calculated by the gravitational energy release $\frac{3}{8\pi}\frac{GM}{R^3}\dot{M}\left(1-\left(\frac{R_0}{R}\right)^{1/2}\right)$. Thus the spectrum generated by the whole disk will be the integral of local spectrum over the whole radius:

$$L_\nu = 4\pi \int_{R_0}^{R_1} F_\nu\left[T_s(R)\right] RdR \tag{1.1}$$

where $L_\nu$ is monochromatic luminosity [1], $R_0$ and $R_1$ correspond to the inner and outer boundary of the accretion disk, $F_\nu[T]$ is monochromatic flux at a certain temperature, $T_s(R)$ is the temperature at the certain position. This finally gives a form of:

$$L_\nu = \frac{16\pi^2 R_0^2 h}{c^2}\left(\frac{kT_0}{h}\right)^{8/3}\nu^\gamma \tag{1.2}$$

Therefore, the SED generated by the accretion disk is a power law, its index $\gamma$ depends on different physical conditions, for the black body case, $\gamma = \frac{1}{3}$. But the $\nu^{\frac{1}{3}}$ dependence only holds for a limited energy band roughly from 1 eV to 20 eV, below 1 eV, it follows a frequency dependency of $\nu^2$. Beyond 20 eV, it drops exponentially, which corresponds to the maximum disk temperature.

The total luminosity is then given by the integral of monochromatic luminosity: $L = \int_{v_1}^{v_2} \mathrm{I}_v dv$. For the optical waveband from 3000 Å to 10000 Å:

$$L_{\text{opt}} \simeq 10^{35} m^{4/3} \dot{m}^{2/3} \frac{\text{erg}}{\text{s}} \tag{1.3}$$

where $\dot{m}$ is the accretion rate of the black hole, in the unit of $M_\odot$/yr. For typical quasars, $\dot{m} \approx 2\ M_\odot$/yr, $m \approx 10^8\ M_\odot$, corresponding to $L \approx 10^{46}$ erg s$^{-1}$.

During the study of accretion, people also noticed that there is a mechanism to prevent the "overgrowth" of black hole, that is the Eddington limit. An object of luminosity $L$ will exert a force on a particle:

$$f_{\text{rad}} = \frac{N_e\sigma_T}{4\pi r^2 c}\int_0^\infty L_v dv = \frac{N_e L \sigma_T}{4\pi r^2 c} \tag{1.4}$$

[1] In the original paper, they use $I_\nu$, since the area has been considered, I think the letter L for luminosity is better than I for intensity

where $N_e$ is the electron density, $\sigma_T$ is the Thomson section, $L_v$ is monochromatic luminosity. On the other hand, the particle is also dragged by gravitational force:

$$f_g = \frac{GM\mu m_p N_e}{r^2} \tag{1.5}$$

where $\mu$ is the mean molecular weight (mean number of protons and neutrons per electron), $m_p$ is the proton mass. When $f_{\rm rad} = f_g$, this system reaches a balance, we call the luminosity at this balance as the Eddington luminosity:

$$L_{\rm Edd} = \frac{4\pi c G M \mu m_p}{\sigma_T} \simeq 1.5 \times 10^{38}\,(M/M_\odot)\,{\rm ergs}^{-1} \tag{1.6}$$

The factor $1.5\times10^{38}$ assumes $\mu$ as solar metallicity, it may vary a few depending on the exact case. Eddington luminosity is considered as the maximum luminosity allowed for an object to accrete stably over a long period of time. The corresponding accretion rate to produce Eddington luminosity is called Eddington accretion rate:

$$\dot{M}_{\rm Edd} = \frac{L_{\rm Edd}}{\eta c^2} \simeq 3M_8\left[\frac{\eta}{0.1}\right]^{-1} M_\odot y^{-1} \tag{1.7}$$

where $\eta$ is the energy conversion efficiency originated from $E = \eta mc^2$ and $L = \dot{E}$. usually we assume it to be 0.1 in the case of black hole accretion.

Actually, people do observe super-eddington luminosity among those massive stars, the density of those stars are usually low, thus their gravitational force at their out layers is relatively weak, this kind of stars will initiate very intense radiation-driven stellar wind from their outer layers. However, it appears to be rarer among SMBHs because of their stronger gravity in a much smaller region, thus most SMBHs are accreting at a moderate rate, we use the parameter "Eddington ratio" $\lambda_{\rm Edd}$ to describe the accretion state of a SMBH:

$$\lambda_{Edd} = \frac{L}{L_{Edd}} \propto \frac{\dot{M}}{\dot{M}_{Edd}} \propto \frac{\dot{M}}{M} \tag{1.8}$$

### Broad-line Region (BLR) and Narrow-line Region (NLR)

The emission lines in AGN spectrum are explained by the photoionization of the gas clouds surrounding the AGN. The simplest case is that central AGN transfers its energy to the gas via photoionization or absorption (when excited but not ionized), thus ionize an atom $X$ to $X^{+1}$, $X^{+2}$ etc, then the ion recombines with free electrons and emits a certain amount of energy depending on the state it jumps to. H is a typical case for this process, and stands for the most abundant element in AGN environment. That's why we see the strongest feature in the AGN optical/UV spectrum are the hydrogen lines like Ly$\alpha$, H$\beta$ and H$\alpha$.

The broadening of the line is due to differential Doppler shift from the bulk motions of the individual clouds and its profile usually follows gaussian distribution. But in type-I AGN, we find one gaussian component is not enough to describe the profiles of the hydrogen lines (see Mean quasar, Seyfert1 and BLRG spectrum in Figure 1.2, their Balmer lines seem to have "broad bases" besides a single gaussian distribution), indicating that there should be another region which is also made up of gas but at the different position, thus have different bulk velocity distribution. As these hydrogen lines can usually be fitted with one broad (width over 5000 $\mathrm{km\,s^{-1}}$) + one narrow component (width around 500 $\mathrm{km\,s^{-1}}$) quite well, we name these two regions of gas clouds as broad-line region (BLR) and narrow-line region (NLR).

However, the decay of an ion to a lower energy state is not equivalent for all energy levels, the selection rule in quantum mechanics decides some of the transitions are easier to happen (permitted) and some are harder (forbidden). In the case of LS (Russel-Saunders) coupling, the total angular momentum is given by J = L + S, where S is the total spin angular momentum and L is the total orbital angular momentum for all electrons. The configuration of the quantum numbers of an individual electron is written as ${}^{2S+1}L_J^{parity}$. The parity term is omitted for even parity and equals to 0 for odd. For a transition, if $\Delta J = 0, \pm 1$ except $0 \to 0$ & $\Delta L = 0, \pm 1$ except $0 \to 0$ & $\Delta S = 0$ & parity changes, it is permitted transition, if only $\Delta S = 0$ is violated, it is semiforbidden, otherwise it is forbidden. Take $O^{2+}$ as an example, the doublet 4959, 5007 are both transitions from ${}^1D$ to ${}^3P$, the parity doesn't change, therefore they are forbidden lines.

Note that forbidden doesn't mean that transition could not happen in anyway, but difficult to happen in the earth's environment. In the Earth's atmosphere, the excited atom would collide with other atoms or free electrons and lose energy in the collision long before it could radiate the energy away. However, in the low densities of cosmic environment, collisions are extremely rare and there is time for the spontaneous decay to occur.

Since we have known that the existence of forbidden lines are related to the density, we can use this property to estimate the density of the region. The [O III]$\lambda\lambda$4959,5007 doublet mentioned above is only observed with a width corresponding to the NLR but absent in BLR. We know the critical density for collisional de-excitation of [O III] is around $10^8$ $\mathrm{cm^{-3}}$, hence the density of BLR must be larger than this value, and the density of NLR smaller than this value.

On the other hand, the size of BLR can be estimated using the so-called reverberation mapping method. Time series studies show that type-I AGN always show optical-UV variations in such a pattern: the increase (decrease) of the luminosity of almost all broad emission lines often follows the increase (decrease) of the continuum luminosity. This time lag strongly supports the photoionization model, it is exactly the time for the photons to travel from one side of BRL to another side. The mechanism is shown in Figure 1.1. Assuming the BLR clouds are distributed along a circular orbit centering the AGN (point O) at inclination $i = 90°$ and orbiting counterclockwise, now there is an outburst in the central source, this signal will reach all the clouds at the same time on the orbit. For the clouds at point M, observers at the left side should see the enhancement in BLR at the same time as the enhancement in continuum, but for clouds at point A or any other position with an angle $\theta$ to the view of sight, the signal of BLR has to travel an additional path AC to reach the observers. This gives a time delay of $\tau =$ $(1 + \cos\theta)$r/c). The difference between A and B is that the light from A is blueshifted because it is approaching us on its orbit and the light from B is redshifted. Therefore, the largest time delay is given by clouds at point N, in that case, the additional path is $MN = 2r$ corresponding to a time delay of $2r/c$. The combination of the time delay and velocity of the BLR clouds at different position is plotted in panel B. For circular orbits with inclinations less than 90°, the axes of both of the ellipses are decreased by a factor sin$i$, thus all the inclination cases are limited by the $i = 90°$ case.

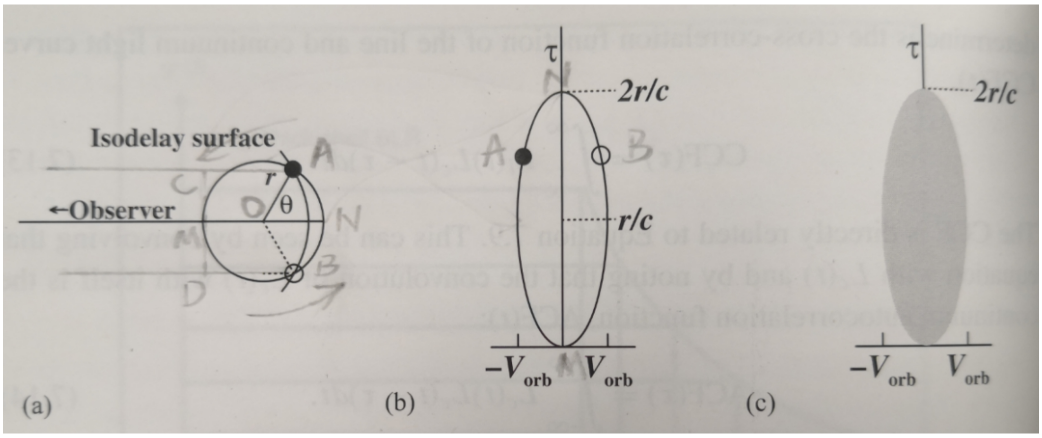


Fig. 1.1: Adopted from [1] Figure 7.8 right panel, labels added by me to help explanation. (a) An example of BLR clouds that are distributed along a circular orbit centered on the central continuum source at inclination $i = 90°$. (b) The points on the orbit plotted in the velovity-time delay space. (c) All the cases with inclination less than 90° are limited by $i = 90°$ case.

With this method, studies like [18] estimated the size of the BLR is approximately tens of lightdays. Later systematic studies of the RM samples suggested a correlation of the size of the BLR and the luminosity of the central source in a power law [19]

$$R_{BLR} = C_{BLR} L^{\alpha(BLR)} \tag{1.9}$$

This is a reasonable guess because as the central source being brighter, it will be able to ionize gas further away, thus making the emission line region larger in size. For H$\beta$, the fitting gives

$$R_{\mathrm{BLR}}(H\beta) \simeq 0.12 L_{46}^{0.6\pm0.1}\mathrm{pc} \tag{1.10}$$

where $L_{46}$ is the bolometric luminosity in units of $10^{46}$erg s$^{-1}$.
For C IV, the expression is

$$R_{\mathrm{BLR}}(C\,iv\lambda1549) \simeq 0.04 L_{46}^{0.6\pm0.1}\mathrm{pc} \tag{1.11}$$

We notice that the factor of C IV is smaller than H$\beta$, this is because the ionization energy of C IV is larger than H$\beta$, thus the C IV region must be closer to the central source to get ionized.

Assuming the system is virialized and individual clouds are moving in Keplerian orbits, we can combine the $R_{\mathrm{BLR}}$ and the velocity of the clouds $v_l$, which can be measured from the line profile, to estimate the black hole mass from Newtonian physics:

$$M_{\mathrm{BH}} = f\left(R_{\mathrm{BLR}}\right) \frac{R_{\mathrm{BLR}} v_l^2}{G} \mathrm{gr} \tag{1.12}$$

where $f\left(R_{\mathrm{BLR}}\right)$ is a geometrical-dynamical factor that depends on the distributions and inclination of the orbits to the line of sight. In reality, there is not enough information to determine $f\left(R_{\mathrm{BLR}}\right)$ form observational data, but fortunately, the $M_{\mathrm{BH}} - \sigma_*$ method (which will be discussed later) provides another independent way to measure the black hole mass. Using $M_\bullet$ from that method and $R_{\mathrm{BLR}}$ from RM method, we cam get an empirical value of $f\left(R_{\mathrm{BLR}}\right)$, thus obtain a practical relation between the black hole mass and velocity (usually use FWHM of the profile) based on equation equation(1.12). There are many studies trying to fit the parameters in this equation, in this thesis, for $H\beta$, we use the formula in [20]:

$$M_{\mathrm{BH}}(\mathrm{H}\beta) = 10^{6.91} \left(\frac{L_{5100}}{10^{44}\mathrm{ergs}^{-1}}\right)^{0.5} \left(\frac{\mathrm{FWHM}}{1000\mathrm{kms}^{-1}}\right)^{2} M_\odot \tag{1.13}$$

For H$\alpha$, we use the formula in [21]:

$$M_{\rm BH}({\rm H}\alpha) = 10^{6.71}\left(\frac{L_{\rm H\alpha}}{10^{42}{\rm ergs}^{-1}}\right)^{0.48}\left(\frac{\rm FWHM}{1000{\rm kms}^{-1}}\right)^{2.12} M_\odot \quad (1.14)$$

For Mg II, we use the formula in[14]:

$$M_{\rm BH}({\rm Mg\,ii}) = 10^{6.74}\left(\frac{L_{3000}}{10^{44}{\rm ergs}^{-1}}\right)^{0.62}\left(\frac{\rm FWHM}{1000{\rm kms}^{-1}}\right)^{2} M_\odot \quad (1.15)$$

For C IV, we use the formula in[20]:

$$M_{\rm BH}({\rm C\,iv}) = 10^{6.66}\left(\frac{L_{1350}}{10^{44}{\rm ergs}^{-1}}\right)^{0.53}\left(\frac{\rm FWHM}{1000{\rm kms}^{-1}}\right)^{2} M_\odot \quad (1.16)$$

As the BLR is very close to the central AGN, NLR is a more extended region and can be directly estimated via spatially-resolved optical spectroscopy [22]. The general size of NLR is around hundreds to thousands of pc, sometimes even exceed the size of the host galaxy, such regions are referred to as *extended narrow-line regions* (ENLRs)

In summary, BLR is a region of gas clouds very close to the central AGN in a tiny region with high density and high velocity dispersion, while NLR is a region of gas clouds spreading over a more extended region with low density and low velocity dispersion.

### Dust Torus

Observations like [23] found obscuration at all wavelength except IR at the region between BLR and NLR, approximately 0.1 to 10 pc from the central BH. It turns out the main component in this region is a flat, thick structure in the shape of a torus made of dust and molecular gas. X-ray observations show that the column density of the dust torus is from $10^{22}$ cm$^{-2}$ to $10^{24}$ cm$^{-2}$. The size of the dust torus may also be measured by the RM method used in BLR. Since the radiation from the torus is mainly IR continuum, the time lag of V- (7.5 – 4 mm) and K-band (1.67 – 1.11 cm) magnitude response to the optical-UV continuum was used. The results correspond to a size of about $3R_{\rm BLR}(H\beta)$. Again, the size of dust torus is also found to be proportional to the bolometric luminosity in a power law of $L_{\rm bol}^{1/2}$, this is because dust grains cannot exist at temperature higher than $\sim 1000$ K, thus as the central source being brighter, the sublimation radius will be larger.

There are two main scenarios to explain the origin of the torus. First is originated from the gas inflow of the host galaxy, being part of the general flow that continues all the way to the central BH. Second is originated from the large-scale wind of the accretion disk, which may be formed by magnetic fields and radiation pressure.

### Jet

The AGN jet was a very early discovery in the history of this field, back to 1918 by Heber Curtis [24], in which their comments on M87 (NGC 4486) was:

> Exceedingly bright; the sharp nucleus shows well in $5^{\mathrm{m}}$ exposure. The brighter central portion is about $0'.5$ in diameter, and the total diameter about $2'$ nearly round. No spiral structure is discernible. A curious straight ray lies in a gap in the nebulosity in p.a. $20°$, apparently connected with the nucleus by a thin line of matter. The ray is brightest at its inner end, which is $11''$ from the nucleus.

We now know "the sharp nucleus" and "the brighter central portion" are the appearance of the central AGN, and the "curious straight ray" is the jet. The formation of the radio jet has three general categories. The first assumes it to be driven by the thermal pressure from two antiparallel channels that propagate adiabatically from the vicinity of the BH. The second assumes it to be produced by the strong AGN radiation along certain directions. The third is a hydromagnetic model that the magnetized accretion disk accelerates and collimates the jet by rotating, twisted magnetic fields, such flows are centrifugally driven and magnetically confined. the third scenario is a now better accepted one [25].

The energy reservior is thought to be the electromagnetic power of the spinning BH. In 1977, Roger Blandford and Roman Znajek introduced the now-called Blandford–Znajek process that when a rotating black hole is threaded by magnetic field lines supported by external currents flowing in an equatorial disc, an electric potential difference will be induced. If the field strength is large enough, the vacuum is unstable to a cascade production of electron-positron pairs and a surrounding force-free magnetosphere will be established. Under these circumstances energy and angular momentum will be extracted electromagnetically [26]. The extracted power is proportional to $B^2 M_{\mathrm{BH}}^2$, it can reach $10^{44}$ erg s$^{-1}$ for a SMBH of $10^8$ $M_\odot$ and magnetic field of $10^4$ gauss. This process may last for over 100 Myr, thus making the large-scale and bright jet in many radio-loud AGN.

### 1.1.2 AGN Unification: All in One

#### The AGN Family

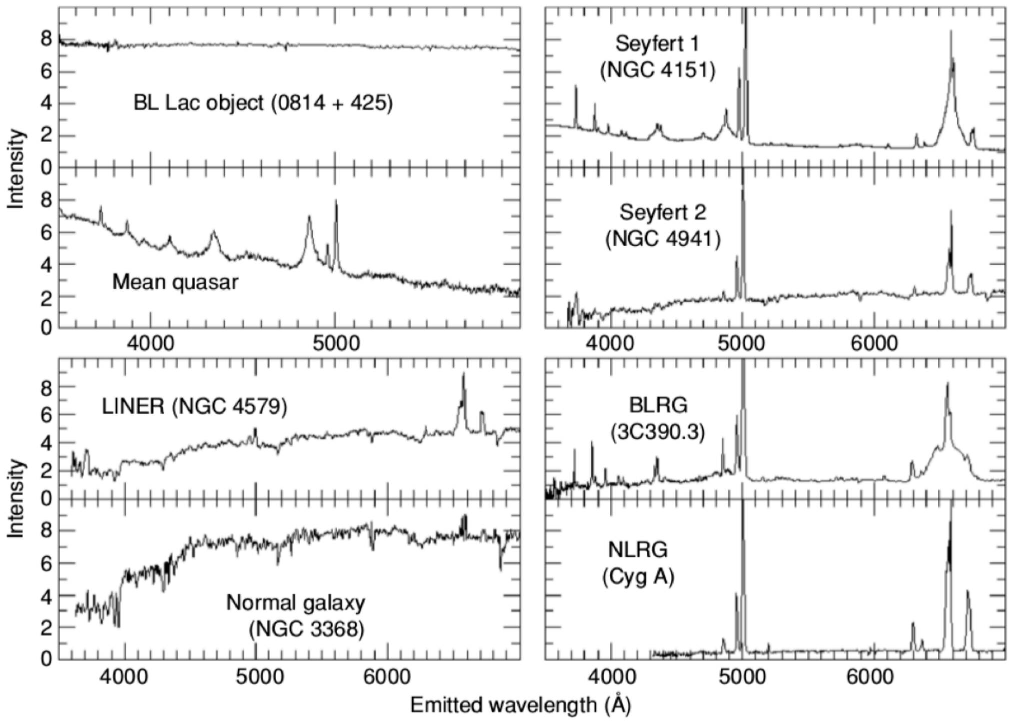


Fig. 1.2: Spectra of different type AGN, adopted from `http://pages.astronomy.ua.edu/keel/agn/spectra.html`

Based on different observational appearance, people classified AGN into subgroups, commonly referred types are summarized here:

- Seyfert Galaxies

  Usually hosted by spiral galaxies, their spectra reveal strong, high ionization emission lines.

  - Type 1

    Have both narrow emission lines with widths of several hundred km/s, and broad emission lines with widths up to $10^4$ km/s. e.g. NGC 1097.
  - Type 2

    Only have narrow emission lines. e.g. NGC 3147.

  - Intermediate Types

    Have broad lines weaker than type 1 but stronger than type 2, named as type 1.2, type 1.5, type 1.8 etc. e.g. Mrk 609.

- Radio Galaxies

  Usually hosted by elliptical galaxies, very luminous at radio wavelength, collimated jets observable. They may also be divided into type 1 (Broad Line Radio Galaxies, BLRGs) and type 2 (Narrow Line Radio Galaxies, NLRGs) following the same criterion as Seyfert galaxies. Here I include another classification depending on the radio structure.

  - Fanaroff and Riley Class I (FRI)

    Radio emission dominated by the center AGN, low luminosity. e.g. 3C31.

  - Fanaroff and Riley Class II (FRII)

    Radio emission dominated by jet, high luminosity. e.g. 3C98.

- Quasars

  The most luminous AGN, host galaxies unresolvable thus appear to be point-like sources.

  - Radio-loud quasars

    Radio loudness parameter $R \geq 10$, generally in the range 10-1000. e.g. 3C 273.

  - Radio-quiet quasars

    Radio loudness parameter $R < 10$, generally in the range 0.1-1. e.g. E1821+643.

  - Broad absorption-line (BAL) quasars

    Have broad absorption lines blueshifted relative to the quasar's rest frame, are usually radio quiet.

  - Optically violent variable (OVV) quasars

    High variable radio-loud quasars, also belong to blazars.

- BL Lac objects

  High variable AGN with weak emission lines, belong to blazars.

- Low-ionization nuclear emission-line region (LINERs)

  Correspond to the low luminous end of the AGN luminosity function. Could be hosted by either elliptical galaxies or spiral galaxies. LINERs are considered as an intermediate state between active galaxies and normal galaxies.

Figure 1.2 shows the spectra of different type of AGN with comparison to a normal galaxy at the bottom left panel.

### The AGN Standard Model

With All the components combined together, the standard model of AGN is finally built up (Figure 1.3) to explain all types of AGN in one single model. Figure 1.1.2 summarizes the different observational appearance of various kinds of AGN.

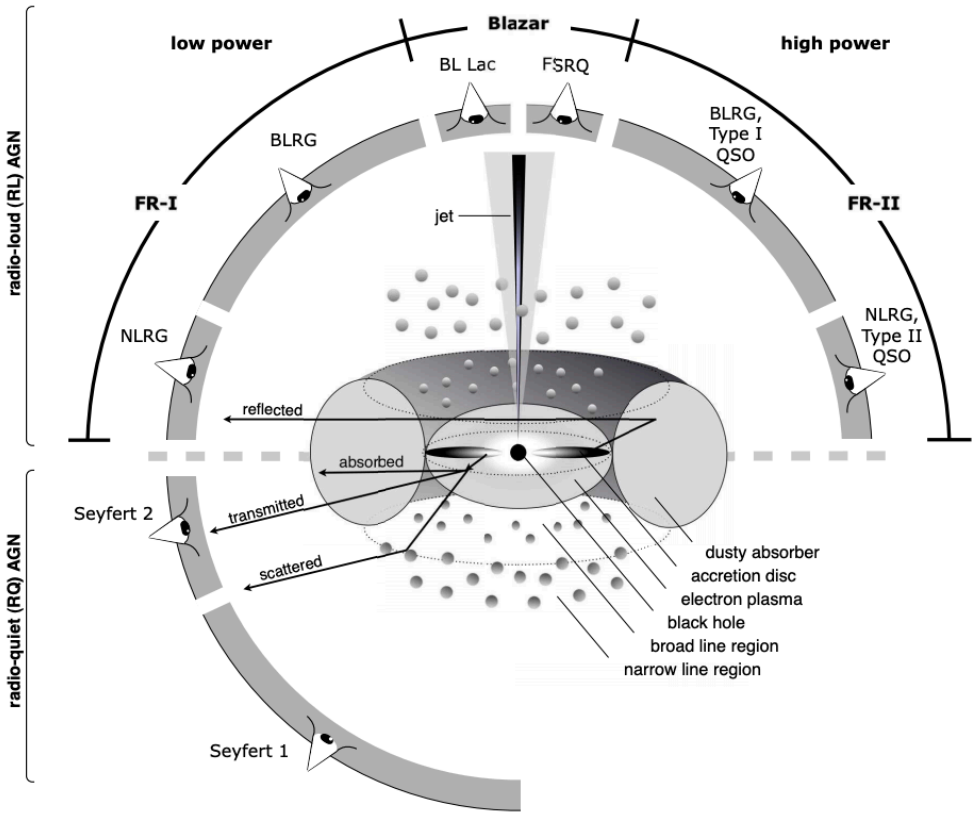


Fig. 1.3: The standard model and unified scheme of the AGN. The type of object we see depends on the viewing angle. Graphic courtesy of Marie-Luise Menzel (MPE). Adopted from [2]

| Galaxy type | Active nuclei | Emission lines | | X-rays | Excess of | | Strong radio | Jets | Variable | Radio loud |
|---|---|---|---|---|---|---|---|---|---|---|
| | | Narrow | Broad | | UV | Far-IR | | | | |
| Normal | no | weak | no | weak | no | no | no | no | no | no |
| LINER | unknown | weak | weak | weak | no | no | no | no | no | no |
| Seyfert I | yes | yes | yes | some | some | yes | few | no | yes | no |
| Seyfert II | yes | yes | no | some | some | yes | few | no | yes | no |
| Quasar | yes | yes | yes | some | yes | yes | some | some | yes | some |
| Blazar | yes | no | some | yes | yes | no | yes | yes | yes | yes |
| BL Lac | yes | no | no/faint | yes | yes | no | yes | yes | yes | yes |
| OVV | yes | no | stronger than BL Lac | yes | yes | no | yes | yes | yes | yes |
| Radio galaxy | yes | some | some | some | some | yes | yes | yes | yes | yes |

Fig. 1.4: Observational difference of various types of AGN. Adopted from wikipedia: Active galactic nucleus

In the center of AGN is a activated SMBH, accreting matters from its surrounding environment and forms a accretion disk with a radius around $10^{-3}$ pc, the particle velocities are thought to be relativistic, they lose their angular momentum via the dynamical friction with radiation released and then fall onto the central BH [17]. Ionized by the UV/optical emission from the accretion disk, the gases at the very vicinity of the BH (0.01 − 0.1 pc) form the BLR, the particle density in this region is around $10^{10}$ cm$^{-3}$ and the velocity dispersion is around few thousands km s$^{-1}$. Outside the BLR is thought to be the position where the dust torus locates. Rowan-Robinson (1977) found an excess in type-II AGN comparing to type-I AGN [27]. Also recall that type-II AGN only have narrow emission lines but no broad emission lines, this finally lead to the geometrically unification scheme of type-I and type-II AGN. As the dust is suggested to be a torus shape, it only covers the BLR at a limited angle, if we view from the direction that is perpendicular to the torus, we can see the BLR, while if we view from the side, it is blocked. The reason why we can see NLR in both types of AGN is that NLR is a more extended region that exceeds the torus, the particle number density there is around 10~$10^{6}$ cm$^{-3}$, enables some forbidden lines to be generated, the velocity dispersion is several hundreds km s$^{-1}$. The jet is thought to be collimated towards the polar directions of the disk, being the main source of the radio emission.

As we have unified the type-I and type-II AGN, next mission is the AGN with different image appearance. Basically, quasars are the most luminous kind of AGN whose radiation is dominated by the central point source and

LINERs are the faintest kind of AGN whose radiation is more dominated by the host galaxy and more similar to normal galaxies. Therefore, it is natural to think of a luminosity gradient among different types of AGN. Seyfets are just fainter version of quasars in which the light of the central AGN is not bright enough to blend the host galaxy, thus leave it resolvable. While the radio galaxies are hosted by ellipticals, they are assumed to be formed via violent merging events, during which the features like arms of the progenitors are floated. Blazars is a relatively rare class, their extremely strong variability is also explained by the geometric scheme. When our line of sight is directly towards the jet, due to the relativistic beaming effect, which is very sensitive to the velocity of the sources (see discussion in the previous section), its luminosity will change dramatically as the particle velocities in the jet varying.

This geometric unification scheme had reached a well agreement at 1990s (see the annual review of [28]) and now named as the "Standard Model" of AGN.

## 1.2 BH-host Coevolution

In 1982, Andrzej Sołtan argued that if quasars were powered by accretion onto a SMBH, then such SMBHs must exist in our local universe as "dead" quasars, thus the local BH density can be estimated via quasar luminosity, now known as the "Sołtan argument" [29]. The Hubble Space Telescope (HST) has made it possible to find BHs in many more galaxies and led to the convincing conclusion that BHs are present not only in AGN, but also essentially every galaxy that has a bulge component. This attracted the interest on studies of the correlation between the BHs and host galaxies.

### 1.2.1 Bulges

Bulge of a galaxy is a tightly packed group of stars within a larger formation. It was suggested that bulges and elliptical galaxies are formed in the same way that the major galaxy mergers scrambles disks into ellipsoids. In 1972, Toomre discussed in detail the role that a encounter plays in forming the structure of the galaxy under different conditions [3]. They modeled NGC 4676 (well-known as the Mice Galaxies) using a major merger scenario (same disk radius) as shown in Figure 1.5.

Followed by numerical simulations like [30], showing the same scenario also occurs for the ellipticals and observational studies like [31], the merger revolution in the understanding of elliptical galaxies has reached an agree-

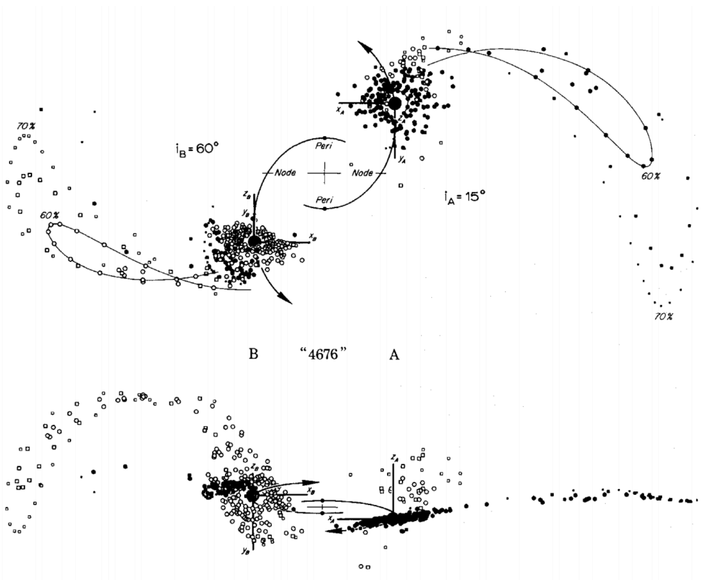


Fig. 1.5: Adopted from [3] Figure 22. Model of NGC 4676, during the encounter of two spiral galaxies, their disks are scrambled into bulge-like shape.

ment [32]. When ellipticals accrete cold gas and grow new disks around themselves, they become the "bulges" we know. For this kind of bulges, we refer to them as "classical bulges."

However, it turns out there exists another kind of "bulge" which has different properties from classical bulges, observationally, they appear to be diskier, thus named as "disky-bulges" or pseudobulges [33].

Figure 1.6 shows a comparison of these two kinds of bulges. Classic bulges are formed primarily by old stars, hence have a reddish hue. These stars are in random orbits, giving the bulge a distinct spherical form. Due to the lack of dust and gases, classical bulges tend to have almost no star formation (SF). While the stars in pseudobulges orbit in an ordered fashion, following the morphology of the spiral arms, star forming activities can be observed and tend to be blueish.

The brightness profile of both kind of bulges can be described using Sérsic function [34]

$$\ln I(R) = \ln I_0 - kR^{1/n} \tag{1.17}$$

where $I_0$ is the intensity at R=0. The parameter n is "Sérsic index," the smaller the value of n, the less centrally concentrated. Generally, n $>$ 4 for giant ellipticals, $\sim$ 2 to 3 for smaller ellipticals, $>$ 2 for classical bulges, and

Fig. 1.6: Comparison of the appearance of classical bulge and pseudobulge. Left: HST photos of M81, holding a classical bulge. Right: HST photos of ESO 498-G5, holding a pseudobulge.

$< 2$ for pseudobulges [35].

### 1.2.2 $M_{\rm BH} - L_{bulge}$, $M_{\rm BH} - M_{\rm bulge}$ and $M_{\rm BH} - \sigma_e$ correlations

At 1988, from a kinematic study on M31 and M32, Dressler and Richstone found that the ratio of the mass of the central object of these two galaxies (5 $\sim$ 10) are similar to the ratio of their spheroid luminosities ($\sim$ 15) [36]. One year later, at 1989, Dressler included 3 more galaxies: M87, N4594 and Milky Way, he suggested a rough scaling relationship between the black hole mass and the mass of the spheroidal component (the bulge) [37]. Kormendy and Richstone reviewed the early efforts to identify black holes in normal galaxies and the correlations, via assuming a mass-to-light ratio, the $M_{\rm BH} - L_{bulge}$ correlation can be converted to $M_{\rm BH} - M_{\rm bulge}$ correlation, the relationship suggested back to then was $\langle M_{\rm BH}/M_{\rm bulge} \rangle = 0.0022^{+0.0017}_{-0.0009}$, compared to the recent values of $\sim 0.0013$. This linear relationship has been supported by lots of studies such as [38, 39, 40, 41, 42].

At 2000, Gebhardt announced a new correlation between the BH mass and the the luminosity-weighted line-of-sight velocity dispersion $\sigma_e$ based on a sample of 26 galaxies [43]. Ferrarese & Merritt also reported a similar correlation at the same year based on a sample of 12 galaxies at the same year independently. This correlation is even tighter than the $M_{\rm BH} - L_{bulge}$ correlation and was believed to be the fundamental relationship between BHs and host galaxies. The study of this correlation was then expanded to bigger samples and to AGN, such as [38, 39, 41, 44, 45, 46, 47].

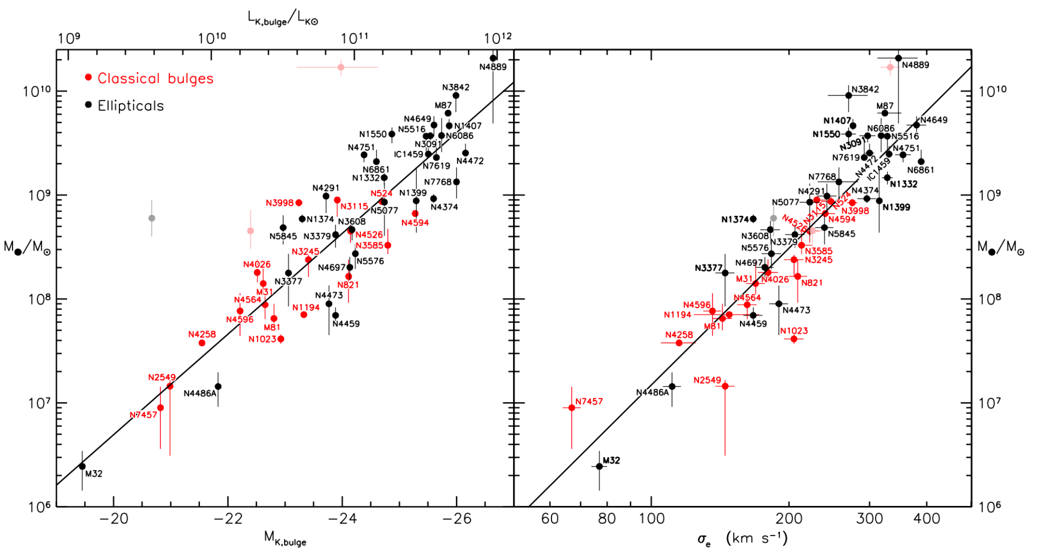


Fig. 1.7: Adopted from [4] Figure 16. Correlation of dynamically measured BH mass $M_{\rm BH}$ with (left) K-band absolute magnitude $M_{K,bulge}$ and luminosity $L_{K,bulge}$ and (right) velocity dispersion $\sigma_e$ for (red) classical bulges and (black) elliptical galaxies. The lines are symmetric least-squares fits to all the points except the outliers NGC 3842, and NGC 4889.

Figure 1.7 shows observational results of these two correlations updated by Kormendy & Ho at 2013 [4]. Fittings to these data gives:

$$\frac{M_\bullet}{10^9 M_\odot} = \left(0.542^{+0.069}_{-0.061}\right) \left(\frac{L_{K,\text{ bulge}}}{10^{11} L_{K\odot}}\right)^{1.21\pm0.09} \tag{1.18}$$

$$\frac{M_\bullet}{10^9 M_\odot} = \left(0.309^{+0.037}_{-0.033}\right) \left(\frac{\sigma}{200\text{kms}^{-1}}\right)^{4.38\pm0.29} \tag{1.19}$$

Recall in the previous subsection, we classified bulges into classical bulges and pseudobulges, as the above correlations are built on the ellipticals and classical bulges (because they are similar), it is natural to ask, do pseudobulges also follow such correlations [39]? Hu(2008) found that pseudobulges have smaller $M_\bullet$ at a given $\sigma$ than do classical bulges and ellipticals [48]. Indirect findings by graham showed similar difference between barred galaxies and unbarred galaxies [49]. They are actually related because barred galaxies preferably have pseudobulges. This deviation could be explained in two ways: $M_\bullet$ is anomalously small or $\sigma$ is anomalously large in pseudobulges. Later at 2011, Kormendy concluded that BHs do not correlate significantly with either the luminosities or the velocity dispersions of pseudobulges, the scatters are much larger than classical bulges and ellipticals [50]. They also showed that galaxy disks do not follow such correlations with BHs.

The different behaviors of pseudobulges and bulges became a clue to lead us to think about different scenarios for black holes to grow. One is via a global mechanism that connects the formation of bulges and BHs, another is a local way that does not lead into any correlations.

### 1.2.3 Galaxy Mergers

#### A Scenario

In reference to Figure 1.5, a galaxy merger is one possible answer for this kind of "global mechanism" that lead to the coevolution of BHs and bulges. Hernquist (1989) performed a N-body/hydrodynamic simulations based on a smoothed particle hydrodynamics (SPH) method to follow the behavior of gas in galaxy mergers. Besides the distortion of the disk, he also found that tidal effects caused by merger can lead to the deposition of gas at the centres of disk galaxies. A mass of gas $\approx 2 \times 10^9 M_\odot$ is driven into a central region $\sim$ 400 pc on a timescale $\leq 10^8$ yr. These gas will then become the material for SF [51]. Di Matteo (2005) followed this work and found that in addition to a burst of SF, the inflows of gas may also feed the SMBH and thereby power the quasar [52]. Therefore, mergers become a bridge that connect the normal galaxies with active galaxies. Hopkins (2008) showed a scheme of the lifetime of a typical galaxy that undergoes a gas-rich major merger (Figure 1.8).

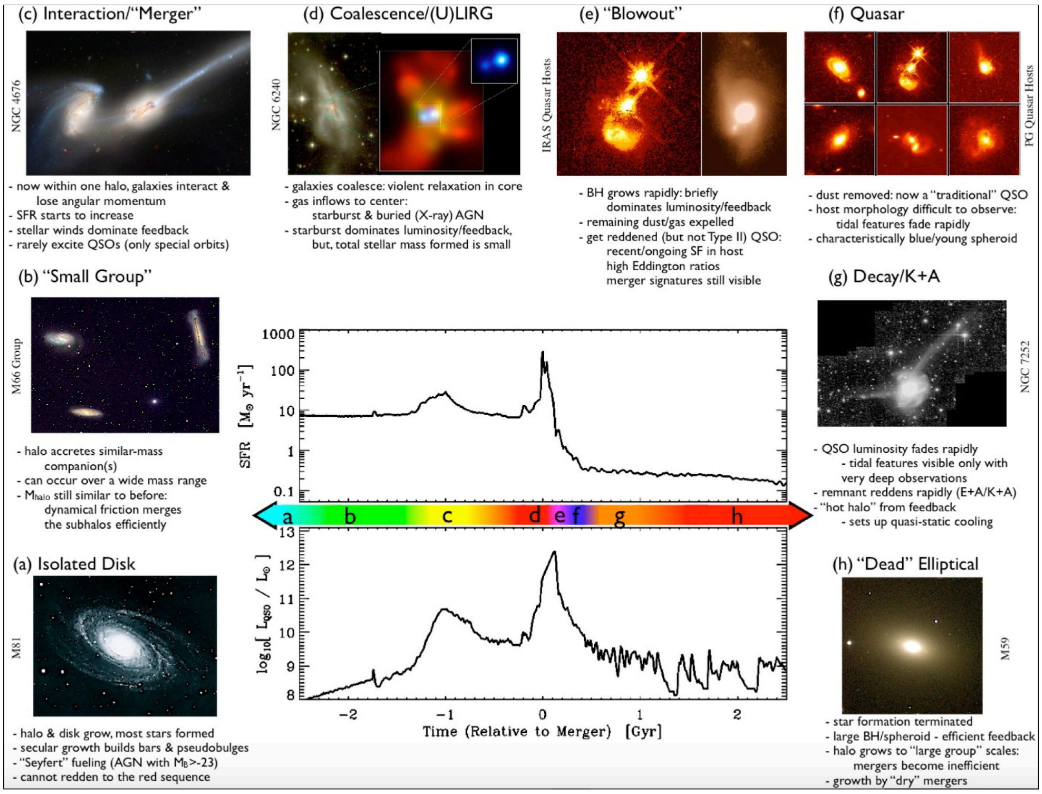


Fig. 1.8: Adopted from [5] Figure 1. Schematic outline of the phases of growth in a "typical" galaxy undergoing a gas-rich major merger. Image credit: (a) NOAO/AURA/NSF; (b) REU program/NOAO/AURA/NSF; (c) NASA/STScI/ACSScience Team; (d) optical (left): NASA/STScI/R. P. van derMarel &J. Gerssen; X-ray (right): NASA/CXC/MPE/S. Komossa et al.; (e) left: J. Bahcall /M. Disney/NASA; right: Gemini Observatory/NSF/University of Hawaii Institute for Astronomy; (f) J. Bahcall /M. Disney/ NASA; (g) F. Schweizer (CIW/DTM); (h) NOAO/AURA/NSF.

A isolated galactic disk is thought to grow in a secular way, bar and pseudobulge can be formed during this process. It may give birth to the low-luminosity AGN with $M_B \geq -23$, representatively, the Seyfert galaxies. Such isolated galaxies may form clusters under the gravity of a larger scale dark matter halo. In those dense groups, the merger events may happen. At the early stage of the merger (e.g. NGC 4676, Figure 1.5 is the simulation for the same object as the real HST photo of Figure 1.8 panel (c)), the distance of the main components of the two galaxies are typically tens of kpc, tidal torques distort the shape of the galaxies and the dynamical friction consumes the angular momentum of the gas and trigger on global inflows, SF at this stage is still weak, so is the AGN activity. During the final coalescence of the galaxies, gas falls into the central region, both activities become stronger, but on the other hand, the gas and dust also leads to obscuration of the optical light, making the galaxy a Luminous infrared galaxy (LIRG, $L \sim 10^{11}L_{\odot}$), the infrared emission comes from the secondary emission of the dust, just like what happens in AGN torus. More luminous cases are named as Ultra Luminous Infrared Galaxy (ULIRG, $L \sim 10^{12}L_{\odot}$ with infrared emission dominating the SED) and Hyper luminous Infrared Galaxies (HyLIRG, $L \sim 10^{13}L_{\odot}$). Observationally, many of these types of galaxies are captured in merger events, for example, Zwicky II 96, NGC 6240, Arp 220 and WISE J224607.57 − 052635.0, etc. As the gas is gradually consumed by star formation, and the feedback from the AGN expels the gas and dust away, turning the galaxy into a "blowout" phase with strong outflows. Some studies suggest that this is the origin of the $M_{\bullet} - \sigma_e$ correlation [53, 54, 55]. After the dust is removed, a traditional quasar becomes visible. Finally, as the quasar gradually runs out of fuel, it quenches to a dormant BH and the remnant is an elliptical galaxy.

### Wet or Dry

According to the gas richness of the galaxies, mergers can be divided into wet mergers and dry mergers. Gas rich wet mergers typically produce a large amount of star formation, and because of the dynamical friction of the gas, they usually transform disk galaxies into elliptical galaxies and trigger quasar activity. Gas poor dry mergers typically do not greatly enhance the SF and AGN activities, but can play an important role in increasing stellar mass. Furthermore, the remnants of these two types of mergers could be different. Some elliptical galaxies have cores, their brightness profiles show a break from steep outer Sérsic functions toward inner radii, appearing as cusps, while those do not possess cores have extra light at small radii. This extra light is interpreted to be generated by the stars that formed in the starburst stage of wet mergers [56, 35]. A recent study carried out by Lin (2018) based on the DEEP2 Redshift Survey found that at local universe ($z \sim 0.1$), 31% of mergers are wet mergers, 25% are dry mergers, and 44% are mixed mergers (one of the encounters is a gas rich galaxy, another is a gas poor galaxy)[57], while at $z \sim 1.1$, 68% of mergers are wet, only 8% are dry, and 24% are mixed. Wet mergers dominated earlier universe and the fraction of dry mergers increases over time, this is consistent to the stronger AGN activities from $z \sim 0.1$ back to $z \sim 1.1$, as more gas was feed to the BHs then.

#### Major or Minor

The importance of the initial mass ratio of the merging galaxies on the final fate of the BHs has been discussed in studies like [58, 59]. Numerous simulations have considered situations of equal-mass galaxy mergers [52, 60, 61, 62, 63], relatively fewer studies considered minor mergers [64, 65]. Pedro (2015) presented a detailed analysis on both major (they defined as mergers with mass ratio $< 4 : 1$) and minor (mass ratio $\geq 4 : 1$) mergers and compared the evolution of various properties like star formation rate (SFR), accretion rate and total mass of gas in the encounters. They found that in minor mergers, the secondary galaxy is significantly affected by the gravitational torques exerted by the primary, while the primary itself remains basically unperturbed during the whole interaction. while major mergers can significantly affect both galaxies, triggering major accretion episodes onto both BHs [6]. Some observations also supported that mergers contribute to the AGN activity systematically and the brightest AGN are formed via major mergers [66, 67, 68], while some stand against [69, 70]. Therefore, the contribution of mergers to AGN activities is still under debate.

## 1.3 Dual AGN

Recall mergers can trigger matter accretion onto BHs of the encounters, one possible product during this process is a dual AGN pair. The idea was put forward by Begelman et al. (1980), in which they discussed the physical processes in different stages of a galaxy merger and predicted the existence of such activated SMBH pairs [71]. This section will show some examples to give a brief introduction about both the theoretical and observational progresses that have been made on this topic.

### 1.3.1 Theory

#### Numerical Simulations

Numerical simulations usually focus on a small region at high resolution, allowing one to follow the detailed dynamics of the process. Here I consider the work of Pedro R. Capelo for an example. In Capelo (2015), they reported the result of a simulation of a coplanar merger (both galaxies are faced on

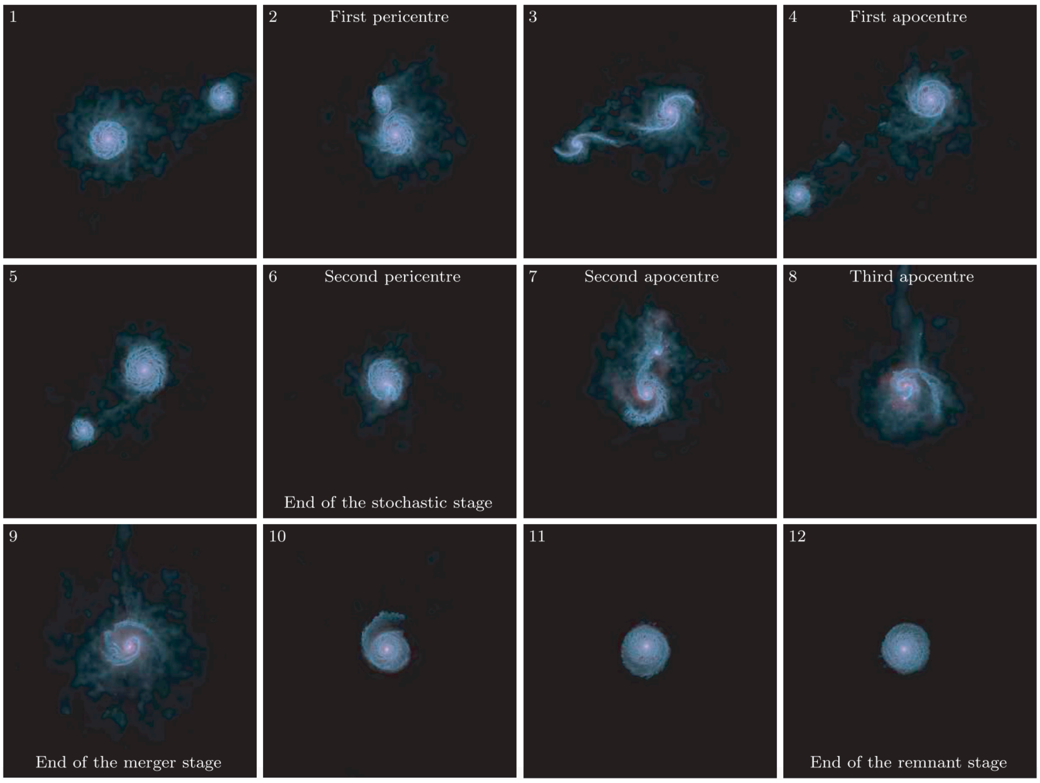


Fig. 1.9: Adopted from [6] Figure 3. Stellar (red) and gas (blue) density snapshots (viewed face-on) at representative times of the 1:4 coplanar, prograde–prograde merger: (1) 0.20, (2) 0.30 (first pericentric passage), (3) 0.39, (4) 0.61 (first apocentric passage), (5) 0.88, (6) 0.97 (second pericentric passage – end of the stochastic stage), (7) 1.05 (second apocentric passage), (8) 1.17 (third apocentric passage), (9) 1.24 (end of the merger stage), (10) 1.56, (11) 1.89, and (12) 2.21 Gyr (end of the remnant stage), respectively. The primary (secondary) galaxy starts the parabolic orbit on the left (right) of the first snapshot, moving right (left) wards. In order to make the gas more visible, gas density was overemphasized with respect to stellar density. Each image ’ s size is 70 $\times$ 70 kpc.

and move on the same orbital plane) with BH mass ratio 1:4 (Figure 1.9). Their mass and spatial resolution were $3.3 \times 10^3\,\mathrm{M}_\odot$ and 10 pc for stellar particles and $4.6 \times 10^3\,\mathrm{M}_\odot$ and 20 pc for gas. They divided the whole merger process into three distinct stages: the *stochastic* (or early) *stage*; the (proper) *merger stage*; and the *remnant* (or late) *stage*. The stochastic stage starts at a distance of ∼74 kpc of the two galaxies. In the second panel, after 0.3 Gyr, they undergo their first pericentric passage, tidal features are formed in the following panel. The dynamical friction of the gas in the galaxies work as a relaxation mechanism to slow down the encounters and the gravity drags them back to their second pericentric passage at a much shorter distance (∼1 kpc, compared to ∼10 kpc at the first passage). This happens 0.7 Gyr after the first passage. Therefore, the time scale for the decay of the orbits is around $10^8$ yr, consisting with the prediction of Begelman et al. (1980) [71]. This time, the morphology of the secondary galaxy is totally deformed and gases are expelled outwards (panel 7) and at the same time, falling onto the central BH and activate them as AGN [52], as we see the centers of both galaxies become brighter. The further hardening of the orbits will bound the two activated BHs and form a dual AGN pair (panel 8). Their simulation was not able to trace the dynamics of BHs on pc scales, thus the BH pair actually do not merge eventually in their run. But when they sink to the center, they take it as the end of the merge stage (panel 9). The final three panels show the remnant of such a violent event, which leaves a featureless galaxy there, with its center getting fainter and fainter.

Based on the simulation, they estimated the evolution of BH separation, compared the accretion rate and gas dynamics of the the primary and secondary galaxies. They found that the accretion rates of both BHs have a burst at the second pericentre stage (Figure 1.9 panel 6), lasting until the end of the merge (panel 9). At the same period of time, a significant loss of angular momentum is observed in especially the secondary galaxy. In their later work (Capelo and Dotti 2017 [72]), they explained the main physical responsible for this as the "ram-pressure". In 1972, James E. Gunn and J. Richard Gott suggested when a galaxy moves through a hot medium (e.g. gas), it would experience a pressure of $P_r \approx \rho_e v^2$, where $P_r$ is the ram-pressure, $\rho_e$ the gas density, and $v$ the speed of the galaxy relative to the medium [73]. Their original argument was a galaxy moving in intracluster medium, but the same thing also happens in galaxy mergers as we already see in Figure 1.9. The ram pressure dramatically alters the motion of the gas during the pericentric passage, decoupling the dynamics of the gas from that of the stars and results in the formation of a bridge between the two galaxies, which have been observed in some observations [74, 75]. Since both the tidal torques and ram-pressure efficiently trigger gas inflow, some level of dual-AGN activity associated with galaxy mergers is expected. Multiple investigations agreed on that dual AGN activity will be more efficiently promoted during the last stages of galaxy mergers [76, 77, 78].

### Cosmological Simulations

Numerical simulations of isolated galaxy mergers cannot provide any prediction on the fraction of AGN pairs out of the total number of AGN. Therefore, cosmological hydrodynamic simulations are developed to simulate more global behaviors of galaxies with lower resolution but larger area. For example, Steinborn et al. (2016) use a simulation with a large volume of 128 Mpc/h$^3$ and a spatial resolution of roughly 2 kpc from the set of Magneticum Pathfinder Simulations down to $z = 2$. They distinguished between four different classes of BH pairs:

- dual AGN
- offset AGN (both BHs are more massive than $10^7\ M_\odot$)
- unresolved offset AGN (while the AGN is more massive than $10^7\ M_\odot$, the second BH is below this resolution limit)
- dual BHs without AGN

Some examples of the appearance of these different classes are shown in Figure 1.10, together with the panoramic view of their simulation. Based on the definition of an AGN as a BH with its bolometric luminosity larger than $10^{43}$ erg s$^{-1}$, they have 1864 AGN in total, among which ∼0.5 per cent are dual AGN, ∼0.3 per cent are offset AGN, ∼0.4 per cent are unresolved offset AGN, 11 are dual BHs without AGN. Thus there are 35 BH pairs in total and the fraction of dual and offset AGN with respect to the total amount of AGN then sums up to ∼1.2 per cent [7].

Another interesting topic in cosmological simulations is estimating the redshift evolution of dual fraction. Figure 1.11 compares the results of the Magneticum simulation run by Steinborn et al. (2016) and EAGLE simulation run by Rosas-Guevara et al. (2019) [7, 9]. Basically, the predictions from the two simulations match very well, but they find that the fraction of BH pairs with one AGN is generally increasing in the EAGLE simulation (light blue and orange dots), whereas in the Magneticum simulation it is decreasing. Also, at $z \leq 3.5$, the dual fraction in Magneticum is significantly larger than EAGLE.

However, the Romulus simulation carried out by Tremmel et al. (2017) [79] found that multiple SMBHs within 10 kpc from the galaxy centre are very

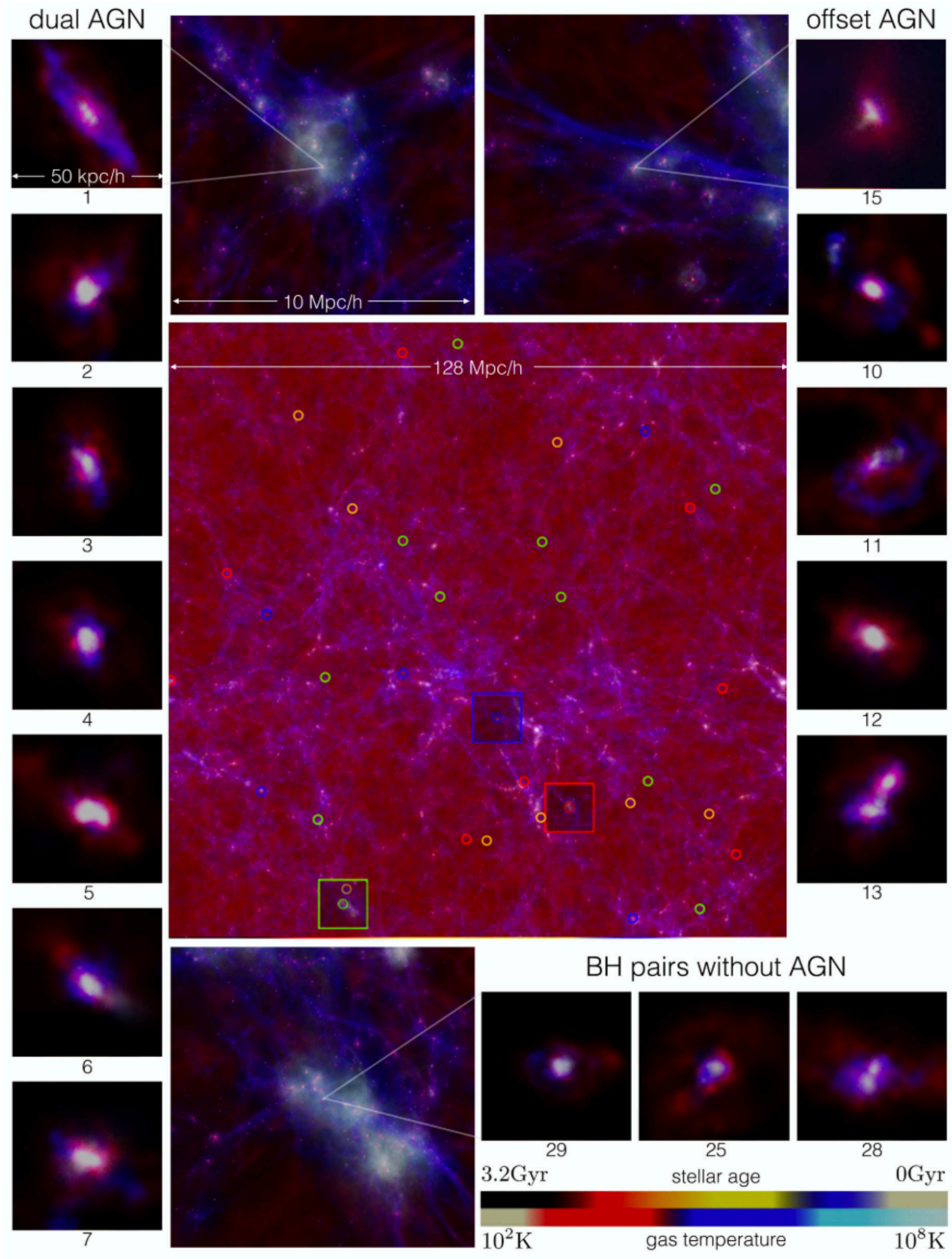


Fig. 1.10: Adopted from [7] Figure 4. The large panel in the middle shows a visualization of their cosmological simulation. The red, blue and green circles mark the positions of all dual AGN pairs, offset AGN and BH pairs without AGN, respectively. A box of 10 Mpc $h^{-1}$ length around the host galaxy is shown for one dual AGN pair, one offset AGN and one BH pair without AGN. The positions of these boxes are also marked in the large picture. Furthermore, they also showed a few examples of the host galaxies of the dual AGN (left-hand images), offset AGN (right-hand images) and BH pairs without AGN (images in the middle bottom). The colour bars are the same for all pictures, where the upper colour bar represents the age of the stars (from old to young in logarithmic scale of the cosmic age) and the lower one the gas temperature (from cold to hot in logarithmic scale).

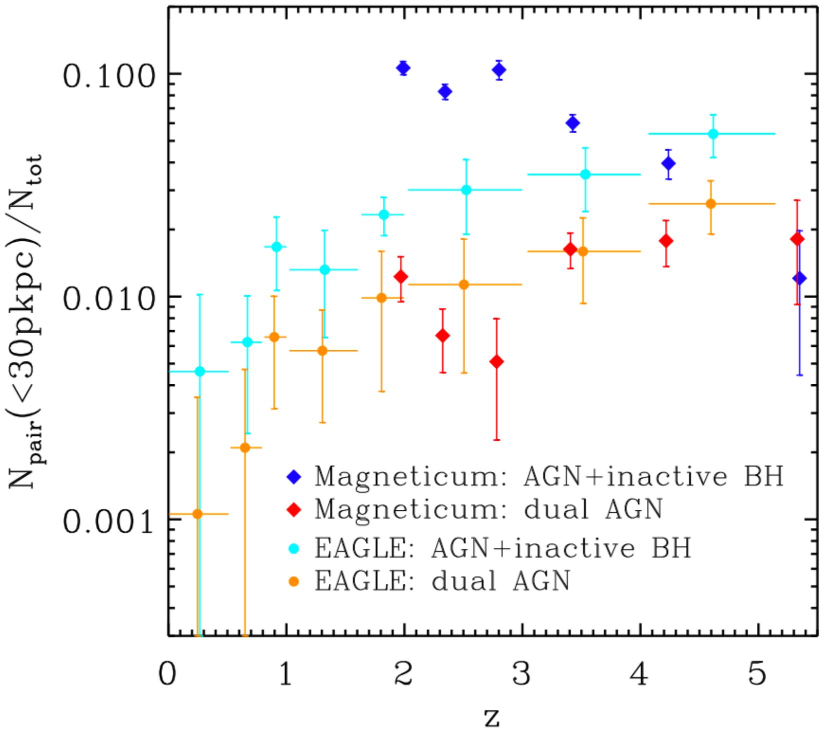


Fig. 1.11: Adopted from [8] Figure 5. Fraction of dual AGN (red/orange data-points) and BH pairs with only one AGN (light and dark blue data-points) with respect to the total number of AGN, for Magneticum (red and dark blue diamonds [7]) and for EAGLE (orange and light blue circles [9]). For both simulations only AGN pairs with a proper separation $< 30$ *kpc* are included.

common in low-mass haloes, different from only 35 BH pairs in Steinborn et al. (2016). But their work was performed at $z = 0$, there could be an increase in the number of BH pairs between $z = 2$ and $z = 0$. On the other hand, the Horizon- AGN simulation (Volonteri et al., 2016) [80] predicted a dual AGN fraction of 2 per cent with respect to all galaxies above $M_* > 10^{11}M_\odot$, a somewhat higher value than the Magneticum simulation. Therefore, the predictions of the amount of SMBH pairs and the fraction of dual AGN based on current cosmological simulations haven't reached an agreement, but some general points have been accepted [7, 80, 9]:

- The probability for dual AGN activity increases with decreasing distance between the BHs.
- The BH mass ratio of dual AGN is close to unity.
- Dual AGN do, on average, require a larger gas reservoir than single AGN.

## 1.3.2 Observation

**Serendipitous Discoveries**

The first discoveries of dual quasars may trace back to around 1980, including pairs with separation of Mpc scale such as QQ 0107-025 [81], QQ 1146+111[82], QQQ 0953+698 [83] and pairs with separation $\leq$100 kpc such as PKS 1145-071 [84], QQ 0151+048 [85], QQ 1343+266 [86]. These observations were all carried out in optical wavelength, the main evidence they argued to confirm the target is a dual quasar system is the existence of broad emission lines in both sources.

It is also feasible to search for dual quasars in X-ray wavelength. ULIRGs, as mentioned in previous section, could be one scene during the evolution of galaxies, right before the formation of a quasar (Figure 1.8 panel (d)). This consists to the time when dual AGN may form that numerical simulations predict (Figure 1.9). Therefore, some studies are interested in revealing the separated point sources in ULIRGs to find dual AGN. However, ULIRGs are usually optically obscured, one have to go to X-ray to *look into* the source. With the ACIS-S detector aboarding the Chandra X-Ray Observatory, Komossa et al. (2003) found there are two nuclei inside NGC 6240 (Figure 1.8 panel (d)), both of them have strong neutral Fe K$\alpha$ lines that originate from fluorescence in cold material illuminated by a hard continuum spectrum, indicating the AGN activities [87]. Later at 2008, Mrk 463 was also found to possess a binary AGN system using a similar method [88]. X-ray observations are also performed together with optical observations to give stronger evidence of dual AGN origins [89, 90]. *Chandra* has the currently best angular resolution, it can resolve into ∼20 pc at $z = 0$, but drops down to ∼8 kpc at $z = 1$. Therefore, without an improvement of instruments PSF (point-spread function), we can only probe kpc-scale separation dual AGN at low-redshift universe for now.

Detection with infrared and radio waveband is less commonly used but also viewed some success. For example, Imanishi and Saito (2014) found 4 dual AGN systems among 29 LIRGs via K- (2.2$\mu$m) and L'-band (3.8$\mu$m) high-spatial-resolution ($< 0''.2$) imaging observations using the Subaru 8.2 m telescope [91]. While Müller-Sánchez et al. (2015) found 3 dual AGN systems out of 18 AGN at 8.5 and 11.5 GHz via Very Large Array (VLA) observations. The limitation of IR and radio methods are the limitation of source types, as IR observation is sensitive only to dusty obscured AGN and radio observation only works for radio loud quasars.

### Systematic Studies

In 1991, when only 6 dual quasar systems were known, Djorgovski realized that these systems could be a probe of a hierarchical clustering model [92]. The two-point correlation function describes the probability that another galaxy will be found within a given distance to a random galaxy in a location, the higher the value for some distance scale, the more lumpy the universe is at that distance scale [93]. Earlier researches have drawn the result that the amplitude of the quasar-quasar two-point correlation function at $z \sim 1$ - 3 is about equal to that of the bright galaxies at $z \sim 0$ [94]. The expected probability of finding a quasar companion at a distance $R$ is given by

$$P(R) = 4\pi\langle\rho\rangle r_0^3 x^3 \left(1 + \frac{3}{3+\gamma} x^\gamma\right) \tag{1.20}$$

where $r_0 \sim 5h^{-1}$Mpc, $x \equiv R/r_0$, $\gamma \simeq -1.8$, $\langle\rho\rangle$ is the average comoving number density of quasars at that redshift, at $z \sim 1$ - 3, $\langle\rho\rangle \simeq 500\,\mathrm{Gpc}^{-3}$. They found the wide separated quasar pairs match the clustering model, but the close separated pairs (closer than 100 kpc) appear to be significantly overabundant above the model. This indicates that quasars are more likely to have a companion around them at close separation than a pure coincidencial distribution, thus indicates that at close separation, there could be some extra mechanism giving birth to new quasars. Related to the merger scenario, it then means galaxies under interaction would be more likely to exibit nuclear activity, this correspond to the results of numerical simulations. On the other hand, since gas was richer at earlier universe, the mechanism could be more effective at higher redshift, this relates to the cosmological simulations that work on the redshift evolution of dual fractions.

Djorgovski's prospect was exciting and instructive, but the observational data set then was too small and too limited. After 2000, with the rich products from the Sloan Digital Sky Survey (SDSS, [95]), it has been possible to search for dual AGN over a wider area systematically and enables us to study the clustering effect further. One outstanding work was done by Hennawi et al., (2006) [96], they discovered 221 quasar pairs over redshift range 0.5 $\sim$ 3.0 from SDSS and 2dF quasar Redshift Survey via color selection and spectroscopic data, and worked out the quasar correlation function from $\sim 400\,h^{-1}$ kpc down to $\sim 10\,h^{-1}$ kpc, followed by Hennawi et al., (2010) [97]. More recently, Eftekharzadeh et al., (2017) [98] reported a steeper power-law index of $\gamma = 1.97 \pm 0.03$ for the correlation function while fixing $r_0 = 5h^{-1}$ cMpc, compared to 1.6 $\sim$ 2.0 for galaxies in literature (e.g. [99], [100], [101] and [102]). This again supported Djorgovski's hypothesis in a way that quasars are denser at smaller separations than galaxies do.

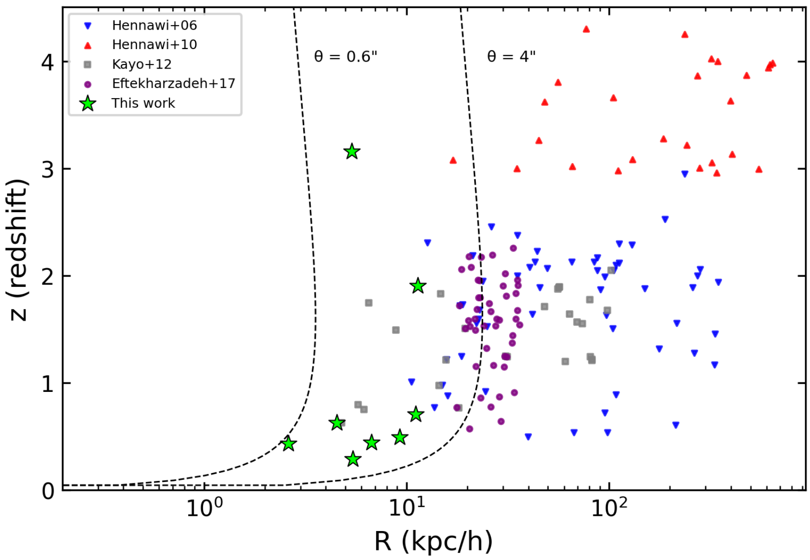


Fig. 1.12: Distribution of our dual quasars in the Redshift-Separation space, dashed lines label the selection range of our candidates. Green star marks are newly discovered quasar pairs in our study.

The fiber diameter of early SDSS-I, II spectroscopic observation was 3″, later SDSS-III, IV improved to 2″. Thus the separation of dual AGN found with SDSS data only is limited to this level. People have tried different ways to break this constraint. For example, Kayo and Oguri (2012) found 26 binary quasars from their lens research selected by the so-called morphology and colour algorithms [103]. Besides, Liu et al. (2010) [104] suggested that such systems may possess double-peaked [O III]$\lambda\lambda$4959,5007 lines, and can be confirmed with Chandra X-ray observation. They reported 4 kpc-scale AGN pairs out of 167 Type 2 AGNs with double-peaked features originally selected from SDSS DR7. Comerford et al. (2013) carried out a similar study by selecting AGN with double-peaked narrow emission lines from the AGN and Galaxy Evolution Survey (AGES) [105]. They confirmed one dual AGN from 12 optically-selected candidates at $z < 0.34$ with Chandra/ACIS and HST/WFC3 observation [106]. They also tried VLA (Very Large Array) in another study and confirmed 3 dual quasars out of 18 candidates with double-peaked [O III] emission. It turns out that most of such features are formed by outflow and possibly not efficient for the aim of discovering dual quasars.

In Figure 1.12 I show the distribution of newly discovered quasar pairs in this study compared to some of the systematical studies mentioned above in the redshift-separation space. This figure follows the fashion of Eftekharzadeh's Figure 4 [98]. Two dashed lines prescribe the region we focus on with this study, it was from $2''.9$ to $7''.7$ in Eftekharzadeh's work, taking the adavantage of HSC imaging data, we improved it to from $0''.6$ to $4''$ and successfully discovered 9 quasar pairs with 1 overlapping with Kayo's work and 1 picked out from SDSS data (without new observation).

## 1.4 Contents

This thesis includes five chapters.

- The first chapter reviews the history and constructions of the concepts involved in this study.
- The second chapter introduces the methodology, how the samples are selected, how the observation is carried out and how the data is reduced.
- Chapter shows the results of our observation, and the physical properties estimated based on the data.
- Chapter four discusses the statistical properties of our targets compared to other studies.
- Chapter five is a conclusion of the main findings in this thesis.

Throughout this paper, we adopt a standard $\Lambda CDM$ cosmology model with $H_0 = 70$ km s$^{-1}$ Mpc$^{-1}$, $\Omega_m = 0.30$, and $\Omega_\Lambda = 0.70$. so that an angular separation of $1''$ at redshift 1.5 corresponds to a projected distance 5.92 kpc $h^{-1}$.

# Chapter 2

# Methodology

In this chapter, we describe the methods we use to search for dual quasars. The sections include descriptions of the sample selection, spectroscopic follow-up, and the the procedure to convert raw spectroscopic CCD images to science-quality data.

## 2.1 Sample Selection

### 2.1.1 Data Set

In this study, two parent data sets are included: Sloan Digital Sky Survey (SDSS) DR14 Quasar catalog and the second public data release (PDR2) of Subaru Hyper Suprime-Cam (HSC)/Subaru Strategic Program (SSP). As we are looking for dual quasars, the SDSS DR 14Q catalog ensures at least one quasar per potential dual system. On the other hand, HSC does not have an independent quasar catalog, PDR2 is a mixture of all types of targets including stars, galaxies and quasars. Therefore, we match the SDSS catalog with HSC catalog to make use of the high resolution images of quasars.

#### SDSS DR14Q

The Sloan Digital Sky Survey (SDSS) uses a 2.5-m wide-angle optical telescope at Apache Point Observatory (APO) in New Mexico, United States. Since its start of operations in 2000, its spectral database has grown to 4 million objects covering over 35% of the sky. Data Release 14 (DR14) is the second data release of the fourth phase of the Sloan Digital Sky Survey (SDSS-IV). It provides a quasar catalog from the extended Baryon Oscillation Spectroscopic Survey (eBOSS), that also includes previously spectroscopically-confirmed quasars from SDSS-I, II [107] and III [108, 109, 110]. The SDSS quasar selection includes magnitude- and color-selected samples and objects identified through radio, infrared and X-ray surveys including FIRST, GALEX, 2MASS and ROSAT. In total it contains 526,356 quasars up to $z \sim 5$. The spectral data are taken with fibers, each subtending 3″ (SDSS-I/II) or 2″ (BOSS/eBOSS) diameter on the sky, connected to the plates. Each plate has a field of view of approximately 7 deg$^2$ and contains 1000 fibers, their spatial locations are shown in figure 2.1. The spectroscopic data cover the wavelength from 3600 to 10,000 Å with resolution varying from $\sim$ 1300 at 3600 Å to $\sim$ 2500 at 10,000 Å [10].

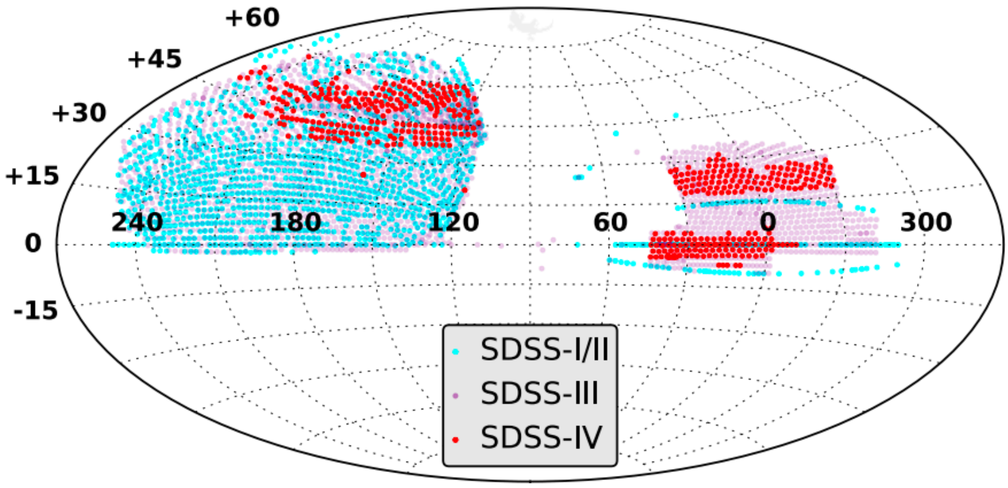


Fig. 2.1: SDSS footprint on the sky, adopted from figure 1 of [10] , distribution on the sky of the SDSS-DR14 spectroscopy in J2000 equatorial coordinates. Cyan dots correspond to the 1462 plates observed as part of SDSS-I/II. The purple dots indicates the 2587 plates observed as part of SDSS- III/BOSS. The red dots represents to the 496 new plates as part of SDSS-IV.

### Subaru HSC/SSP PDR2

The Subaru Telescope is a 8.2-meter Ritchey-Chretien reflecting telescope built on the Mauna Kea Observatory on Hawaii. HSC is a wide-field (1.7 degree diameter) optical imager installed at the prime focus of the Subaru Telescope. SSP is a survey using this instrument started from March 2014 [111]. It includes 3 layers: Wide, Deep, and UltraDeep. The Wide layer covers 1400 deg$^2$ in 5 broad-band filters (grizy) down to about 26th magnitude. The Deep layer has 4 separate fields (XMM-LSS, COSMOS, ELAIS-N1, DEEP2-F3) covering in total about 26 deg$^2$. The UltraDeep layer has 2 fields: COSMOS and the Subaru/XMM-Newton Deep Survey (SXDS) it covers 4 deg$^2$ down to 28th magnitude. PDR2 of HSC/SSP includes data from 174 nights of observing time with 4 billion targets in total [11]. The imaging used in this study included 796 deg$^2$ of i-band imaging. We include all imaging with at least one 200 second exposure, so not all data reach the final depth of 26.2 mag (5$\sigma$; AB). Our initial selection of dual quasar candidates is based on the i-band because the seeing condition of i band is $0.58 \pm 0.05$ arcsecond, the best among all five bands.

### 2.1.2 Image Analysis

As we match the catalog, it turns out 34,476 SDSS quasars are within the usable HSC exposure area which are not flagged as saturated ($i_{AB} \geq 18$), having a bad pixel, or unable to determine a magnitude based on a model fit. We input the HSC image cutouts, the variance image and model PSF to the open-source package Lenstronomy [112] in Python to detect those with multiple optical components. For each candidate, different models are tried, e.g. one point source only, two point sources, two point sources with one Sérsic profile, two point sources with two Sérsic profile, and etc. Each model is fitted with the center position of the point source, total flux, Sérsic parameters (if there is at least one Sérsic profile), whose half-light radius is limited within [0".1, 1".0], Sérsic index limited within [0.3, 7] to ensure a physical output and 2D ellipticity of the image. The combination of the parameters are optimized by the Particle Swarm Optimization method [113]. All galaxies in the field-of-view of the image are simultaneously fitted as their extended profiles can contribute to the flux of the main sources. The performance of each model is estimated by the $\chi^2$ value, and the best four models are output together with their best fit parameters. We show an example of the best fit results of one of our candidate SDSSJ220906.91+004543.9 in Figure 2.3.

Using our decomposition algorithm, we pick out the targets with multiple optical components with a separation between 0."6 $\sim$ 4" as our dual quasar candidates. The lower limit is determined by the spatial resolution of HSC while the upper bound is arbitrarily set to minimize the level of contamination and overlap with privious studies. We initially identified 452 candidates within these separations. Then rejected 27 objects as artifacts via visual inspection and four objects that are found to be gravitational lenses according to the literature. Among the left 421 candidates, 401 of them have all 5-band photometry information. For this smaller sample set, we run our decomposition codes for the other 4 bands (i.e. g,r,z,y), thus get the model-

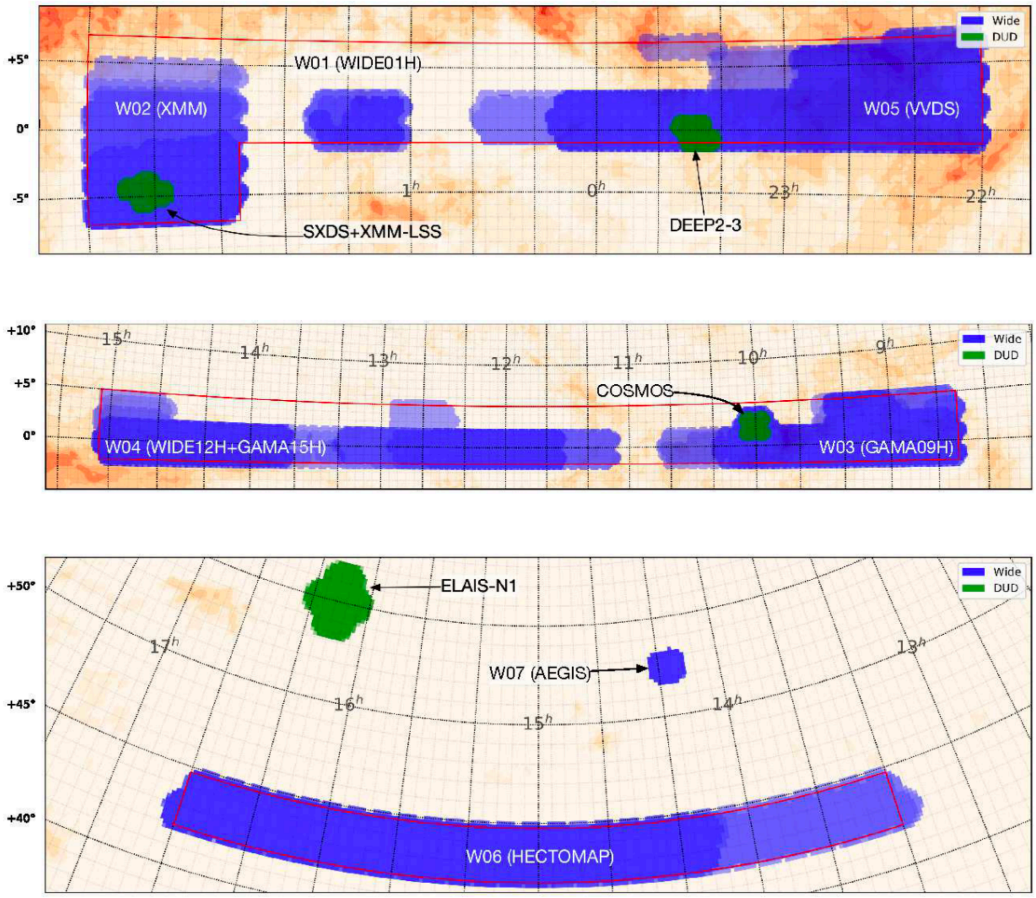


Fig. 2.2: Adopted from [11] figure 1. The area covered in HSC PDR2 catalog. The blue and green areas show the Wide and Deep+UltraDeep layers, respectively. For the Wide layer, the darker color means that the area is observed in more filters (up to 5 filters). The red boxes indicate the approximate boundaries of the three disjoint regions that will make up the final Wide survey.

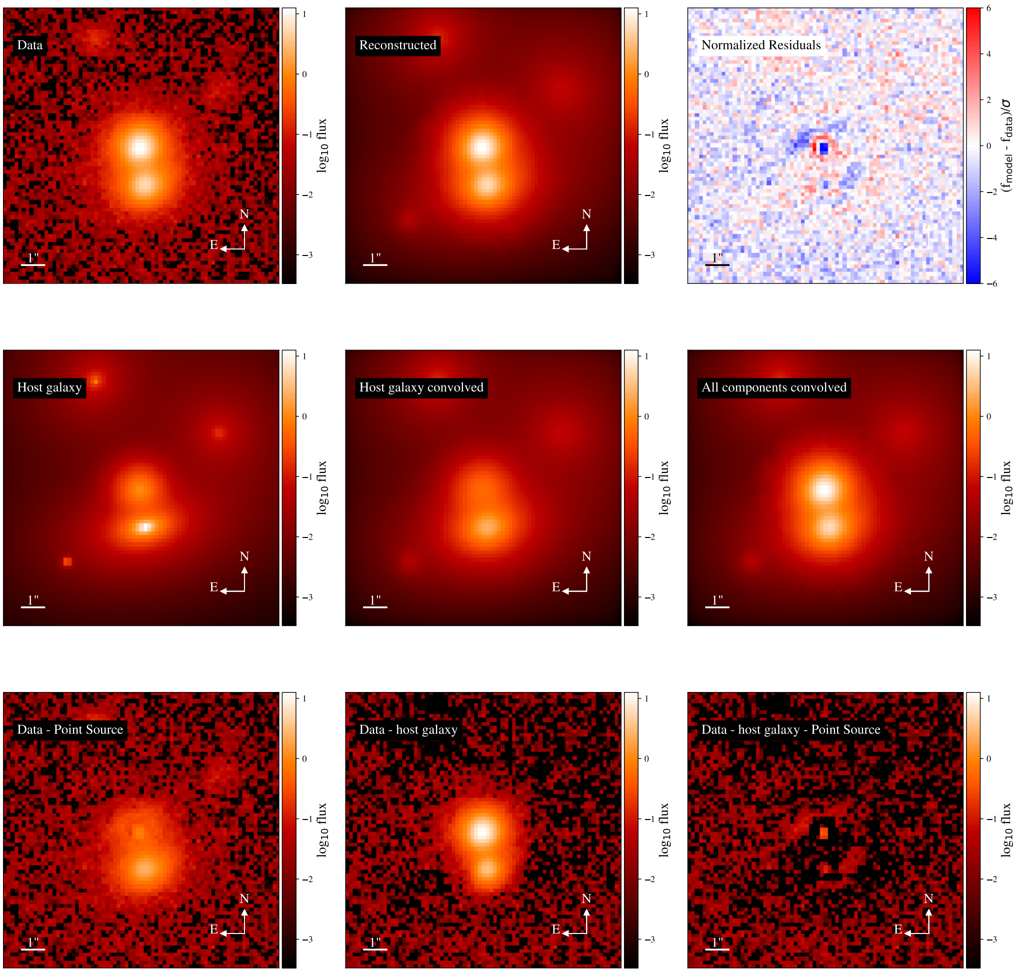


Fig. 2.3: An example of the algorithm, which is carried out on the HSC-G band image of SDSSJ220906.91+004543.9. The upper left panel is the original HSC data, upper center panel is the final result of fitting, upper right panel is the subtraction of the previous two, showing the normalized residual distribution in the field. Middle left panel is the modeled host galaxy, middle center panel convolves a gaussian kernel to that to smooth the model. Middle right added the point sources to the model, thus is the final fitting result (same as upper center panel). Lower left panel subtracts the modelling point sources from the original data, lower center panel subtracts the modelling host galaxy from the original data, lower right panel subtracts both, leaving the residuals (the same as upper right panel but before normalization).

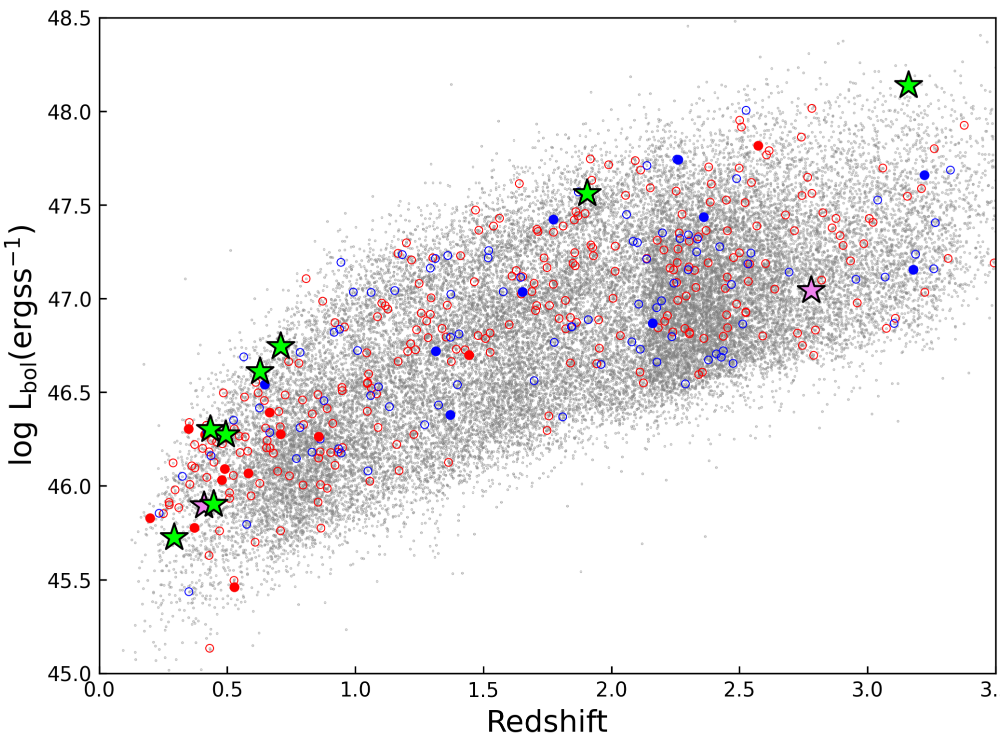


Fig. 2.4: Distribution of our targets in $L_{bol}$-Redshift space. Grey dots are 34476 SDSS DR14 quasars which are imaged by HSC. Colored circles are 401 targets after selection as dual quasar candidates, blue open circles are targets with their companion sources have g - r > 1.0 and red open circles with g - r ≤ 1.0. The filled ones are what we have acquired further spectroscopy but turned out to be negative detections (i.e. not a quasar pair). Green star marks are successfully confirmed dual quasars, pink stars are projected quasar pairs with two sources at different redshift.

ing magnitudes in all 5 bands of the candidates (both the point sources and the hosts), which are subsequently used for color selection, flux calibration, and stellar mass estimation. We set an empirical criterion at $g - r = 1$ to separate the priorities of the candidates into two groups. There are 116 dual candidates bluer than this value, we put them as high priority candidates. However, this color cut is not definitive; massive stars can be this blue, and obscured quasars can be redder thus we still include red sources in our spectroscopic follow-ups taking the risk of a lower success rate. In Figure 2.4 we show the bolometric luminosities of this sample set relative to the overall parent quasar population as a function of redshift. Table 2.1 summarizes the sample size at each step in the selection process.

Table 2.1: Sample selection

| Category | Number |
|---|---|
| SDSS DR14 quasar catalog | 526357 |
| Imaged by the HSC wide-area survey | 34476 |
| Dual quasar candidates with 0.6–4 ” separation | 452 |
| after visual inspection | 425 |
| minus known lenses | 421 |
| with 5-band photometry available | 401 |
| with the companion having $g - r < 1.0$ | 116 |

*Note:* The sample size at each step in the selection process.

## 2.2 Spectroscopic Observing Program

For next step, we have to confirm the origin of the companion point source, which could be a gravitationally lensed quasar, or a projected star, galaxy, or another quasar. Therefore, we need spectroscopy with good enough seeing conditions to separate the two components and confirm their origins. Considering the economic issue, at this time point, we prefer to use the ground-based telescopes than the space telescopes. As these candidates are selected optically, we start from optical observations to look for the broad emission lines such as C IV$\lambda$1549, MgII$\lambda$2798, H$\beta$ and $H\alpha$ as a commonly accepted evidence for an AGN. The search for these lines determine which instruments we are going to use for our observations, essentially dependent on the wavelength coverage and spectral resolution of targets at different redshifts. For the obscured AGNs, the H$\beta$ and H$\alpha$ regions can still provide us information to identify the AGN origin based on diagnostic diagrams. Once they are confirmed or turn out to be ambiguous due to lack of evidence in the optical waveband, we then will turn to space telescopes such as HST

(Hubble Space Telescope) for a higher quality data and Chandra for a view of X-ray or ground-based IR or radio telescopes as supportive information and evidences.

Considering the spatial distribution of our candidates, some of them are equatorial and others are located at $40° - 55°$ as shown by the HSC footprint (figure 2.2). Therefore, we expect our telescopes to cover both regions with small angles so that we can have a longer time window to observe and suffer less from the air mass. As they are originally selected by the Subaru telescope, itself is naturally a good choice to reach that depth of the candidates. Smaller telescopes will spend more time on each target, but we hope to check as many targets as possible in a limited amount of available time. With Subaru telescope, we expect to spend 30 minutes on each target and thus observe 20 targets per night. The Subaru telescope is located at the Mauna Kea Observatory, which is famous for its ideal observation conditions with dark skies from lack of light pollution, good astronomical seeing, low humidity, high elevation above most of the water vapor in the atmosphere, clean air and good weather. There are two other telescopes having comparable abilities to the Subaru telescope at the same observatory: the Keck telescope and the Gemini North telescope. Therefore, we decided to submit our proposals to these three telescopes.

The telescopes can either be used in visitor mode or queue mode. For the visitor mode, the observers are assigned with solid dates for concentrated observation and have to operate the telescopes by themselves. The Subaru telescope can be remotely operated from the National Astronomical Observatory of Japan (NAOJ) in Tokyo. This saves our time of travelling. But the other two telescopes require one to visit the big island of Hawaii. On the other hand, the observers have to face the risk of a bad weather when the observation could be canceled out. The queue mode works in another way such that we can just put our candidates in the list (if accepted) and wait for the local observers to send us data. This ensures the quality of the data and again, saves the time of travelling. But the data is taken more sparsely, one may have to wait for more than half a year to get all the requirements done. Also, we have less freedom on making changes to the observational plans. We required both modes in our observation, for those with very close separation and high priority, we proceed with the queue mode to make sure they are observed under good condition. For those with relatively large separation (mostly), we proceed with the visitor mode to check as many of them as possible.

Commonly used spectroscopic observations include that with a long-slit spectrograph, multi-slit spectrograph or integral field spectrograph (IFS). IFS provides a 3D data cube with 2 dimensions of space and 1 dimension of wavelength, while the slit strategies provide 2D data with 1 dimension of space and 1 dimension of wavelength, i.e. stacks of the data for one space dimension. As we already have 5 bands photometry information of our targets, and IFS will spend roughly double the time of slit-based spectrograph, we prefer to use slits to capture the spectrum here. Most of our targets only have two sources, which are enough to be covered by a single long slit. Only a few of our targets have three sources, in those cases, we set the alignment of the slit to cover the two unknown sources as the main quasar has already been confirmed by SDSS. We set the upper limit of the width of the slit we use to be $1''$ to minimize the contamination from sky emission, nearby objects, and the host galaxy of AGN itself. Also, a narrower slit width will give a better spectral resolution.

### 2.2.1 Keck/LRIS

The W. M. Keck Observatory is a two-telescope astronomical observatory at the summit of Mauna Kea in the U.S. state of Hawaii. Both telescopes have 10 m (33 ft) aperture primary mirrors. The Low Resolution Imaging Spectrometer (LRIS) is an optical imaging and spectroscopy instrument equipped on Keck-I telescope, it is a double instrument dividing the light into blue and red components using a dichroic mirror, which enables it to cover the whole spectral region from 3100 to 11000Å in a single exposure [114]. This is ideal to include most of the features we need to confirm a quasar mentioned above.

Our observations were carried out at 2019 January and February as filler targets for another program leaded by K.G. Lee. Three nights in total were included (Jan 10th, Jan 11th and Feb 4th), our targets are mainly observed at the first night, the seeing varied from $2''$ to $0''.6$. The light was dispersed to the red camera via the 600/7500 grating with 0.8 Å/pixel dispersion and the 600/4000 grism with 0.63 Å/pixel dispersion to the blue camera, no filter was applied, the width of the slit is $1''.0$.

### 2.2.2 Subaru/FOCAS

The Faint Object Camera and Spectrograph (FOCAS) is a Cassegrain optical instrument for the Subaru Telescope. Its capabilities include 6' ϕ FOV direct imaging, low-resolution spectroscopy (R = 250$\sim$2000) and multi-slit spectroscopy and polarimetry [115]. We observed 21 candidates in 18.09.2019 and 19.09.2019 using FOCAS (S19B-079, PI: J. D. Silverman). The first night observation was executed with the VPH850+O58 grism, which covers the wavelength range from 5800 Å to 10350 Å with 1.17 Å/pixel dispersion, aiming at sources at redshifts 0.23-0.82 and 1.86-2.2. The second night configuration used the 300B+Y47 grating, covering wavelength from 4700 to 9100 Å with a 1.34 Å/pixel dispersion, aimed at targets at redshifts 0.82-1.86 and larger than 2.2. We elected to use a slit width of $0''.8$. The seeing condition was around $0''.4$ for the first night, and it varied between $0''.4$ and $1''.2$ for the second night. As most of our samples have magnitudes brighter than 21st magnitude (AB), we basically required two 10 minutes exposure for each object (table 2.2 column 10) so that the S/N will be greater than 10. For targets brighter than 19th magnitude, we reduce the exposure to two 5 minutes to save time. We did a quick reduction on the data every time after we take one exposure. Sometimes we decided to skip the second exposure if we think that target is not promising. Exposures with a ThAr arc lamp were taken to calibrate the wavelength and the standard star G191B2B was taken for flux calibration during the observation.

### 2.2.3 Gemini/GMOS-N

The Gemini Observatory consists two 8.1-metre (26.6 ft) telescopes. The Gemini Multi-Object Spectrographs (GMOS) instrument provides 0.36-0.94 $\mu$m long-slit and multi-slit spectroscopy and imaging over a 5.5 square arcminute field of view [116]. We observed 9 candidates using the Gemini Multi-Object long-slit Spectrograph in queue mode (GN-2019B-Q-128, PI: J. D. Silverman) from September 2019 to December 2019. We require a seeing condition of $0''.4 - 0''.75$, 20% image quality, 50% cloud, and 80% sky background. The exposure time varied based on the luminosity of the target, ensuring S/N to be at least 5 for the detection of broad emission lines. We used R400, R831 and B600 gratings aiming at targets with different redshifts for the coverage of emission lines. CuAr lamp was taken to calibrate the wavelength and standard stars EG131 and Feige 66 are taken for flux calibration.

### 2.2.4 Observation Setups

The setups of observation with the above three telescopes are listed in Table 2.2. The targets are ordered by the time they were observed (column 9). In total, there are 36 rows of information, but actually only 33 distinct candidates are observed because we revisited three candidates for better S/N or wider coverage of wavelength (No.8 & No.32, No.17 & No.31, No.23 & No.28). The RA, DEC and redshift of the candidates are taken from SDSS, while the separations are calculated from our decomposition based on HSC imaging, indicating the angular separation of the point sources. Column 6 and 7 records the instruments, grisms and filters we used for observation. K/L is short for Keck/LRIS, S/F is for Subaru/FOCAS, G/G is for Gemini/GMOS-N. For LRIS, data are taken with two cameras simultaneously, so there are two settings in column 7, left of the semicolon is for the red camera, right is for the blue. 6/75 is short for 600/7500 grating, and 6/40 is short for 600/4000 grism. The position angle is decided by the position of separated two sources in each candidate (output of our algorithm, not shown here), pointing from north to east. They are feed to the operation file of the telescope so that the alignment of the long slit will cover both of our sources. Column 10 records the time of exposure for each source in the format of ”single exposure time × times”. Again, two numbers are recorded by the Keck telescope referring to the red and blue arm.

Table 2.2: Basic information and observation setups

| | Name (J2000) (1) | RA (degree) (2) | DEC (degree) (3) | Redshift ($z_s$) (4) | Sep (”) (5) | Inst (6) | Grism+Filter (7) | PA (°) (8) | Date (dd.mm.yy) (9) | Exp (s) (10) |
|---|---|---|---|---|---|---|---|---|---|---|
| 1 | J0119-0020 | 19.897051 | -0.342664 | 0.8576 | 0.77 | K/L | 6/75; 6/40 | -9.7 | 10.01.19 | 900; 880 |
| 2 | J0848+0115 | 132.233688 | 1.261119 | 0.6457 | 1.21 | K/L | 6/75; 6/40 | -60.4 | 10.01.19 | 900; 880 |
| 3 | J0847-0013 | 131.793365 | -0.217406 | 0.6269 | 0.95 | K/L | 6/75; 6/40 | -34.96 | 10.01.19 | 900; 880 |
| 4 | J0903+0020 | 135.947235 | 0.340634 | 0.4124 | 2.22 | K/L | 6/75; 6/40 | 63.8 | 10.01.19 | 900; 880 |
| 5 | J1416+0033 | 214.156021 | 0.564521 | 0.4336 | 0.66 | K/L | 6/75; 6/40 | -69.53 | 10.01.19 | 600; 580 |
| 6 | J1214+0102 | 183.521362 | 1.034775 | 0.4927 | 2.18 | K/L | 6/75; 6/40 | -8.3 | 10.01.19 | 600; 590 |
| 7 | J0949+0005 | 147.430588 | 0.093404 | 0.4220 | 1.24 | K/L | 6/75; 6/40 | 53.65 | 04.02.19 | 900; 880 |
| 8 | J2202+0049 | 330.619415 | 0.817198 | 1.4482 | 1.22 | S/F | VPH850+O58 | 65.64 | 18.09.19 | 180 × 3 |
| 9 | J2207-0017 | 331.826813 | -0.289751 | 0.7086 | 1.85 | S/F | VPH850+O58 | 5.29 | 18.09.19 | 300 × 3 |
| 10 | J2209+0045 | 332.278809 | 0.762209 | 0.4461 | 1.67 | S/F | VPH850+O58 | 8.5 | 18.09.19 | 300 × 3 |
| 11 | J2211-0000 | 332.812775 | -0.008605 | 0.4778 | 1.90 | S/F | VPH850+O58 | 40.05 | 18.09.19 | 300 × 1 |
| 12 | J2251+0016 | 342.94928 | 0.27794 | 0.4097 | 1.86 | S/F | VPH850+O58 | -31.59 | 18.09.19 | 600 × 2 |
| 13 | J2311-0013 | 347.970428 | -0.226392 | 0.3478 | 1.75 | S/F | VPH850+O58 | -18.18 | 18.09.19 | 600 × 2 |
| 14 | J2328+0112 | 352.222507 | 1.206083 | 0.5280 | 0.66 | S/F | VPH850+O58 | 68.61 | 18.09.19 | 600 × 2 |
| 15 | J0004-0001 | 1.166559 | -0.029582 | 0.5829 | 1.23 | S/F | VPH850+O58 | -20.5 | 18.09.19 | 600 × 2 |
| 16 | J0219-0556 | 34.87715 | -5.945302 | 0.2920 | 1.77 | S/F | VPH850+O58 | -19.68 | 18.09.19 | 300 × 2 |
| 17 | J2205+0031 | 331.254974 | 0.523022 | 1.6520 | 1.07 | S/F | 300B+Y47 | -90.15 | 19.09.18 | 600 × 2 |
| 18 | J2208+0238 | 332.048207 | 2.641707 | 3.1790 | 2.36 | S/F | 300B+Y47 | 33.03 | 19.09.18 | 600 × 2 |
| 19 | J2217+0604 | 334.498273 | 6.073975 | 2.5720 | 2.44 | S/F | 300B+Y47 | -69.9 | 19.09.18 | 600 × 1 |
| 20 | J2220+0003 | 335.239338 | 0.058294 | 2.2600 | 1.79 | S/F | 300B+Y47 | -93.64 | 19.09.18 | 600 × 1 |
| 21 | J2212+0051 | 333.115601 | 0.861267 | 1.7725 | 1.77 | S/F | 300B+Y47 | -10.33 | 19.09.18 | 600 × 1 |
| 22 | J2303-0014 | 345.844781 | -0.243969 | 3.2220 | 2.25 | S/F | 300B+Y47 | 6.32 | 19.09.18 | 600 × 2 |
| 23 | J2337+0056 | 354.306946 | 0.936338 | 0.7078 | 2.21 | S/F | 300B+Y47 | 14.32 | 19.09.18 | 600 × 2 |
| 24 | J0005+0108 | 1.284879 | 1.135122 | 1.3131 | 1.54 | S/F | 300B+Y47 | 35.74 | 19.09.18 | 600 × 2 |
| 25 | J0008-0103 | 2.156927 | -1.053815 | 1.3697 | 1.75 | S/F | 300B+Y47 | -13.02 | 19.09.18 | 600 × 1 |
| 26 | J0213-0211 | 33.469467 | -2.191526 | 2.7800 | 2.99 | S/F | 300B+Y47 | 53.5 | 19.09.18 | 600 × 2 |
| 27 | J0221-0145 | 35.498804 | -1.753334 | 2.3600 | 2.72 | S/F | 300B+Y47 | -92.81 | 19.09.18 | 600 × 1 |
| 28 | J2337+0056 | 354.306946 | 0.936338 | 0.7078 | 2.21 | G/G | R831+RG610 | 14.32 | 08.09.19 | 605 × 3 |
| 29 | J0127-0035 | 21.817378 | -0.599352 | 0.3713 | 1.50 | G/G | R831+RG610 | -3.87 | 08.09.19 | 605 × 2 |
| 30 | J0203-0623 | 30.828645 | -6.389267 | 2.1600 | 1.12 | G/G | R400+OG515 | -81.65 | 08.09.19 | 840 × 3 |
| 31 | J2205+0031 | 331.254974 | 0.523022 | 1.6520 | 1.07 | G/G | R831+OG515 | -90.15 | 24.09.19 | 605 × 3 |
| 32 | J2202+0049 | 330.619415 | 0.817198 | 1.4482 | 1.22 | G/G | R831+RG610 | 65.64 | 24.09.19 | 605 × 3 |
| 33 | J2229+0104 | 337.372742 | 1.077335 | 1.4447 | 1.21 | G/G | R831+OG515 | -39.28 | 25.09.19 | 605 × 3 |
| 34 | J0221-0441 | 35.273505 | -4.683758 | 0.1990 | 1.23 | G/G | R831+OG515 | 83.13 | 25.09.19 | 225 × 4 |
| 35 | J0941+0007 | 145.387085 | 0.125333 | 0.4889 | 1.05 | G/G | R831+OG515 | -49.81 | 19.12.19 | 605 × 4 |
| 36 | J1238+0105 | 189.590281 | 1.088519 | 3.1590 | 1.01 | G/G | B600+CG455 | -80.34 | 24.12.19 | 847 × 2 |

## 2.3 Spectroscopic Data Reduction of Subaru/FOCAS observations.

The reduction of FOCAS data was carried out with **focasred** package in the Image Reduction and Analysis Facility (IRAF) software tools. We followed the procedure as described in the Subaru Data Reduction CookBook by T. Hattori and N. Kashikawa for FOCAS long-slit data.

### 2.3.1 Raw Data

The process to take the raw 2D spectroscopic data to final science-ready 1D spectra is shown in Figure 2.5 panels (a)-(d). First, Given the sky coordinate of the target (RA and Dec), an image is taken to locate the position of the target (panel (a) and (b)). Then given the position angle, a slit is inserted to disperse the light (panel (c) and (d)). Basically, if the target is a single point source, the position angle of the slit doesn't matter much, if it is an extended source, then the observers may interested in trying different angles to take spectrum from different parts of the source. For our purpose, since we are looking for dual point sources, we prefer to take the spectrum of them at the same time. Therefore, the position angle of the slit is set to be equal to the position angle of the two sources. Panel (e) and (f) show an example for SDSS J220228.65+004901.9, one of our targets observed at the first night of observation. Panel (e) is the image taken by the CCD camera of FOCAS with a 10s exposure, which is divided into four channels. We can find the pair in the third channel, the camera is already rotated so that they are aligned along the horizontal direction, corresponding to panel (b). Panel (f) corresponds to panel (d). It is dispersed from a horizontal slit across panel (e). Note that panel (f) is rotated by 90 degrees for layout purpose, so the x and y axis are shifted compared to panel (d). In panel (f), the x-axis is the wavelength direction and y-axis is the spatial dimension. Our target is in the second panel, which shows a bright line (actually two) along the x-axis. The radiation from astronomical objects like stars, galaxies and quasars usually cover a wide range of wavelength but limited in the spatial dimension, while emission from earth's atmosphere only takes a single wavelength but covers the full spatial region along the slit as shown by the vertical bright lines. They appear in all ground based observations. Fortunately, IRAF offers tools to get rid of these lines and use them to check our calibration. Our final goal is to extract useful information from this 2D spectrum, the most reasonable way is to keep the horizontal bright line only and plot it as a 1D spectrum. The image data will not be used as it only works as a guidance for

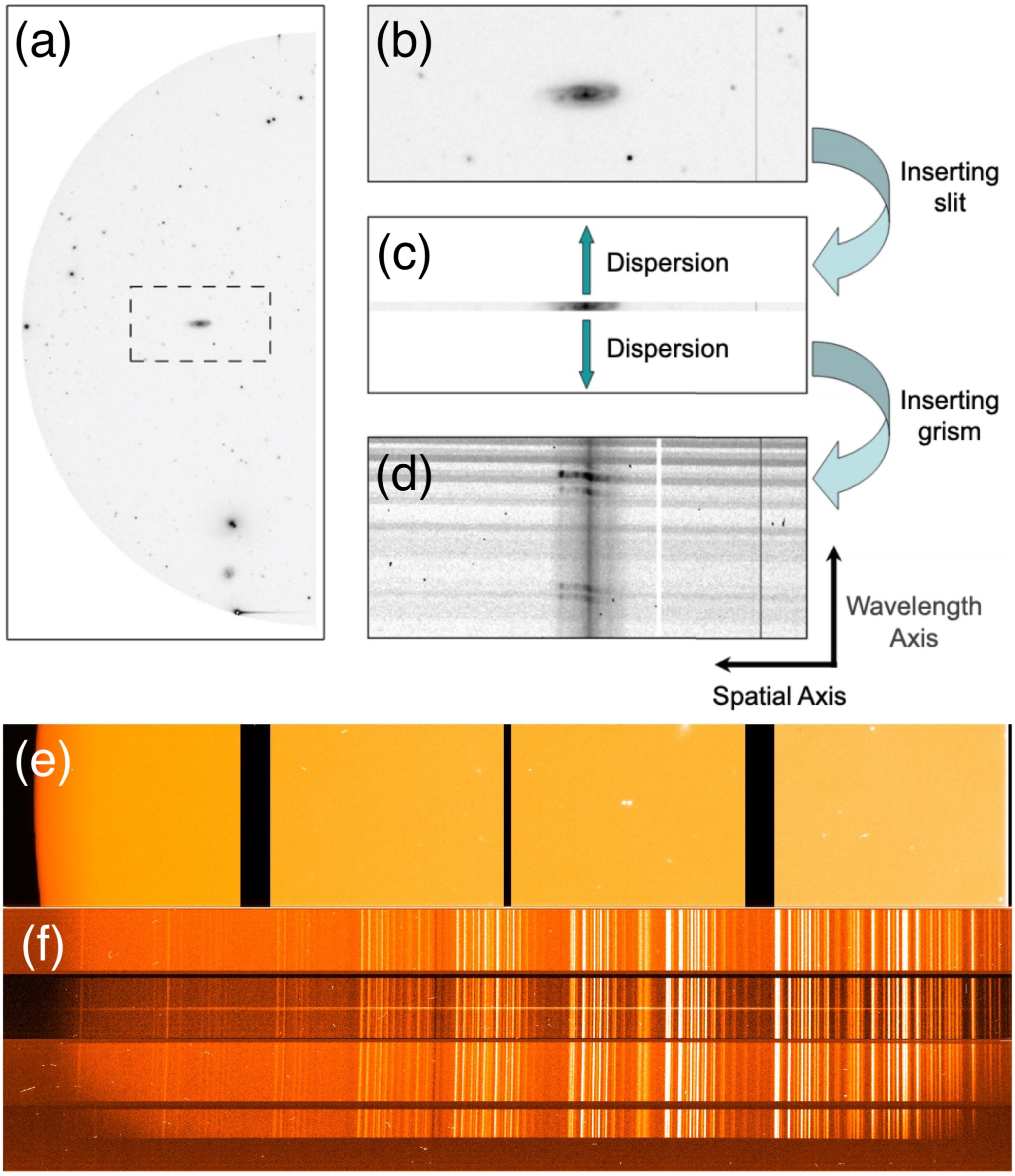


Fig. 2.5: (a)-(d) Adopted from Figure 2 of the Subaru/FOCAS cookbook by T. Hattori and N. Kashikawa. Concepts of long-slit observations. Panel (e) is the image of the candidate, panel (f) is the raw 2D spectroscopic data. See details in the text.

observation in our observation. Here, we describe in detail the data reduction steps.

### 2.3.2 Bias Subtraction

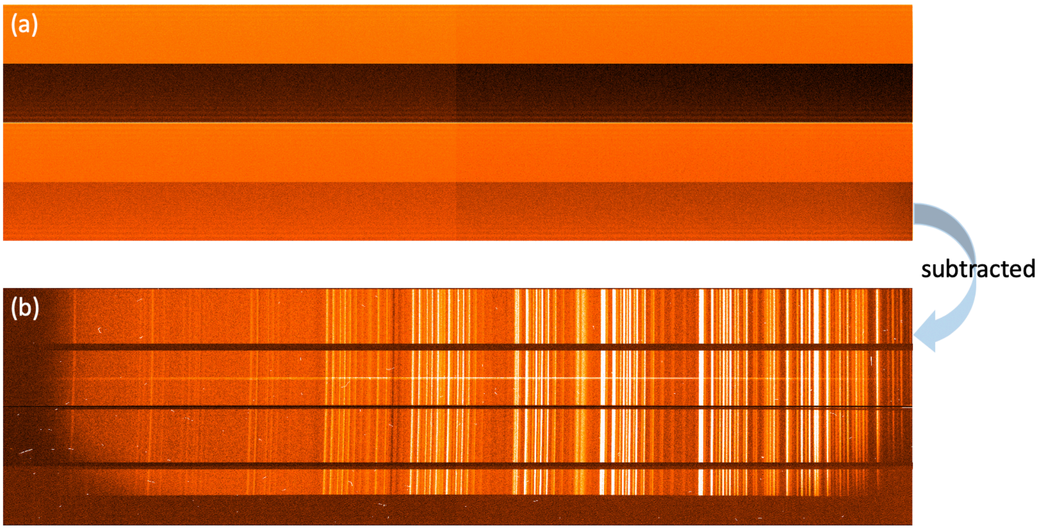


Fig. 2.6: Example of bias subtraction. (a) Averaged bias frame. (b) The result of figure 2.5 panel (f) subtracting panel (a).

With the raw data in hand, we first proceed with bias subtraction. Bias images are taken before or after each observation with an exposure time of zero seconds. The signal comes from the dark current with the detector. In our case, the counts vary from 520 $\sim$ 540 for each pixel. As multiple bias images are taken, we take the median value of them using the **imcombine** task to get the standard bias image (figure 2.6 panel (a)). Then we subtract this standard bias image from each of our raw science frame using **imarith** task to get rid of these unwanted signals. The result of SDSS J220228.65+004901.9 is shown in panel (b).

### 2.3.3 Flat Fielding

The sensitivity of pixels differ from each other, that will affect our signal. Dome flat images are taken before (i.e. twilights) or after (i.e. dawn) each observation. It provides us a sensitivity map to flatten this inequality. Before flat fielding, we preprocess the images to trim the bias subtracted image first. Since our source spectrum only falls in the third channel, we use this that

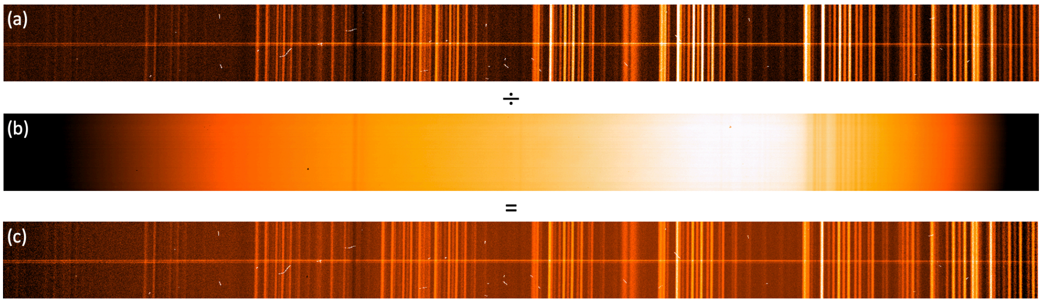


Fig. 2.7: Example of flat-fielding. (a) Cut of the data from previous step. (b) Normalized dome flat image, showing the sensitivity map of pixels. (c) The result of dividing (a) wihh (b).

channel only (figure 2.7 panel (a)). The dome flat image is also cut to the same size. The count levels of the dome flat image are around 10,000. We normalize it with the median value to produce the sensitivity map (panel (b)). Then we divide our science frames by the 2D sensitivity map to achieve flattened data (panel (c)).

### 2.3.4 Cosmic Ray Removal

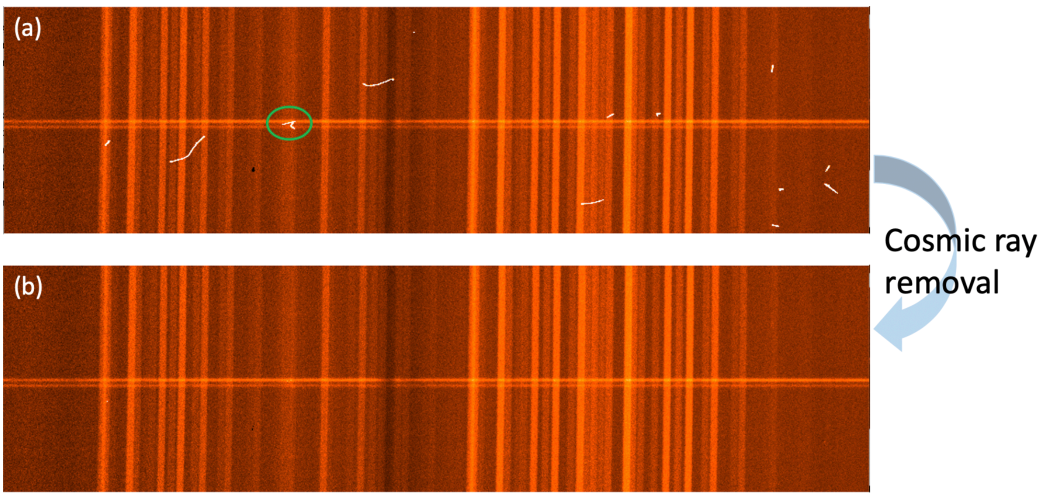


Fig. 2.8: Cosmic ray removal. (a) Zoom in of the flattened data, green circle labels an event that locates on our scientific data. (b) The same region after cosmic ray removal.

Cosmic rays are high-energy protons and atomic nuclei moving through space at a relativistic speed. When they accidentally hit the CCD camera, they will leave a spark on the image. For a long flip the order, there could be hundreds to thousands of such events. Mostly, they appear over the background region of the image for spectroscopic observations. but they sometimes unfortunately fall exactly on the spectrum (Figure 2.8 panel (a), labeled with a green circle). A common way to deal with such cases is to require multiple exposures of the same field. Since comic rays are random events, they only appear on one single exposure, so combining multiple exposures to take a median value will eliminate them. However, this method requires at least three exposures, while there are circumstances in our observations that only one or two exposures are taken. Van Dokkum (2001) provided the **L.A. COSMIC** package that is usable to reject cosmic ray events with arbitrary shapes and sizes from single exposure images [117]. The algorithm is based on a variation of Laplacian edge detection, which can identify the sharp edges of the cosmic ray events. For each image, the task loops through the algorithm four times by default to reach a satisfying result. Parameters of detection sensitivity and loop times can be modified for more sophisticated use. Figure 2.8 (panel b) shows the result after applying this method to our data.

### 2.3.5 Sky Subtraction

Next we consider the sky background using regions that are free of sky emission lines to estimate the background level. We use the **background** task in IRAF, with a specification of the range of wavelength. Stacking the data in that range will call out a window like figure 2.9 panel (a). The figure shows the average counts along the spatial axis with the two peak representing our targets. Then we select a background region on both sides of these two peaks as we believe there is only sky signal present (the two "H" shape markers in the window). Notice that the average counts of the background is around -10, this is caused by over subtracting the bias frame. The dark current may vary depending on the status of the telescope, since the bias frame is not taken at the exactly same time as our scientific data, the status may differ a little, in this case the counts differed by $\sim 2\%$, the **background** task will be used to rectify this. By fitting the background emission with a given function (e.g., third order chebyshev function), automatically recognizes the sky lines in selected regions and eliminates them. The result is shown in panel (b). Now only our scientific data is left in the field and the average count of the background is around 0.

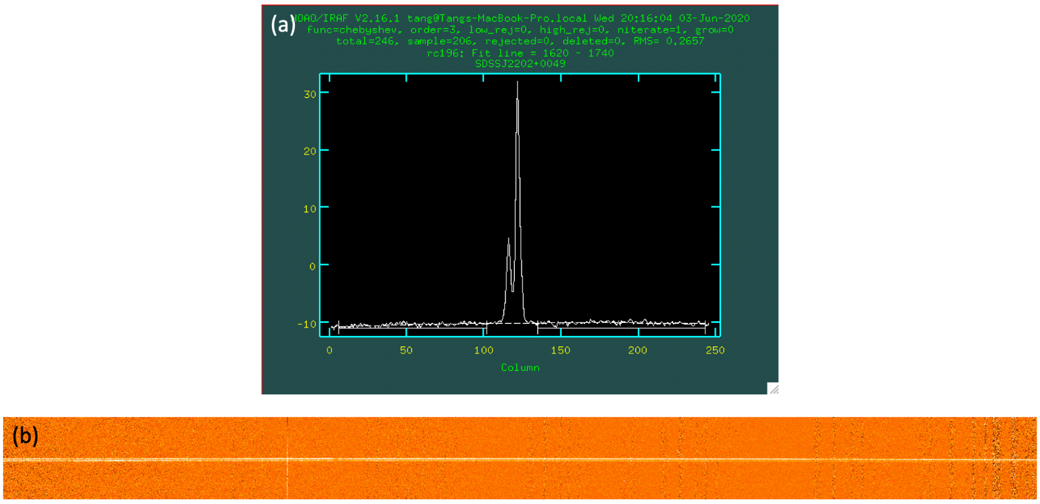


Fig. 2.9: (a) Call **background** task in IRAF, x-axis is the spatial axis, y-axis is average counts along the wavelength axis. (b) Output data after sky-subtraction.

### 2.3.6 1D Extraction

The main task of the data reduction procedure, **apall**, whose main functionality is to extract the data from the 2D spectrum, is executed. There are many parameters that need to be set prior to completing the extraction. The task will first automatically choose a region along the wavelength axis (lines 1638 to 1652 as shown in figure 2.10 panel (a)) and stack the counts onto the spatial axis. We can see a similar spatial profile as Figure 2.9 (panel a). I then set an aperture for the right brighter source in the window. The task will trace this aperture along the wavelength axis and finally sum the data along the spatial axis to get a 1D spectrum. Here I set the lower limit to be around position 120, so that the aperture will not be contaminated by the left source. Panel (b) shows the trace of this target, each data point is the peak position at that column. The trace is fitted with a fourth order legendre ploynomial, giving a curve that is the trajectory it is going to follow. We can see that the trace in the 2D spectrum is distorted, but the apall task will help us to trace the spectrum accurately. Panel (c) shows the background removal task result, where our 2D data is extracted to 1D. The x-axis is wavelength, and the y-axis is the counts at that wavelength, within the aperture. Since we haven't applied the calibration yet, the numbers do not have physical meaning, but the shape itself is reasonable. We can see some broad emission and absorption features. Note that we only extracted one source, we have

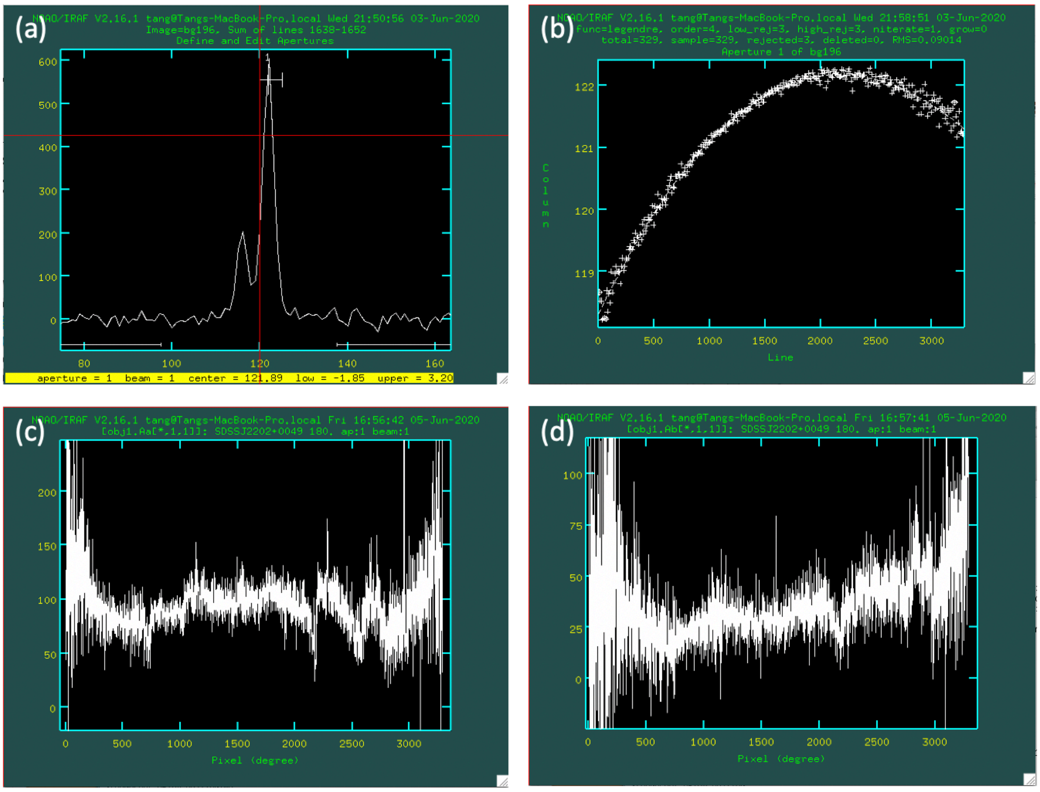


Fig. 2.10: 1D spectral extraction. (a) Call **apall** task in IRAF, the aperture of one of the sources are selected, x-axis is the spatial axis, y-axis is stacked counts. (b) Trace of this source along the wavelength direction, x-axis is the wavelength axis, y-axis is the spatial axis, we can see the line is actually curved, but apall task will help us to keep on it. (c) Extracted spectrum of the right source in panel (a). (d) Extracted spectrum of the left source in panel (a).

to call the task again to extract the other object within the pair (i.e. the left source). Panel (d) shows the result for that source where we can also see some emission features at a similar position to the right source (around pixel position 2700), indicating that this could be a good dual quasar candidate!

### 2.3.7 Wavelength Calibration

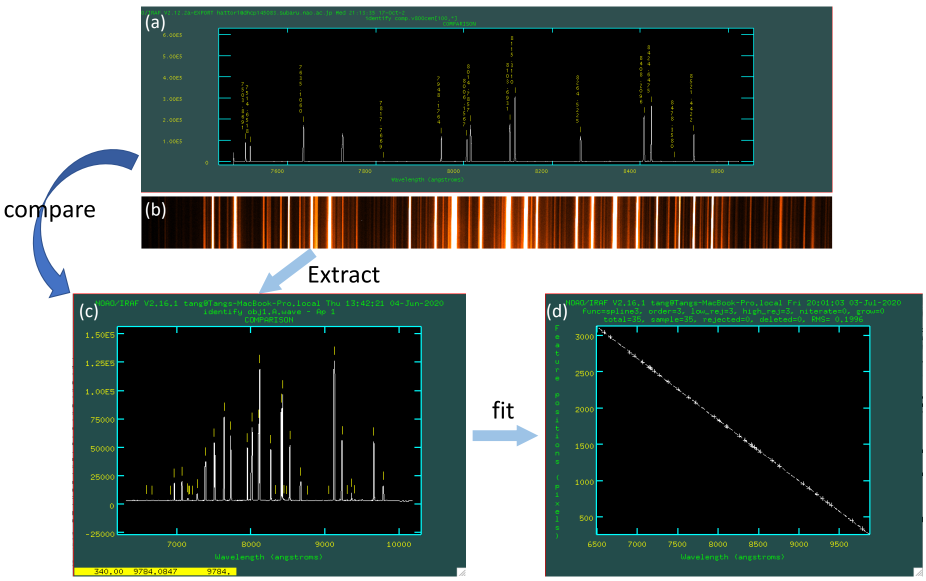


Fig. 2.11: Wavelength calibrations. (a) Parts of the ThAr lamp template provided by FOCAS. (b) Arc lamp image taken for our first night observation using FOCAS/VPH850. (c) Arc lamp extracted to 1D using **apall** task. (d) The solution of wavelength calibration, an almost linear relationship is established between pixel coordinates and physical coordinates.

The next step is to calibrate the pixel coordinate to real wavelength units of Å. For this purpose, an arc lamp image is taken for each observation using the same instrumental setup as the scientific data, whcih only contains the arc lines generated by the lamp of the telescope (figure 2.11 panel (b)). Then we call **apall** task again to extract an 1D data array from this arc lamp image following the same trajectory got from the previous step. This gives panel (c), now the arc lines are shown in 1D dimension. The x-axis is the wavelength direction and the y-axis is the counts. We then compare the positions of these arc lines with a template (panel (a)) to mark the lines with known wavelength (yellow marks there). Then push "f" so that it will fit a solution based on the wavelengths provided. This leads to panel (d), where the relationship between the pixel coordinates and physical coordinates is established. The solution is almost linear, although the data points there only cover 6500 Å to 10,000 Å. The program will extrapolate to the full coverage of FOCAS/VPH850, which is 5800 Åto 10350 Å. Recall the existence of sky lines, although they are a nuisance for our scientific data, a positive aspect is that since they are registered on every spectrum, they thus provide a potential wavelength calibration or zero-point determination for the spectrum without taking time-consuming comparison to decide the redshifts for each of the source [118, 119].

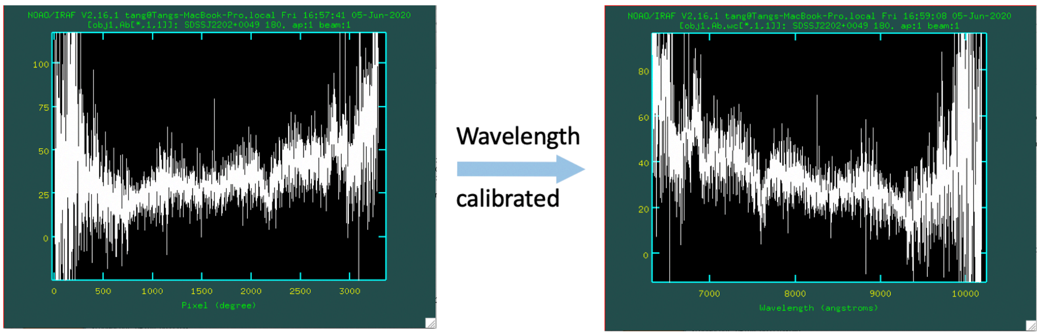


Fig. 2.12: Wavelength calibration. Left: the same as figure 2.10 panel (c), spectrum before wavelength calibration, x-axis is pixel coordinates. Right: spectrum after wavelength calibration, x-axis is physical coordinates.

This solution is then saved as a ".fits" file to calibrate our scientific data. Then call **dispcor** task to disperse it into wavelength coordinates. Now we see the x-axis of our data has been calibrated from pixel coordinates to physical coordinates (Figure 2.12). The direction is flipped as the solution indicates in Figure 2.11 panel (d).

### 2.3.8 Flux Calibration

As we have calibrated the x-axis, the y-axis is still in "counts" of photons that the CCD camera captured. We need to correct it to physical units: flux density. For this purpose, we use the same instrument to observe a standard star whose flux density is already known, thus providing us with a relationship between the flux density and counts. For the FOCAS run, we observed G191B2B, a white dwarf that is commonly used for this purpose [120]. Its 2D spectrum is shown in Figure 2.13 panel (a). Again, as we did before, we call **apall** task to trace the spectrum (panel (b) and (c)), **refspec**

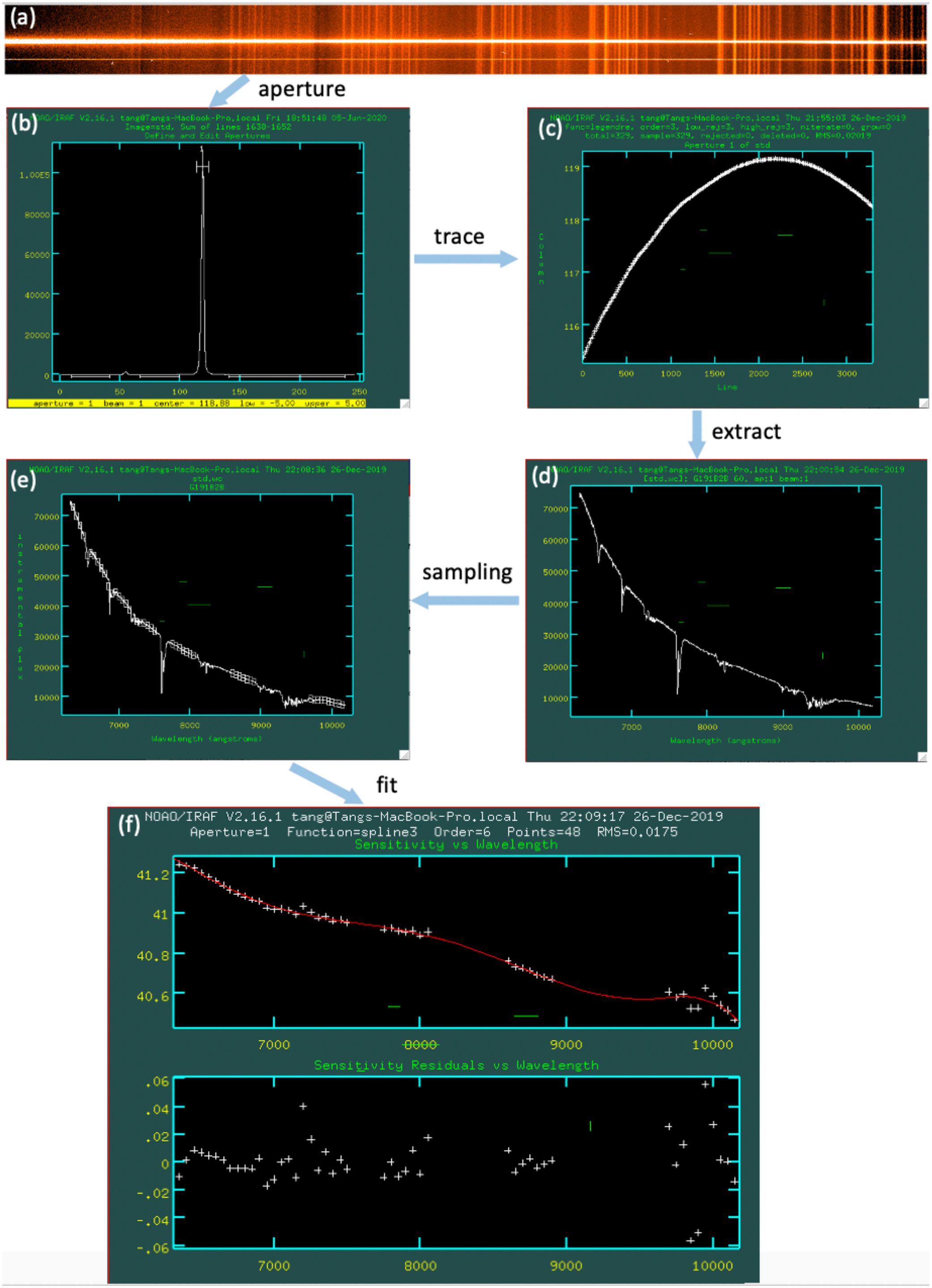


Fig. 2.13: Flux calibration. (a) 2D spectrum of standard star G191B2B. (b)-(d) Call **apall** task to extract it into 1D spectrum. (e) Call **standard** task to sampling data from the spectrum. (f) Call **sensfunc** task to fit the sampling data and make a sense function file to calibrate the flux.

task will calibrate the wavelength of the spectrum and make it a reference 1D spectrum to proceed (panel (d)). Then call **standard** task to bin and sampling data from the spectrum (panel (e)). The size of each box indicates the bandwidth where a catalog value has been measured. This outputs an ASCII file. Using the results, we subsequently fit the data with the **sensfunc** task to build a relationship between counts and energy density (panel (f) upper half, lower half shows the residuals of fitting). Besides, we set the *extinct* parameter in this task to correct the extinction due to atmosphere with an input of airmass at observation for each target. Finally, a ".fits" format sense function file is made. We call the task **calib** to apply it to our wavelength calibrated scientific data. Besides the standard flux calibration with IRAF, we also rescaled the spectrum with respect to HSC magnitudes to make sure it agrees with the photometry.

### 2.3.9 Finishing Touches

The main work of data reduction is done after flux calibration. The spectrum is now more readable than it was in 2D and has physical units (Figure 2.14 panel (a)). But there are still something else we can do to polish our results. First, most of our targets are exposed more than one time, which means we will have multiple scientific images for one target, thus multiple 1D spectrum. We can combine these 1D data array with the task **scombine** to take the median value of them. This on the one hand improves the signal to noise ratio and on the other hand, removes outliers (panel (b)). To assist identifying the features, we may smooth the spectrum by a factor, in panel (c) I smoothed by 10. The broad feature we saw before is really there! To estimate the spectrum further, one can keep in IRAF, but python also provides many useful packages to deal with the data. Personally, I prefer to work in python. If we would like to proceed with ".fits" format data, we may use the **astropy** package. But an ASCII, ".txt" or ".csv" format file will be much easier to deal with, as python has very strong data analysis packages like **numpy** and **pandas** that work well with these formats. To convert ".fits" file to text format, call **wspectext** task in IRAF. After reading the data into python, visualization can be performed use **matplotlib** or **seaborn** packages. Here I overplotted the spectrum of the two sources in SDSS J220228.65+004901.9, red curve is the known quasar from SDSS (say source A) and blue curve is the unknown source (say source B). Dashed lines are a quasar template provided by SDSS, overlayed here as a comparison. The positions of emission lines of the main quasar are labeled with green dashed lines. We find that broad feature in source B is quite close to the broad MgII line in source A. That is what we really want to see, because this is a signal that the unknown source

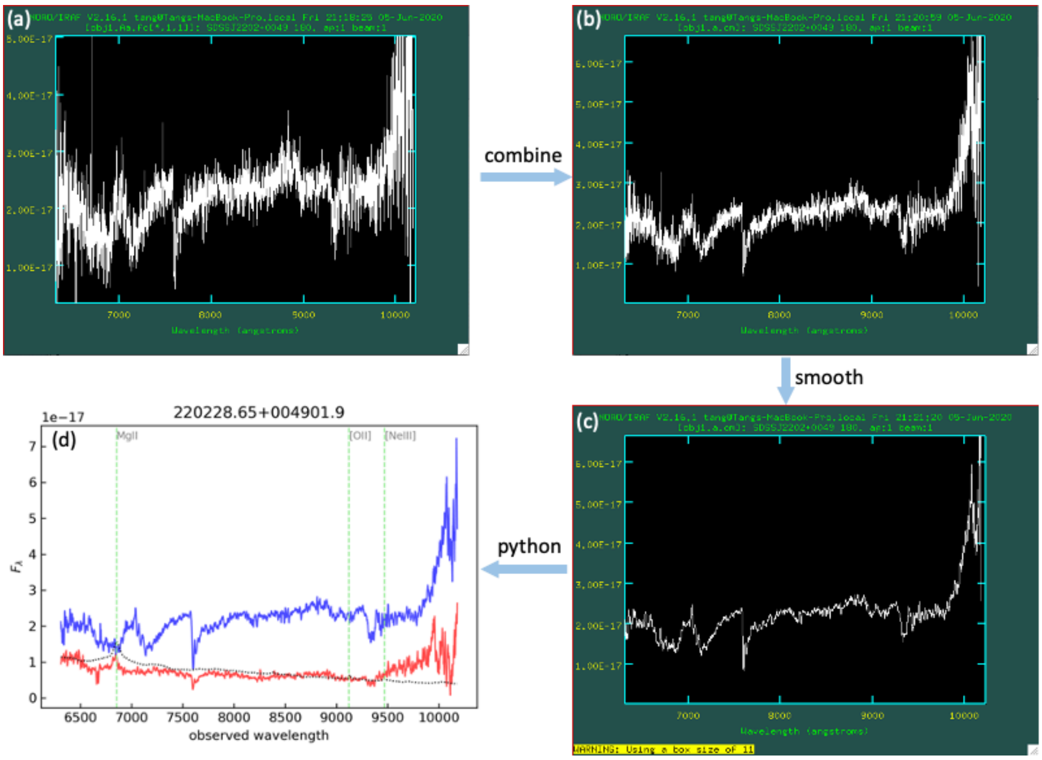


Fig. 2.14: Combining individual 1D spectra. (a) Flux calibrated 1D spectrum. (b) Combined spectrum from multiple frames. (c) Panel (b) smoothed by a factor of 10. (d) Read the data in python and overplot two sources together. Red curve is the known quasar, blue curve is the unknown source, dashed line is a quasar template from SDSS. The positions of emission lines of the known quasar are marked with green dashed lines.

could be a quasar at the same redshift as the known quasar, thus form a pair! We will revisit this source later in the classification section to see whether it is true.

### 2.3.10 Quick Notes on LRIS and GMOS Data

As I used the FOCAS spectrum as an example for data reduction, basically, LRIS and GMOS longslit data also follows similar steps. The main difference of LRIS is that the data is taken with a red arm and a blue arm simultaneously but output separately. Thus there will be two parts of spectrum for each source, which we have to concatenate them together using some more strategies. GMOS data is somewhat more complicated. It is taken with 3 chips and saved in 12 extensions with a 32-pixel wide overscan section for each. So before proceed with data reduction, some preprocesses are required, which can be performed in python with the **PyAstronomy** package. One must be careful about the gaps of the chips, as that could lead to an offset when calibrating the wavelength.

# Chapter 3

# Results

In this chapter, we will discuss the observational results of this program to date. At first, Section 3.1 will describes how we classify these targets based on a matching of spectrum with SDSS templates and HSC imaging. Based on which, we summarize the success rate of this program. Here, we define a successful detection as a physically associated quasar pair. We will show how this rate dramatically changes depending on the color of the candidates and how they deviate in color from single quasars. Besides the physically associated quasars, we also discovered projected quasars and physically associated quasar-galaxy pairs. Section 3.2 will then show the detailed information of the imaging and spectroscopy data of these candidates and discuss their properties.

## 3.1 Classification

### 3.1.1 Overview

To confirm a dual quasar system, we classify the companion based on its optical spectrum. Using 33 SDSS spectral templates, we use a simple interactive tool using python **bokeh** package [121] to inspect each spectrum in 1D and 2D. Figure 3.1 shows examples of a quasar, a galaxy and a star. Typical emission and absorption lines are labeled with green and orange dashed vertical lines. Besides the spectrum, we also display the HSC image.

Generally, when broad emission lines (with Doppler width from 1000 $\mathrm{km\,s^{-1}}$ to 25,000 $\mathrm{km\,s^{-1}}$) such as C IV $\lambda$1549, H$\beta$, H$\alpha$, Mg II $\lambda$2789 and C III] $\lambda$1909 are observed, we classify the companion as a quasar. Furthermore, broad absorption lines are not uncommon among quasars [122], typically C IV may form a so-called "P-Cygni" profile, with a broad absorption feature

Table 3.1: Spectral classification

| Name | Type | $z_A$ | $z_B$ | AGN activity | Merger | Comments |
|---|---|---|---|---|---|---|
| J0004-0001 | Early-type galaxy | 0.5812 | 0.4037 | P | N | moderate Hα emission observed |
| J0005+0108 | Early-type galaxy | 1.3545 | 0.3649 | N | N | based on absorption lines |
| J0008-0103 | Unclassified | ? | ? | ? | ? | noisy |
| J0119-0020 | M3 star | 0.8597 | 0 | N | N | blended spectrum |
| J0127-0035 | Unclassified | 0.3611 | ? | N | P | visible disturbed feature in main source |
| J0203-0623 | F star | 2.07 | 0 | N | N | flat spectrum with a few absorption lines |
| J0213-0211 | Quasar | 2.778 | 2.844 | Y | N | only C IV observed |
| J0219-0556 | Quasar/Seyfert | 0.2905 | 0.2907 | Y | Y | according to WHAN diagram |
| J0221-0441 | Galaxy | 0.1934 | 0.1949 | Y | Y | according to WHAN diagram |
| J0221-0145 | Unclassified | 2.343 | ? | ? | N | noisy |
| J0847-0013 | Quasar | 0.6255 | 0.6268 | Y | P | type1-type1 |
| J0848+0115 | G star | 0.6457 | 0 | N | N | a triple source system |
| J0903+0020 | M1 star | 0.4124 | 0 | N | N | well-matched |
| J0941+0007 | Galaxy | 0.4819 | 0.1287 | N | N | weak Hα |
| J0949+0005 | Unclassified | 0.4220 | ? | ? | N | noisy |
| J1214+0102 | Quasar | 0.4916 | 0.4935 | Y | P | type1-type1 |
| J1238+0105 | BAL Quasar | 3.103 | 3.13 | Y | P | type1-BAL |
| J1416+0033 | Quasar | 0.4331 | 0.4327 | Y | Y | type1-type2 |
| J2202+0049 | M1 star | 1.445 | 0 | N | N | well-matched |
| J2205+0031 | A star | 1.6364 | 0 | N | N | Hα absorption observed |
| J2207-0017 | Galaxy | 0.7068 | 0.3875 | N | N | moderate Hα emission observed |
| J2208+0238 | F star | 3.172 | 0 | N | N | Hα and Na absorption observed |
| J2209+0045 | Quasar | 0.4457 | 0.4456 | Y | Y | type1-type1 |
| J2211-0000 | F star | 0.4769 | 0 | N | N | based on absorption lines |
| J2212+0051 | F star | 1.767 | 0 | N | N | featureless spectrum |
| J2217+0604 | Early-type galaxy | 2.569 | 0.8248 | N | N | based on CaII H & K absoption |
| J2220+0003 | Unclassified | 2.265 | ? | N | N | featureless |
| J2229+0104 | Early-type galaxy | 1.445 | 0.137 | N | N | possible lens |
| J2251+0016 | Quasar | 0.4076 | 0.577 | Y | N | projected pair |
| J2303-0014 | Early-type galaxy | 3.215 | 0.589 | N | N | ambiguous |
| J2311-0013 | Early-type galaxy | 0.3456 | 0.345 | N | P | possibly broad Hα |
| J2328+0112 | Unclassified | 0.5265 | ? | ? | ? | extremely extended [O III] in main source |
| J2337+0056 | Quasar | 0.701 | 0.699 | Y | Y | type1-type1 |

Column (2): Type of the companion based on SDSS templates.
Column (3) & (4): Redshifts of the two sources estimated by template matching.
Column (5): Whether the companion has AGN activity, Y: Yes, N: No, P: Potential.
Column (6): Whether they are a merger, based on HSC images.
Column (7): Comments on the companion's spectrum, if not specified 'main source'.

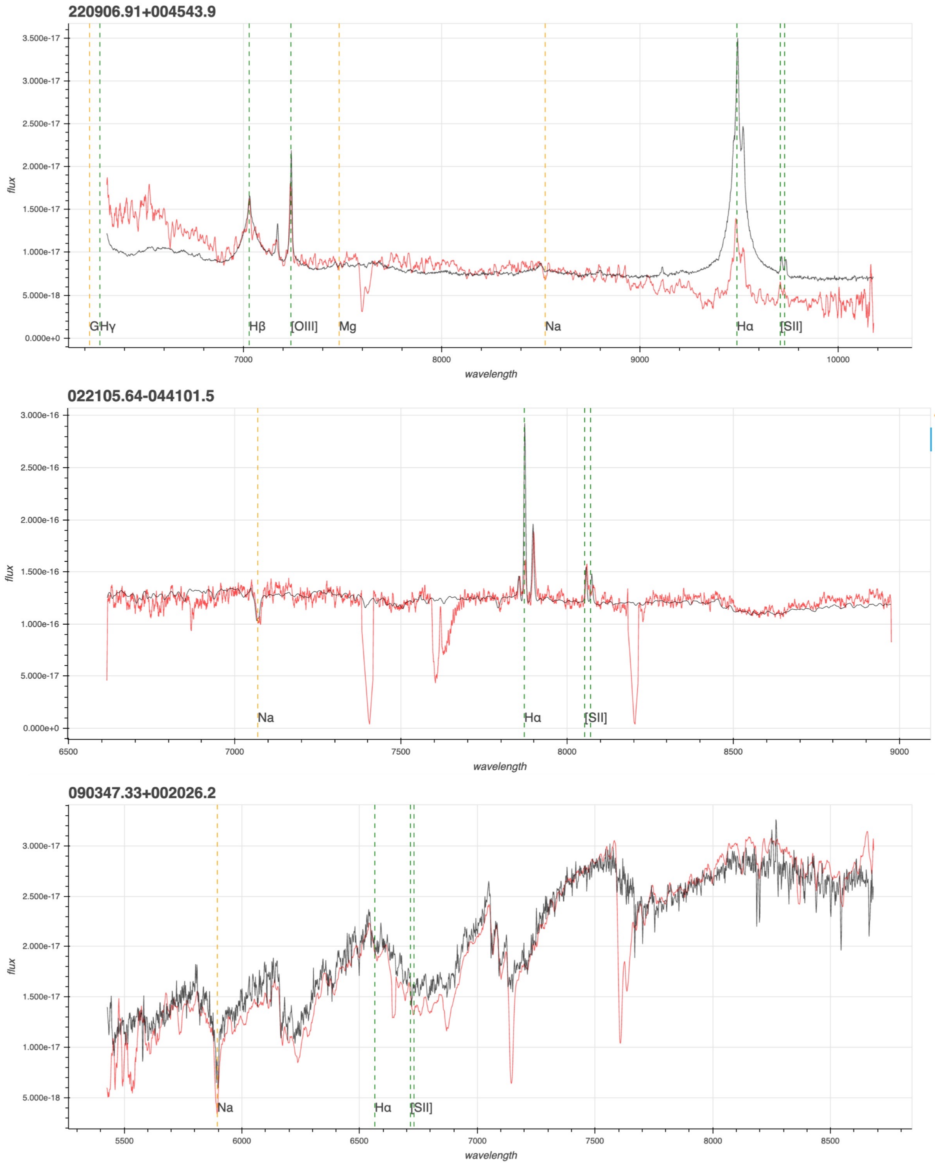


Fig. 3.1: Examples of visually-matched SDSS templates with observation data, see details in section 4. Top: A matched quasar spectrum at redshift of 0.4456. The drop at 7600 Å is the sky absorption line. Middle: A galaxy spectrum at redshift 0.199. The drop at 7400 Å and 8200 Å are the gaps of the chips. Bottom: A matched M1 star spectrum. Red curves show our data, black curves are SDSS templates, green vertical dashed lines label the position of some main emission lines, and orange vertical dashed lines label the position of some main absorption lines.

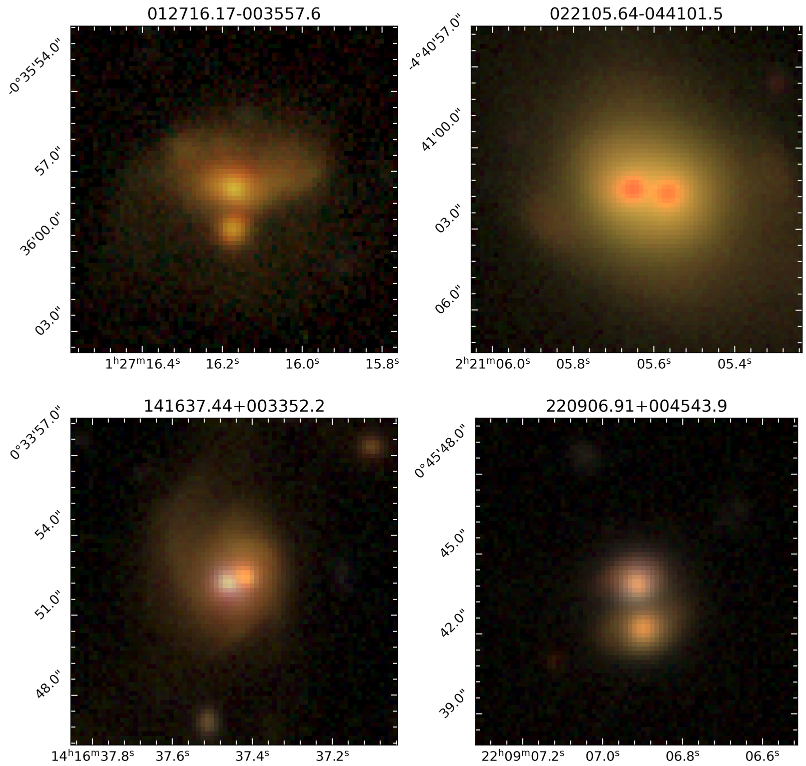


Fig. 3.2: HSC image of four possible merging systems in this program. Left upper panel is an unclassified system that we are not able to tell what is the companion source because of bad S/N ratio, but we can see the HSC image shows disturbed feature of the quasar's host galaxy. Right upper panel is an ambiguous quasar pair, they are so close to each other that the image shows they share their host galaxy. The bottom two panels are two secure quasar pairs, elongated features can be seen in their images.

impacting the blue wing of the core emission. In these cases, we classify them as a "BAL (Broad Absorption Line) quasar". With respect to galaxies, late-type and early-type galaxies can be identified by the existence of narrow emission lines such as the [O III] $\lambda\lambda$4959, 5007 doublet or the presence of only absorption lines such as Na or Ca H+K. Faint main sequence stars can be challenging to classify due to their featureless spectrum. The optical photometry from HSC does help to identify stars by their relative location to the well established stellar locus (Figure 3.4). M stars are a special case, since they often have strong molecular OH bands, causing their spectrum to be very rugged (see Figure 3.1 bottom panel as an example). In some cases, because of the limitation of the wavelength coverage, spatial resolution, or S/N ratio, we were not able to obtain enough information to classify our candidates. The spectrum could either be featureless, hard to match to any known lines, or could just be heavily impacted by noise. These cases are noted as "unclassified" with reasons given in the "comments" column of table 3.1.

Regarding our classification scheme, there are two properties of the companions that we care about, the first being the AGN activity. For some candidates, the classification is ambiguous, thus there is no evidence for an AGN, e.g. the emission line is not so broad, or only one axis of the BPT diagram ("Baldwin, Phillips & Terlevich" diagram), used to distinguish LINERs can from normal HII regions and AGNs based on their [O III] $\lambda$5007/H$\beta$, [N II] $\lambda$6583/H$\alpha$, and [S II] $\lambda\lambda$6716,6731/H$\alpha$ flux ratios [123], [124], is available.

In such cases, we provide a designation "P" standing for potential. Another property is whether there are signs of an ongoing merger, this is mainly suggested from the HSC images, where disturbed features such as tidal tails are seen. We give a "Y" indicating a positive judgement for this column. In Figure 3.2, we show some examples of quasars in mergers. We found resolved candidates at same redshift do tend to have such features in their images, but when the redshift is too high, the source is unresolved, we give a "N" or "P" note for these cases.

### 3.1.2 Calibration of Color from SDSS to HSC

Before the discussion about color, as we sometimes would like to compare the color of our targets to that of SDSS data, we are always facing the problem that the photometry system of SDSS and HSC are different. e.g. g band in SDSS does not exactly cover the same wavelength rage as g band in HSC. Figure 3.3 proves this. Using SDSS data from [12], we plot a so-called "stellar locus" as shown by the red line in the bottom left panel of Figure 3.3. This curve represents an average distribution of the color of SDSS stars.

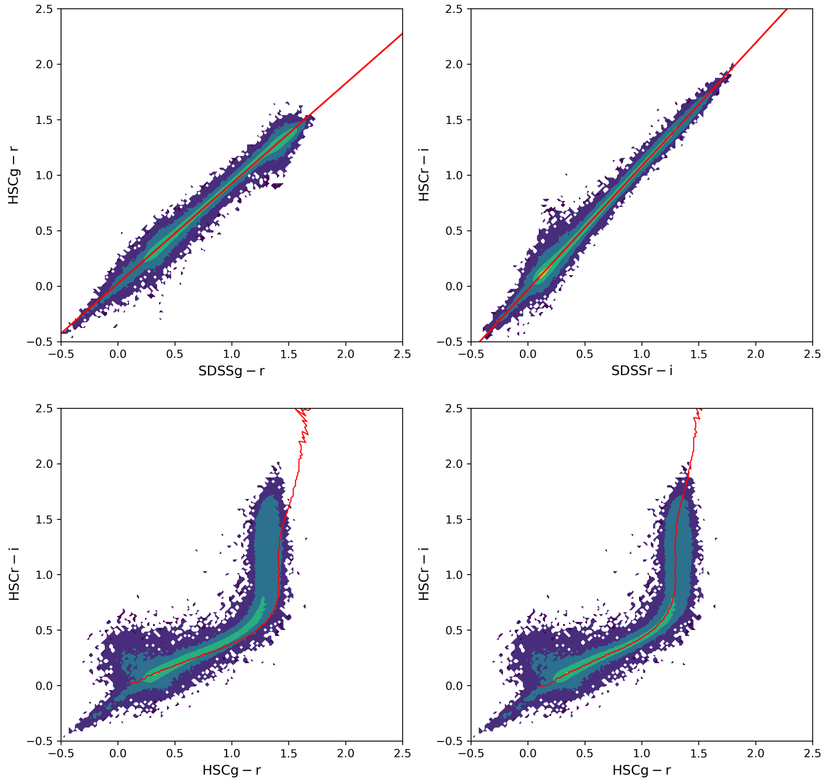


Fig. 3.3: Calibration of the stellar locus to the HSC photometric system. Upper panels: linear regression applied to HSC and SDSS colors, red lines are the regression results, contours are a set of stars queried from Stripe 82 data. Lower panels: stellar locus of [12] before and after correction to HSC, contours are the same set of data as above.

We compare that to a set of 619,634 stars with HSC photometry, shown as the contours. They are plotted in the color-color diagram. We can see that stellar locus has a significant shift from the data set. Therefore, a calibration is required. Here we assume a linear relationship between SDSS and HSC color, i.e.

$$(g-r)_{HSC} = k1 * (g-r)_{SDSS} + b1 \tag{3.1}$$

$$(r-i)_{HSC} = k2 * (r-i)_{SDSS} + b2 \tag{3.2}$$

The upper panels of figure 3.3 show the results of linear regression indicating k1 = 0.90093, b1 = 0.02389, k2 = 1.11105, b2 = -0.03081. We then apply these two relations to the stellar locus. The calibrated stellar locus is plotted in the lower right panel, while compared to the same data set of stars from HSC. In following sections, whenever SDSS color is used, this calibration is applied.

### 3.1.3 Spectroscopic Success Rate with Optical Color Distribution

As listed in Table 3.1, we confirmed 7 quasar pairs out of 33 targets observed in this work, giving a total success rate of $\sim 21\%$ for finding physically associated quasar pairs, plus 1 extra quasar pair selected out from SDSS/BOSS spectrum. In addition, we identified 2 quasar-galaxy pair and 2 projected quasars (quasar pairs with velocity offset larger than 2000 $\mathrm{km\,s^{-1}}$). Therefore, the success rate for identifying quasars in this study is $\sim 27\%$.

Figure 3.4 provides a guide of these results in color-color space, note that only the companions are plotted here. In left panel, the blue curve is a stellar locus adopted from [12], which shows the average distribution of stars as a reference. Grey dots are our 401 candidates. The magnitudes used here are the PSF magnitudes estimated from our decomposition methods based on HSC imaging (Section 2.1.2). Colored data points are targets we have observed to date. Green filled circles are those identified as quasars, two projected pairs are filled with pink color. Galaxies are shown as cyan squares. Stars are shown as red star marks. In some cases, the spectra are too noisy or too featureless to tell which class they belong to, these unclassified targets are labeled as purple cross marks.

We find that the targets from same classes seem to cluster in certain regions of color-color space. Quasars locate around the blue end of the stellar locus and mostly above it with relatively far distance. Galaxies are located at the lower right side of the stellar locus and also have relatively far distance. While stars are mostly along the stellar locus, as this curve was defined so.

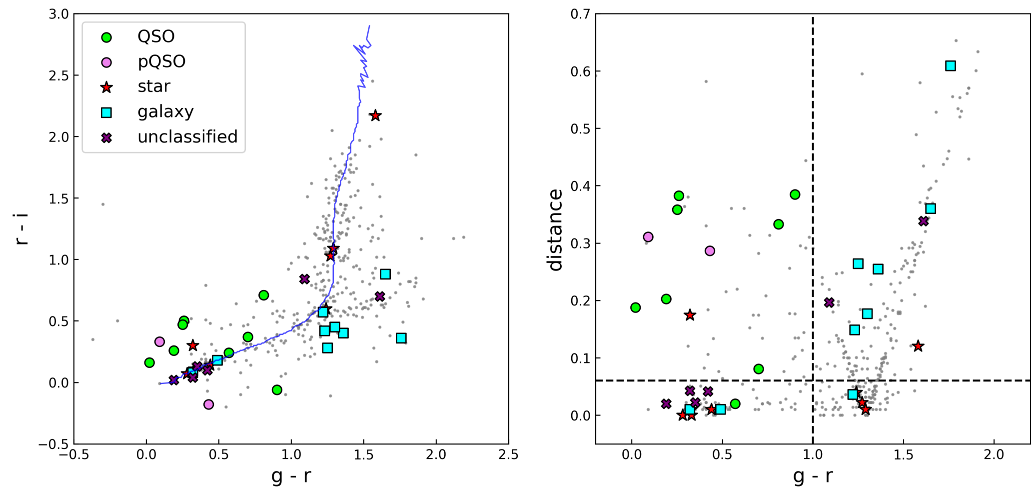


Fig. 3.4: Distribution of the companions in the color space (small grey dots). The main quasars are not shown here. Left panel: distribution around the stellar locus as indicated by the thin blue line. Green dots are secure quasars, pink dots are project quasars, red star marks are stars, cyan squares are galaxies, purple cross marks are unclassified sources. Right panel shows the distance of each targets from the stellar locus vs g-r color, dashed lines are $g - r = 1.04$ and $distance = 0.06$, see detailed discussion in the text.

Therefore, there seem to be two parameters that may matter on the class of the targets: color and distance form the stellar locus. Thus we plot these targets again in a distance-color space (Figure 3.4 right panel). This time the quasars are better separated from the other classes, basically, they are blue and far away from the stellar locus. We draw manually a vertical dashed line at $g - r = 1.0$, this was already used as the criterion of priority of our targets when doing observation (Figure 2.4). Now we add another vertical line at "distance from stellar locus=0.6", dividing the figure in to 4 regions. The left upper region is where we have a very high success rate of identifying quasars (9/10). The lower left region resides mostly blue stars, the main contamination of our observation. This is instructive for future observational plans, but may lead to a selection bias towards the blue quasars. There are quasars that are actually very close to the stellar locus. In our case, the "outlier" quasar at the lower left region is a high redshift quasar pair at $z \sim 3.16$, its host galaxy is unresolved, making the source very star-like. The lower right region is where red stars locate, we have not been successful in finding a quasar in this region. Most of the galaxies are at the upper right region, among which we have one source with moderate AGN activity but classified as galaxy according to the diagnostic diagrams.

### 3.1.4 A Trial with Support Vector Machine

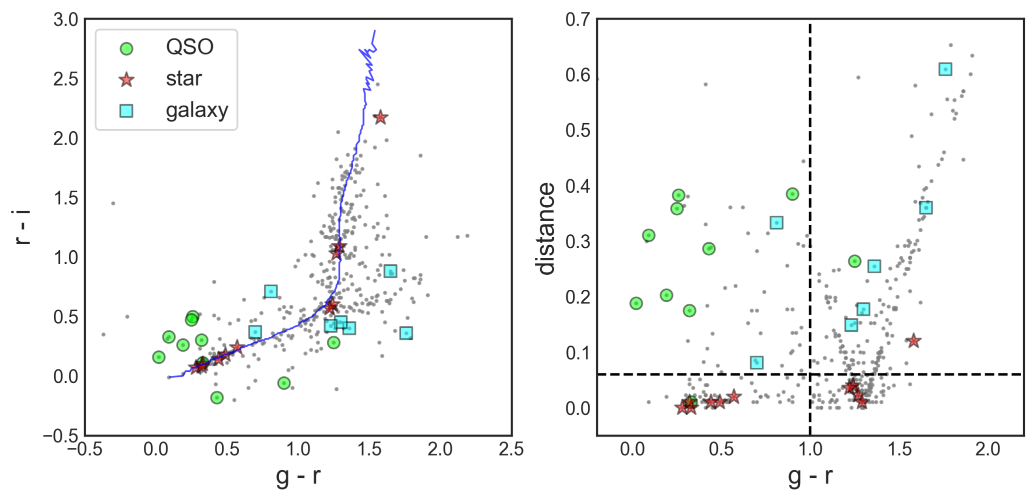


Fig. 3.5: Prediction of the types of the targets we have observed in this study using SVM. Only those with clear classification are colored. The data set and fugure configuration are the same as figure 3.4.

Considering the clustering of different types of targets in the color-color diagram, it is possible to apply machine learning strategies to guide our sample selection in the future. Support-vector machines (SVMs, [125]) are supervised learning models that can classify the data into different categories via constructing hyperplanes in a high-dimensional parameter space. The advantages of this algorithm over human eyes are that it can find out the connection of multiple dimensions, while we can only tell from no more than 3-dimensional space. The criterion we draw in figure 3.4 right panel can be seen as a 1D plane in a 2D space. With SVM, we can draw a (n-1)D plane in a nD space, and it can not only be linear, but also nonlinear.

The classifier we select is **SVC** from **sklearn.svm** package. The kernel is set to be polynomial, i.e. nonlinear. The training samples we use are randomly selected 9000 quasars, 9000 galaxies and 9000 stars from HSC catalog. We take the same number of these three categories so that the classify will no be biased to anyone of them. The parameter space includes 10 axis: five magnitudes from HSC bands, four colors generated from these magnitudes and the distance from the stellar locus. The color and magnitude seem to be duplicated information, but the algorithm of SVM is able to deliver the weights to all the parameters so that finally only those important ones work for the classifer.

As a result, we get a 85.9% success rate on predicting the types of the training data set itself. Thus a fraction of the sources are still overlapped even in the 10D parameter space. But the color clustering is real as a totally blind guess will only give a success rate of 33%. We then use this classifier to predict the types of the sources we have observed in this study with clear classification (i.e. the purple crosses in figure 3.4 left panel are not included). The results are projected to the same 2D space as figure 3.4 in figure 3.5. As we expected in the previous section, stars reside along the stellar locus, quasars locate at the blueward and galaxies reside the redward. In the distance-color diagram, the classifier also predicts a very high success rate of finding quasars (8/10) at the left upper region we draw by experience. It turns out 67.8% of the prediction match the type we classified with observation. A not very high success rate but still double that of a totally blind guess. The confusion matrix is: $\begin{bmatrix} 7 & 3 & 1 \\ 0 & 5 & 2 \\ 1 & 3 & 7 \end{bmatrix}$ following the order of: star-galaxy-quasar. Thus seven stars, five galaxies and seven quasars are correctly classified. While one quasar is wrongly classified as star, two quasars are wrongly classified as galaxies, the success rate of predicting a quasar is 70%. And one star is wrongly classified as quasar, three galaxies are wrongly classified as quasars, the precision rate of predicting a quasar is 63.6%. At this time point, it is not satisfying enough to instruct our sample selection, and our eye selection seems to be good enough. However, such machine learning strategies do help us to find some underlying relationship between the parameters, which could be useful for a large sample set. Also, here we only use the very simple model of SVM, it could be hypertuned to improve the classifier.

### 3.1.5 Color Variations of Dual Quasars

Now we would like to focus on the color of physically associated quasar pairs. This time we plot both the companions and the main sources in the same plot but remove the other classes (Figure 3.6). In the upper panel, red dots are the same data set as in Figure 3.4, black dots are the main source of these systems, i.e. the known SDSS quasars. Our 10 quasar pairs (including the SDSS pair and projected pairs) are shown with star marks, same color marks stand for the two sources in one system. Similar to stellar locus, [13] suggested that quasars at same redshift tend to have similar color based on their studies on 2625 SDSS quasars, thus form a "quasar locus" in color-redshift space. In the lower panels, we show this locus with shadowed 95% confident regions and overlaid our dual quasars. 62.5% (10/16) of them fall in the 95% region of $g-r$, 75% (12/16) fall in the 95% region of $r-i$, both significantly smaller than 95%. Therefore, dual quasars may tend to have more abnormal colors, and mostly (5 of 6 outliers in $g-r$, 4 of 4 outliers in $r-i$) being redder. We suggest the reason are the dust extinction caused by the interaction of the galaxies.

## 3.2 Details On Individual Cases

### 3.2.1 Line Fitting Procedures

Next we will provide the details of several targets, basically three types: physically associated quasar pairs (velocity offset between two SMBHs smaller than 2000 km s$^{-1}$ [126]), projected quasar pairs (velocity offset between two SMBHs larger than 2000 km s$^{-1}$) and quasar-galaxy pairs (small velocity offset but only one source possess activated SMBH). The line widths and offsets are estimated via line fitting, which is perforemed using Python scipy.optimize.curve_fit package, the basic algorithm is Least Square when no boundary is set and Trust Region Reflective when is set. In most cases, we have to set some constrains to the parameter based on the appearance of the spectrum to make the fitting stable. Here we list the models we applied to certain emission lines: For C IV $\lambda$1549, we first fit a power law in the spec-

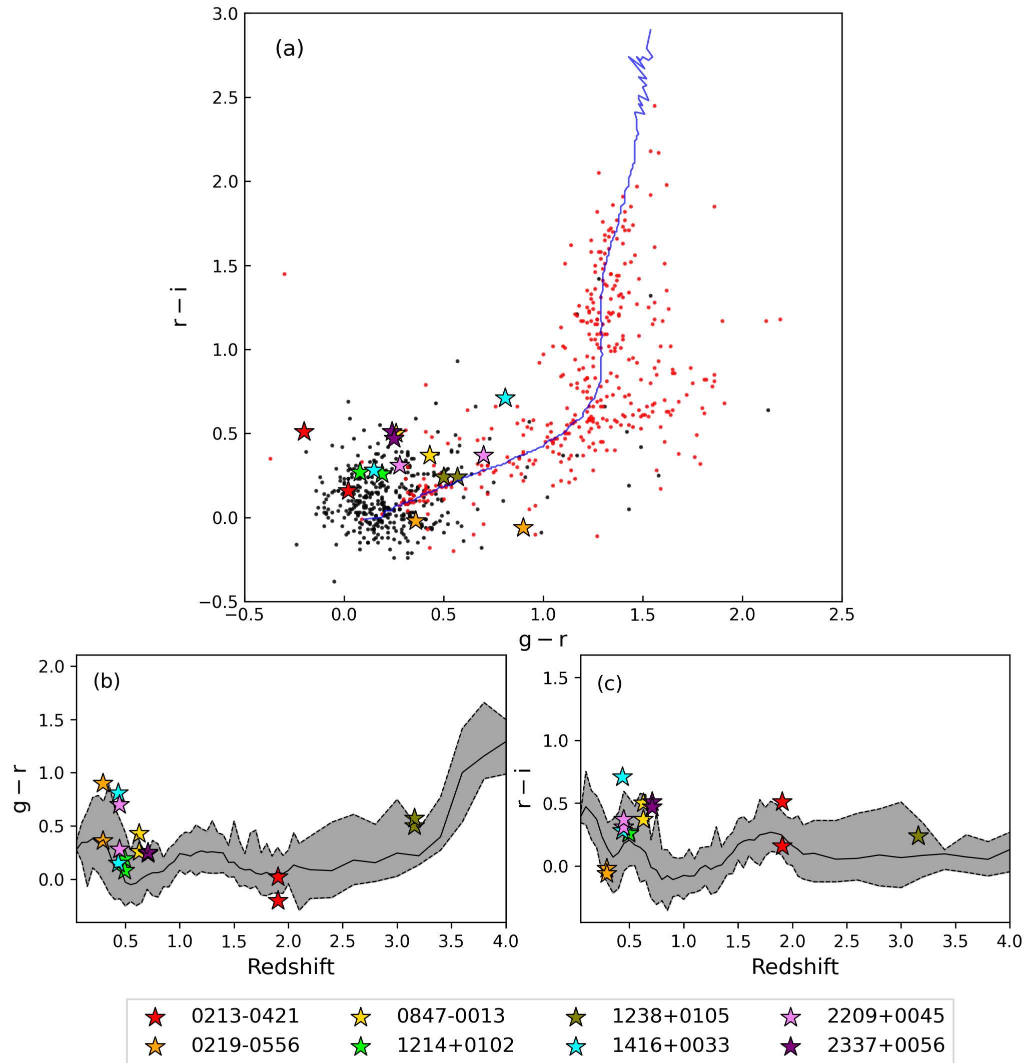


Fig. 3.6: Quasar pairs in color space, upper panel: similar to Figure 3.4 left panel. Here we plot both the quasars and their companions in this color-color space, black dots are main SDSS quasars and red dots are companions, blue line is again Covey's stellar locus. Bottom panels plot these targets in color-redshift space. According to [13], quasars at same redshift tend to have similar color, whose average is the black "quasar locus" in these two plots, grey shadows are 95% confident regions.

tral window [1445,1465] and [1700,1705] Å, to remove the continuum. We fit the emission line with either one or two Gaussian components. We mask regions that are affected by significant absorption features. In one source that has BAL features, we include an extra gaussian component to describe the absorption feature in the model fit. Similar to C IV $\lambda$1549, C III]$\lambda$1909 and Mg II $\lambda$2798 are also usually single component lines, thus fitted with a single gaussian component after subtracting the continuum in most cases. The power law continuum region for C III] $\lambda$1909 is taken from [1700,1820] and [2000,2500] Å. For Mg II $\lambda$2798, it is [2200,2700] and [2900,3090] Å. In Mg II $\lambda$2798's case, the iron emission is sometimes significant, we applied [127]'s UV iron template when necessary.

H$\beta$ and [O III]$\lambda\lambda$4959, 5007 are fitted simultaneously. The spectral windows [4435,4700] and [5100,5535] are used to fit the continuum and remove it from the spectrum prior to fitting the emission line. After subtracting the continuum, we fit the emission components together in several cases depending on our data: the basic one includes three gaussian components, corresponding to a narrow H$\beta$ component + [O III] $\lambda$4959 + [O III] $\lambda$5007. We assume the width of the narrow lines to be the same in velocity space and locked their position (i.e, the separation between [O III] $\lambda$4959 and [O III] $\lambda$5007 is locked as 48Å in the rest-frame and the separation between H$\beta$ and [O III] $\lambda$5007 is locked as 145.5Å). We also set the ratio of [O III] doublet's height to be 2.98 according to atomic physics [128]. Therefore, in this case, we only have one free positional parameter, one free width parameter and two free height parameters. When a broad component is required for H$\beta$, we add one extra gaussian component to the model, the parameters of this component is totally independent from the narrow components considering their different origin. On the other hand, it is common for [O III] doublet to have asymmetric blue wings [129], in that case, we add two gaussian components locate at the blueward of the core components, these two components themselves have same width, proportional height and locked position. Our fitting model could be the basic case or a premium course with either or both of the two snacks.

### 3.2.2 A Guidance to the Figure Format

The information of each target is collected in one figure, which is always organized in three panels (Figure 3.7 as an example):

The upper panels of Figure 3.7 show the optical imaging from Subaru HSC. The RGB colored image is generated via the standard way of HSC [130], using data of g, r and i bands. The magenta circle shows the position of SDSS fiber, the green dashed rectangular region shows the position of the slit we use for long-slit spectroscopy. The blue and red rectangular regions are the extraction apertures in 2D used to generate the individual 1D spectra. We keep the same color coding for all the sources so that source A in red is always the known SDSS quasar (usually the brighter source), and source B in blue is always companion identified in this study. For pairs at redshift < 1, we use the LENSTRONOMY tool [131] to decompose the images into point sources and host galaxies separately. This was carried out for all 5 bands, but here we only show i-band results as an example as it has the best image quality in HSC data (section 2.1.1). These series of images from left to right are the: original data, reconstructed model (point sources + host galaxies), host galaxies (data - point sources) and normalized residuals (data - model).

Middle panel (panel (b)) shows our spectrum data. The overploted 1D spectrum are extracted from the rectangular regions in the HSC images. Besides the standard flux calibration with IRAF, the HSC magnitudes used for rescaling (section 2.3.8) are plotted as star marks, red for source A, blue for source B. The position of emission lines are also labeled with dashed vertical lines with same color coding. We show a zoom in view of the reduced 2D spectrum while highlighting emission lines of interest.

Bottom panel (panel (c)) shows detailed analysis of the emission-line profiles through multi-component fits using Gaussian models. The colored curves represent different components as noted in the legend. The vertical brown dashed lines in the line fitting images label the centroid of the emission lines. The tables on the right hand side record the widths of narrow and broad lines with errors, and the offsets of the lines between two sources or between the broad and narrow components of the same line, for example, "$An\_Ab$" stands for the offset between the narrow line and the broad line of source A, "$Ab\_Bb$" stands for the offset between the broad line of source A and the same broad line of source B. The velocity is positive when the former line is redshifted relative to the later line, vise versa. All the velocities are in the units of $km/s^{-1}$

### 3.2.3 Physically-associated quasar pairs

We report on the properties of five newly-discovered dual quasars where the companion to a SDSS quasar has been identified as a physically-associated quasar through our spectroscopic program.

#### SDSS J220906.91+004543.9

Figure 3.7 shows all the necessary information of this target. As shown in panel (a) HSC image, the two sources have similar color, both of them reside

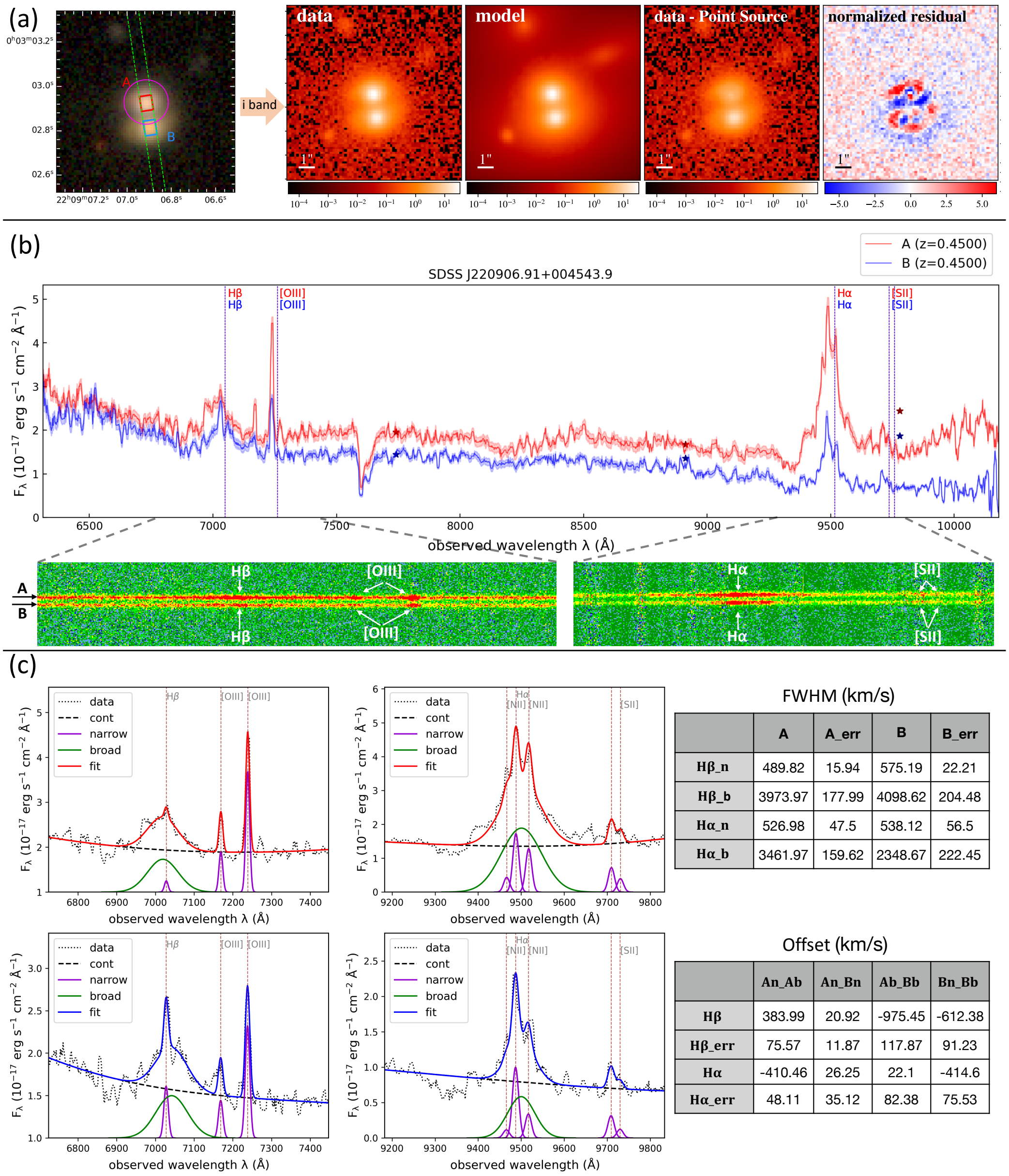


| | A | A_err | B | B_err |
|---|---|---|---|---|
| Hβ_n | 489.82 | 15.94 | 575.19 | 22.21 |
| Hβ_b | 3973.97 | 177.99 | 4098.62 | 204.48 |
| Hα_n | 526.98 | 47.5 | 538.12 | 56.5 |
| Hα_b | 3461.97 | 159.62 | 2348.67 | 222.45 |

| | An_Ab | An_Bn | Ab_Bb | Bn_Bb |
|---|---|---|---|---|
| Hβ | 383.99 | 20.92 | -975.45 | -612.38 |
| Hβ_err | 75.57 | 11.87 | 117.87 | 91.23 |
| Hα | -410.46 | 26.25 | 22.1 | -414.6 |
| Hα_err | 48.11 | 35.12 | 82.38 | 75.53 |

Fig. 3.7: A kaleidoscope of J220906.91+004543.9. Panel (a): image information of the HSC data and decomposition. Panel (b): 1D and 2D spectrum information. Panel (c): Supplementary information, the line fitting results and parameters.

in the "quasar region" of the color-color diagram (Figure 3.6). They are separated by $1.''67$, this corresponds to 9.55 kpc at this redshift. Their i band magnitudes are 19.92 and 20.25. SDSS spectrum of this source was taken from SDSS southern survey with $3''$ diameter fiber. It was classified as a broad line quasar at $z = 0.4466$.

The FOCAS spectrum covers the H$\beta$ and H$\alpha$ regions well-separated for the two sources (Figure 3.7 panel (b)). According to the fitting results (Figure 3.7 panel (c)), the FWHM of broad H$\beta$ component in source B is $4098.6 \pm 204.5$ km s$^{-1}$, that of broad $H\alpha$ is $2348.7 \pm 222.5$ km s$^{-1}$. The measurement of the narrow lines tell that in the two sources they are only offset by $\sim 20\ km\ s^{-1}$, indicating they are at a very similar redshift. Based on these evidence we classified it as a quasar pair.

As shown in Figure 3.7 panel (a), the decomposition of the i band image resolves the host galaxies of this system (methods described in section 2.1.2), as our modeling of host galaxies consider the Sérsic profile only, the non-smoothness of the residual could be a signal of asymmetry of the galaxies' morphology, possibly resulted from the on-going merger event. For J2209, the asymmetry is not very strong and the galaxies are not totally deformed yet. Thus we suggest that this is a system undergoing their first passage. Considering the small offset between the narrow lines in two sources, we further argue that our view angle towards this system should be almost perpendicular to the merging plane. On the other hand, we find the broad H$\alpha$ components in the two sources are redshifted by $\sim 400$ km s$^{-1}$ relative to the narrow components. However, the values of H$\beta$ do not totally agree with that, it is blueshifted in source A and redshifted with a larger velocity in source B. These offsets could possibly be caused by the recoil of the SMBH during the merger.

#### SDSS J233713.66+005610.8

The SDSS legacy survey classified this target as a broad line quasar at $z = 0.7080$. The SDSS fiber diameter is 3" and centered on the southern source as shown in Figure 3.8 panel (a) by the red circle. The optical color of the two sources are very similar and both of them are located in the typical quasar region of the color-color diagram (Figure 3.6).

The GMOS spectrum of this target was taken with R831+RG610 grism so that H$\beta$ region is captured at the center of the spectrum (Figure 3.8 panel (b)). The 2D spectra of the two individual objects is well-separated and we can clearly see the [O III] and H$\beta$ features in both spectrum. We measured a FWHM of $2002.5 \pm 27.5$ km s$^{-1}$ for H $H\beta$ in source B and an offset of $300.8 \pm 16.5$ km s$^{-1}$ between two sources. Thus we classify this target as a

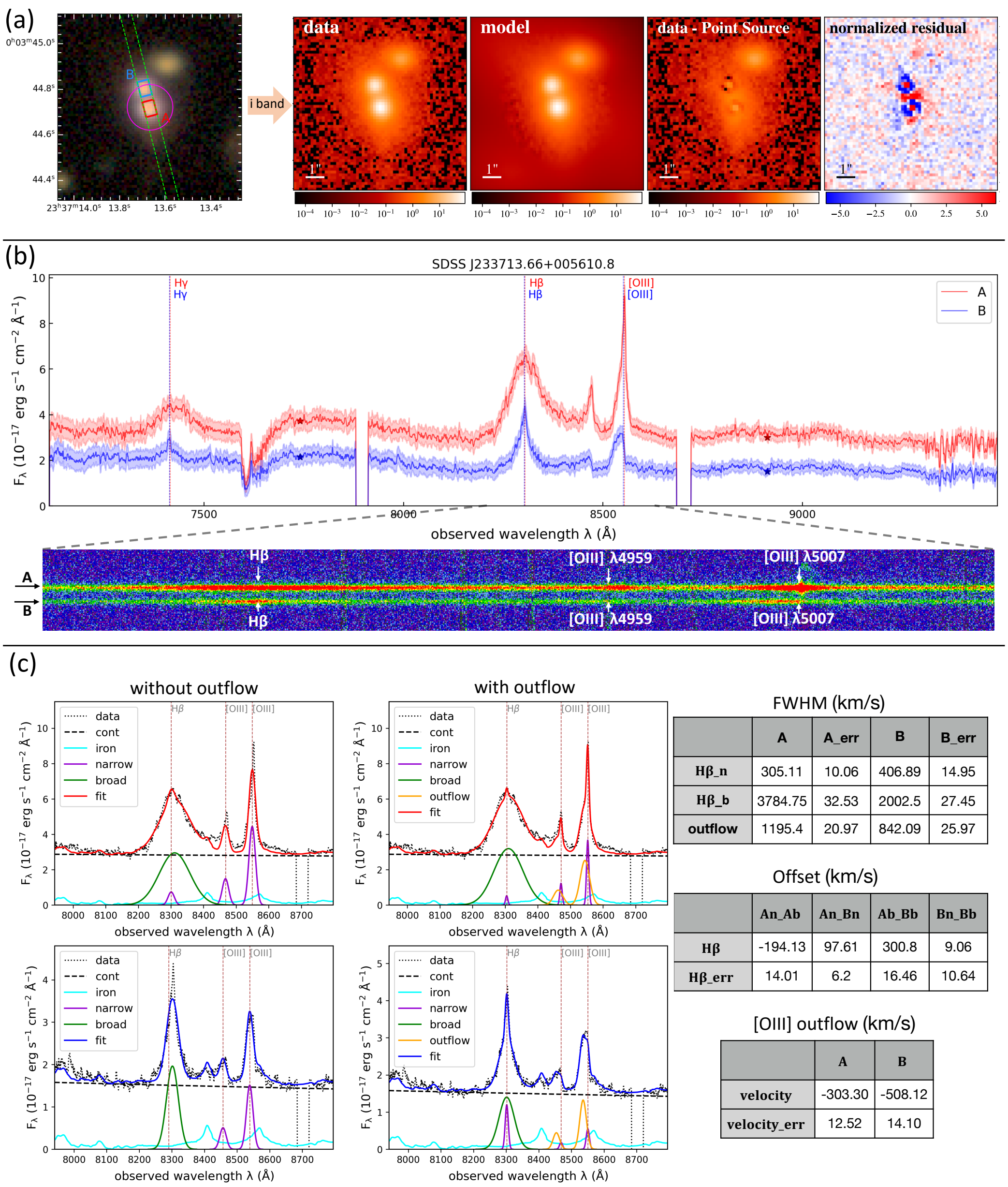


FWHM (km/s)

| | A | A_err | B | B_err |
|---|---|---|---|---|
| Hβ_n | 305.11 | 10.06 | 406.89 | 14.95 |
| Hβ_b | 3784.75 | 32.53 | 2002.5 | 27.45 |
| outflow | 1195.4 | 20.97 | 842.09 | 25.97 |

Offset (km/s)

| | An_Ab | An_Bn | Ab_Bb | Bn_Bb |
|---|---|---|---|---|
| Hβ | -194.13 | 97.61 | 300.8 | 9.06 |
| Hβ_err | 14.01 | 6.2 | 16.46 | 10.64 |

[OIII] outflow (km/s)

| | A | B |
|---|---|---|
| velocity | -303.30 | -508.12 |
| velocity_err | 12.52 | 14.10 |

Fig. 3.8: A kaleidoscope of J233713.66+005610.8. In the line fitting panels of this target, we applied both iron emission and outflow components, which are drawn as cyan curves and orange gaussian shapes. The final best fitting spectrum included these two extra components.

dual quasar system.

Notably, the [O III] doublet seem to have blue wings in both of the sources. To prove this, we fit the lines with two different models (Figure 3.8 panel (c)). In the left column, no outflow components are used, thus each [O III] line is only modelled with one single gaussian curve. This leaves a significant residual (a sharp peak not fitted) on [O III] in source A and $H\beta$ in source B. One may argue about the result of the fitting in source B for a lack of a narrow component for $H\beta$. The discrepancy is that, as we have locked the widths of the narrow lines, if we would like to explain the [O III] doublet with that widths, then we have to use the same parameter for the H$\beta$, which does not work for the sharp peak there. Therefore, the width of the core [O III] doublet emissions should be narrower. We thus apply extra outflow components for the [O III] doublet in both sources (orange curves in the right line fitting plots of Figure 3.8 panel (c)). This improves the result a lot and now we see the sharp peaks in both sources are well explained.

Our decomposition do not really resolve the morphology of their host galaxies. However, we can tell from the "data - Point Source" panel and normalized residual that they are more extended than simply two point sources: the centers are underfitted (red in residual) and outer regions are overfitted (blue in residual)). The HSC image also shows a third source at the north of the pair, but there are no obvious tidal features either from the quasar's host galaxies or the third source, and it is well-modeled by a Sérsic profile thus not heavily disturbed. So we suggest this should be a foreground galaxy.

Considering the lens hypothesis for this system, we argue that the layout of the three sources (two point sources and the extra galaxy) is not akin to a typical lens system in HSC (e.g. [132], [133]). On the other hand, source B tends to have relatively stronger narrow $H\beta$ comparing to its broad component than source A, which should be similar if this is a lens system.

#### SDSS J123821.66+010518.6

The SDSS BOSS program reports this target as a broad line quasar at $z = 3.1327$. The fiber diameter is 2". This is the highest redshift pair we have confirmed so far, both are very red sources in HSC imaging (Figure 3.9 panel (a)) and close to the color locus (Figure 3.6). The primary source is two magnitudes brighter than the secondary. The host galaxies are unresolved in this system according to our decomposition results.

The GMOS spectrum of this target was taken with B600+CG455 grism. Ly$\alpha$ and C IV$\lambda$1549 were covered (Figure 3.9 (b)). The redshift measurement of source A is based on template matching (figure 3.9 (c) right figure). However, Ly$\alpha$ and C IV$\lambda$1549 are affected by strong absorption, causing their

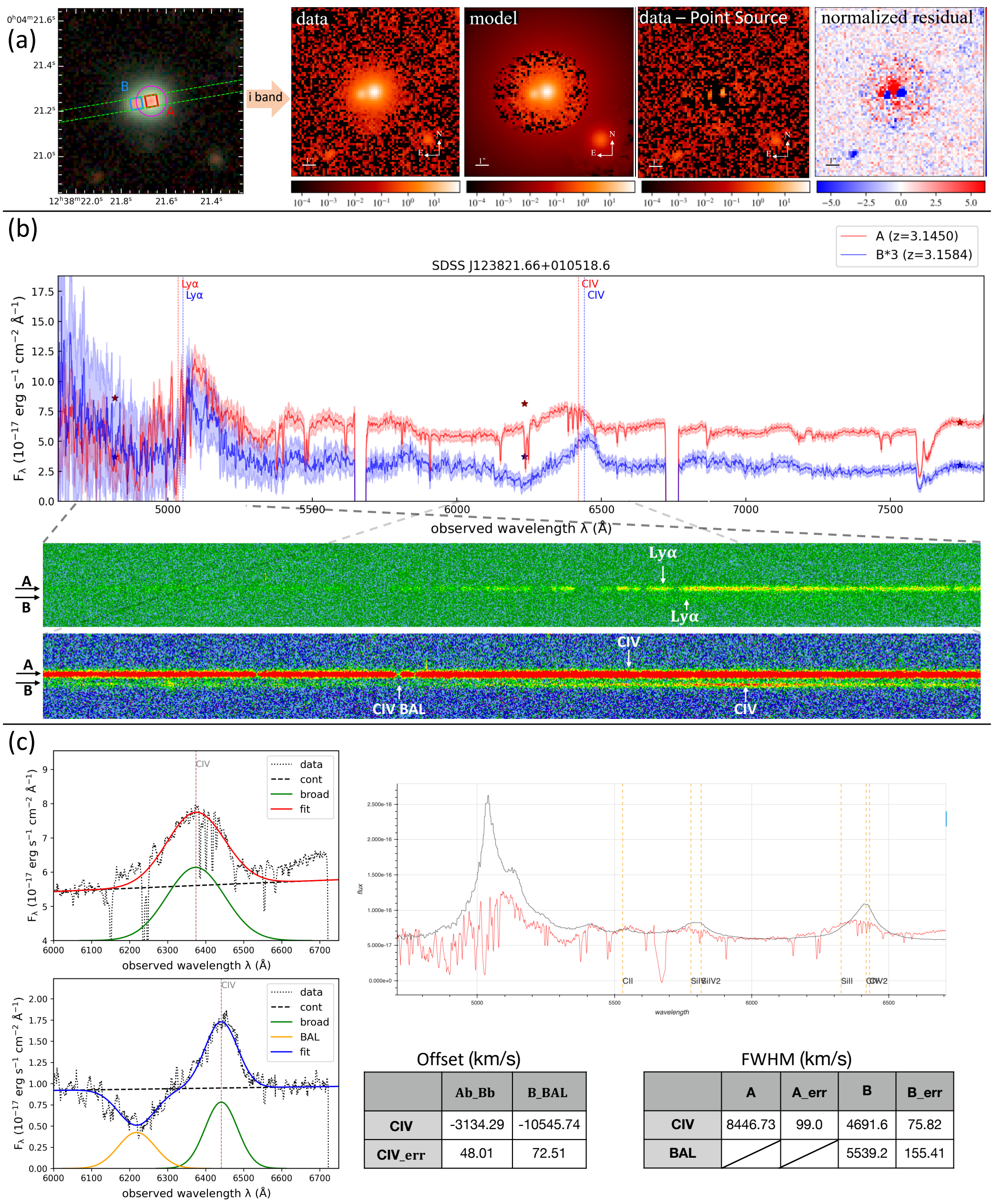


| | Ab_Bb | B_BAL |
|---|---|---|
| CIV | -3134.29 | -10545.74 |
| CIV_err | 48.01 | 72.51 |

| | A | A_err | B | B_err |
|---|---|---|---|---|
| CIV | 8446.73 | 99.0 | 4691.6 | 75.82 |
| BAL | | | 5539.2 | 155.41 |

Fig. 3.9: A kaleidoscope of J123821.66+010518.6. Panel (a): image information of the HSC data and decomposition. Panel (b): 1D and 2D spectrum information. Panel (c): Supplementary information, the line fitting results and parameters.

centroids to be shifted. In the template matching figure, the black curve is the SDSS quasar template, red curve is our data. We shifted the template to $z = 3.145$ so that the Ly$\alpha$ feature and the continuum match our data. Some absorption lines are labeled with orange vertical dashed lines. While for source B, the results from line fitting and template matching agree with each other, indicating a redshift around 3.1584. Giving this small difference between the redshift, we classify this as a physically associated quasar pair.

Further more, we carry out a line fitting routine on C IV$\lambda$1549 of the two sources. We find that the companion appears to have a typical 'P Cygni' profile while the primary source does not. We fit the profile with two gaussian functions (Figure 3.9 panel (c) left figures) to model the BAL component that is blueshifted from the emission line by $10545.7 \pm 72.5$ km s$^{-1}$ with a FWHM of $5539.2 \pm 155.4$ km s$^{-1}$, comparing to $4691.6 \pm 75.8$ km s$^{-1}$ of the emission component. According to [134], a quasar with contiguous absorption spread on more than 2000 km s$^{-1}$ and with a blueward velocity of at least 5000 km s$^{-1}$ can be considered as a BAL quasar. Therefore, we further classify this as a BAL quasar. The difference of width of the absorption and emission lines can be explained geometrically [135]. The width of the emission line will be equal to the width of absorption line if the outflow is spherically symmetric. In fact, many BAL quasars have stronger absorption lines than emission lines, suggesting a non-spherical symmetric geometry of the outflow, as seen in the companion to SDSS J123821.66+010518.6.

### SDSS J021930.51-055643.0

The SDSS BOSS program classified this target as a broad line quasar at $z = 0.2917$. The fiber diameter is $2''$ and centered on the northern source as shown in Figure 3.10 panel (a) colored image. The companion is relatively diffuse and deformed. Our decomposition model does not reconstruct this system into a good result, indicating the anomalous morphology.

The FOCAS spectrum of this target was taken with VPH850+O58. H$\alpha$ regions are captured but unfortunately, H$\beta$ just falls out of the coverage (Figure 3.10 panel (b)). The spectrum of the companion is relatively faint, the flux of the continuum is around one thirds of that of the main quasar, the photometry magnitude is 1.2 magnitude fainter on average of five bands. Thankful to the weather condition, they are not blended. It is ambiguous whether the companion has a broad H$\alpha$ component or not. We tried to fit the emission lines with two models. The left column includes models with broad H$\alpha$ and right column without (Figure 3.10 panel (c)). Only three panels are shown since the main quasar clearly has broad H$\alpha$. For the companion, both models seem to equally fit the data, thus it is hard to tell which one is better

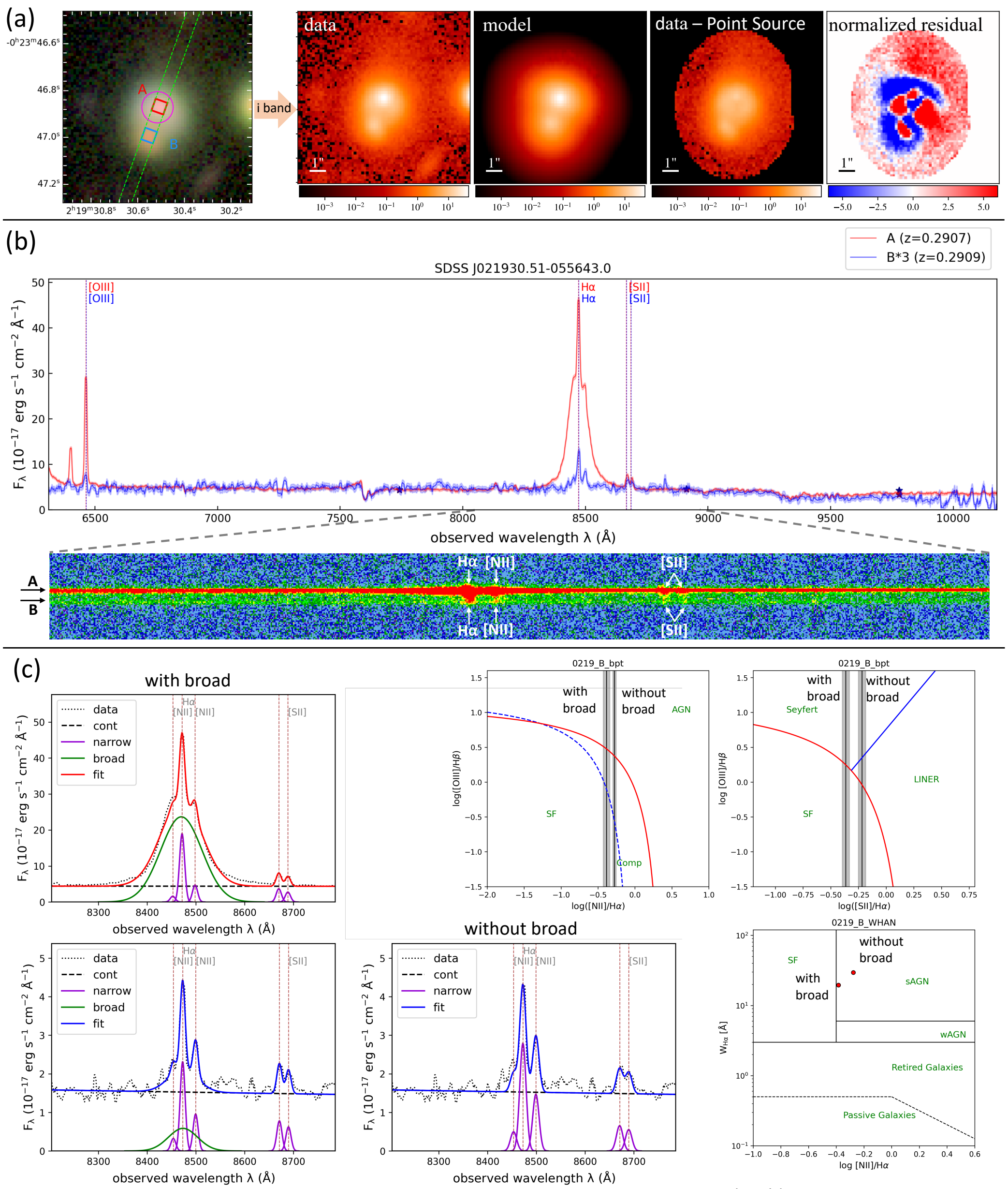


| FWHM (km/s) | | | | |
|---|---|---|---|---|
| | A | A_err | B | B_err |
| Hα_n | 433.95 | 15.83 | 426.9 | 19.31 |
| Hα_b | 3545.47 | 30.96 | 2501.33 | 194.94 |

| Offset (km/s) | | | | |
|---|---|---|---|---|
| | An_Ab | An_Bn | Ab_Bb | Bn_Bb |
| off | 55.02 | -41.95 | -121.42 | -24.46 |
| err | 13.56 | 9.01 | 76.43 | 75.76 |

Fig. 3.10: A kaleidoscope of J021930.51-055643.0. Panel (a): image information of the HSC data and decomposition. Panel (b): 1D and 2D spectrum information. Panel (c): Supplementary information, the line fitting results and parameters.

than another. Therefore, we consider both cases in the following discussion. We first consider using the conventional BPT diagnostic diagram (Baldwin, Phillips & Terlevich, [123, 124]). Since we only have the H$\alpha$ region covered, the [O III]/$H\beta$ is unknown. We plot them as vertical lines with shadows indicating the error (Figure 3.10 panel(c) right figures). The model with broad component gives a lower [N II]/H$\alpha$ ratio, corresponding to the left line, while the model without a broad component corresponds to the right line. We found in both diagrams, the span ia over all the categories. Therefore, it is still hard to determine the origin of the source. Fortunately, [136] provided a new tool known as the "WHAN diagram" using the equivalent width of H$\alpha$, $W_{H\alpha}$ versus [N II]/$H\alpha$ to classify galaxies, in which no information about $H\beta$ is required. This diagram is shown at the bottom right of Figure 3.10 panel (c). There are five classes according to their diagnostics: Pure star forming galaxies; Strong AGN (sAGN in the figure); Weak AGN (wAGN in the figure); Retired Galaxies (fake AGN); Passive galaxies (line-less galaxies). Two red dots stand for our data estimated from two different models. The error is comparable to the size of the data points, thus not plotted. We found both of them locate in the strong AGN region, the result from model with broad component is closer to star forming region, but in that case, we have the broad component as another evidence. The FWHM of which turns out to be $2501.3 \pm 194.9$ km s$^{-1}$. The position of the H$\alpha$ is almost the same in two sources, shifted by only $\sim 100$ km s$^{-1}$. Therefore, we classified this target as a likely dual AGN system, with its companion a Seyfert-like source.

On the other hand, the 2D spectrum in Figure 3.10 panel (b) shows that the H$\alpha$ regions in two sources seem to be merged. The H$\alpha$ emission in source A is more extended at the companion's side than the other side. Recall the deformed morphology of the two galaxies, we suggest this system to be undergoing a stage of second passage or later, when they have been bound to each other. The distance of these two sources are projected to 7.74 kpc at this redshift.

**SDSS J021322.99-042134.3**

This target is a special case, both sources have SDSS spectrum and are classified as broad line quasars, so it is not in our observation list, we include it here because it matches our selection criterion. According to SDSS, the left source (source A) is at redshift 1.9053 and the right source (source B) is at redshift 3.5461. However, when we overplot the spectrum, we found the redshift of source B was wrong and they should be at a similar redshift (Figure 3.12 panel (b)). This target was also previously reported by [137], in which they classified it as a projected quasar pair with redshift 1.99 &

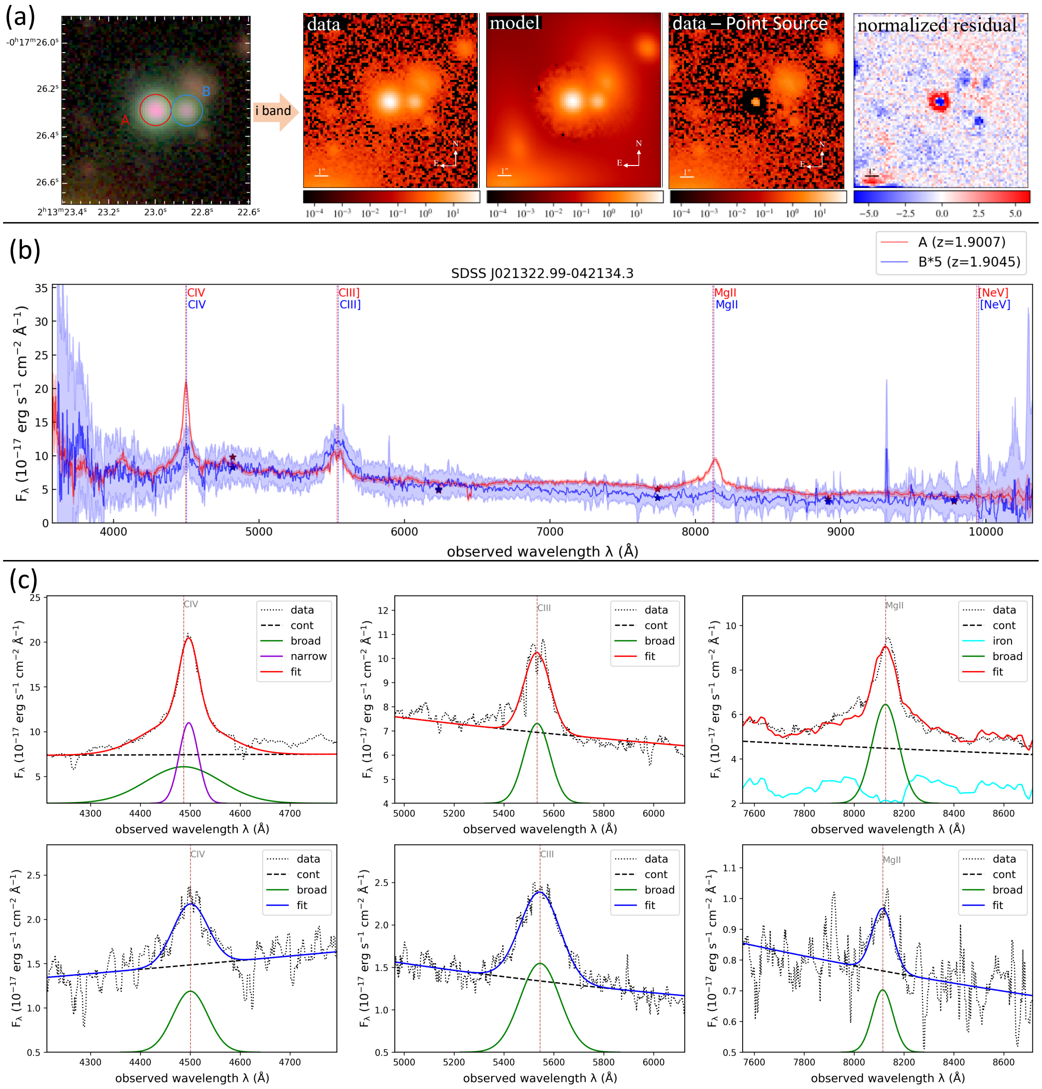


FWHM (km/s)

| | A | A_err | B | B_err |
|---|---|---|---|---|
| CIV_n | 3005.54 | 69.07 | | |
| CIV_b | 11784.79 | 317.48 | 5490.06 | 247.53 |

FWHM (km/s)

| | A | A_err | B | B_err |
|---|---|---|---|---|
| CIII | 6703.07 | 122.59 | 10204.05 | 124.41 |
| MgII | 4670.36 | 52.98 | 3630.58 | 219.87 |

Offset (km/s)

| | An_Ab_ civ | Ab_Bb_ civ | Ab_Bb_ ciii | Ab_Bb_ mgii |
|---|---|---|---|---|
| off | 683.18 | -903.69 | -644.54 | 415.81 |
| err | 89.55 | 136.15 | 75.66 | 93.86 |

Fig. 3.11: A kaleidoscope of J021322.99-042134.3. Panel (a): image information of the HSC data and decomposition. Panel (b): 1D spectrum. Panel (c): Supplementary information, the line fitting results and parameters.

0.99 (see their figure 1 panel 2) according to their Subaru observation. The discrepancty, again, appears on source B. In eBOSS spectrum, C IV line of the companion appears at 4500 Åwhere there is nothing in [137]'s result. We think of two possible reasons, the separation of two sources are 1".93, almost the same as the diameter of the eBOSS fiber, the seeing condition for source A was 1.71" and 2.03" for source B. so it is possible that the eBOSS spectrum is contaminated by the main quasar, but in this case, the line ratio of two sources are expected to be the same, while our fitting results don't support this, especially noting that there appears to be a narrow C IV component in source A, while only broad C IV in source B (Figure 3.12 panel (c)). Otherwise, it could be caused by the intrinsic variability of the source. Note there seem to be some narrow emission lines between 9000 Å and 10000 Å of the companion's spectrum. They turn out to be the residual of sky spectrum that are not well subtracted. Ignoring that, the three broad lines line up well at this given redshift. Their FWHM are $5490.1 \pm 247.5$ km s$^{-1}$ for C IV$\lambda$1549, $10204.1 \pm 124.4$ km s$^{-1}$ for C III]$\lambda$1909 and $3630.6 \pm 219.9$ km s$^{-1}$ for Mg II$\lambda$2798. Therefore, we classify this target as a dual quasar system here. However, further observation is still required to examine the classification.

### 3.2.4 Projected quasar pairs

The two sources of a projected quasar pair are offset by over 2000km s$^{-1}$ by definition [126]. With that offset, the sources are thought to be not physically-associated, but projected to that close angular separation on the image map. These targets are the by-products of this thesis. However, we can still get useful information from such systems. For example, we can study the foreground quasar's host galaxy using absorption lines apparent in the spectrum of the background quasar, and statistical study of such systems may help us to estimate the amount of absorbing gas in quasar hosts.

#### SDSS J021352.67-021129.4

SDSS BOSS program reports this target as a broad line quasar at $z = 2.7794$, both of the sources are very blue, near to the stellar locus in the quasar region (figure 3.6). The host galaxies are not resolved or even detected at this high redshift. Two PSFs are enough to model the image (Figure 3.12 panel (a)).

The FOCAS spectrum was taken using 300B+Y47 covering C IV$\lambda$1549 and C III]$\lambda$1909. Unfortunately, the observation condition was optimal since seeing was around 2" and the target was only 20° from the moon. This resulted in a very noisy profile and cut off at the blue end (Figure 3.12 panel

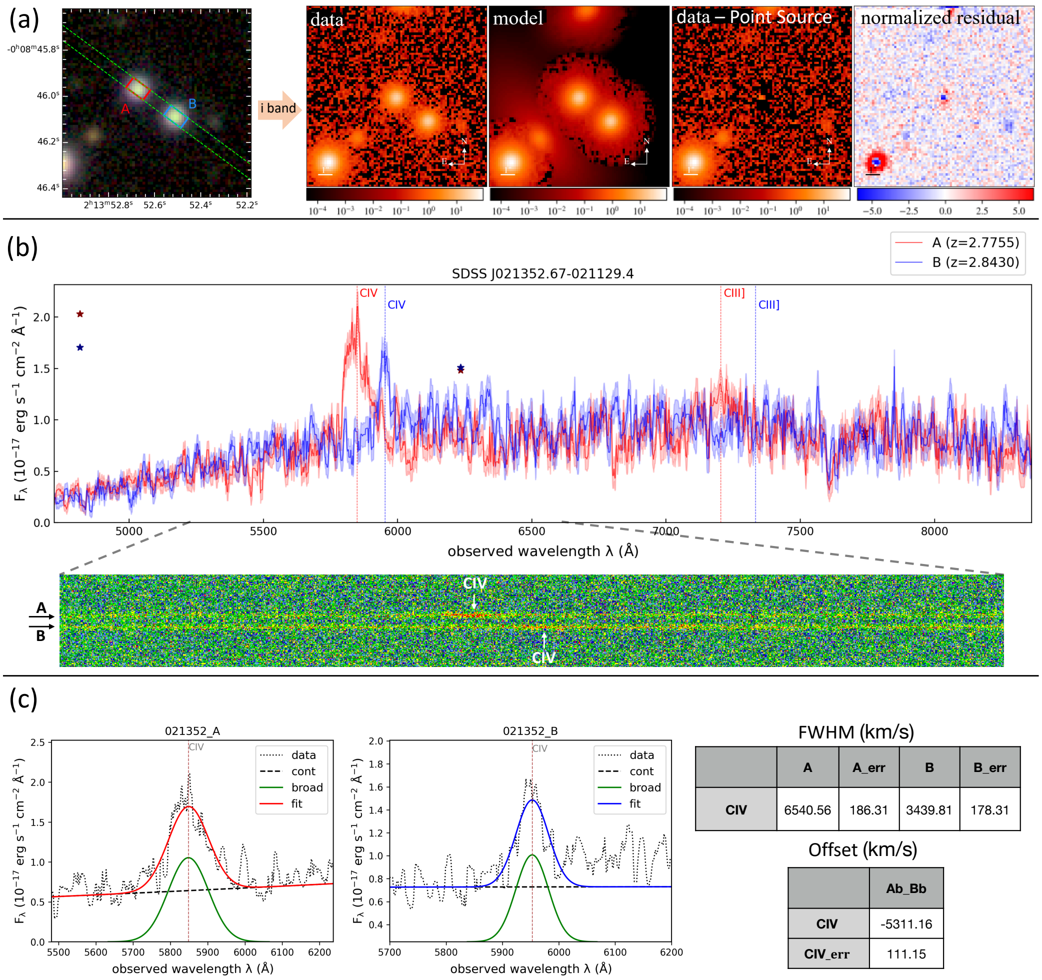


Fig. 3.12: A kaleidoscope of J021352.67-021129.4. Panel (a): image information of the HSC data and decomposition. Panel (b): 1D and 2D spectrum information. Panel (c): Supplementary information, the line fitting results and parameters.

(b)). The redshift of source A is solidly determined as Ly$\alpha$, C IV$\lambda$1549 and C III]$\lambda$1909 as observed by SDSS. Here, we find that source B is ambiguous. We are not very confident to say the peak emission in the companion is C IV, because there is no obvious C III]$\lambda$1909 feature at the corresponding position. We tried to fit the line with one gaussian function (Figure 3.12 panel (c)). It has a velocity width (FWHM) of $3439.8 \pm 178.3$ km s$^{-1}$. If we consider the line to be C IV$\lambda$1549, then it is shifted by $5311.2 \pm 111.2$ km s$^{-1}$ relative to source A. Therefore, we classify it as a projected quasar pair here.

#### SDSS J225147.82+001640.5

The SDSS reports this source as a broad line quasar at $z = 0.4096$. According to the HSC image, the main quasar is hosted by a barred spiral galaxy, it was well resolved after we subract the point sources (Figure 3.13 panel (a)) data - point source).

The FOCAS spectrum of this target was taken using VPH850+O58 covering the H$\alpha$ and H$\beta$ regions of the main quasar. However, we did not find similar features at similar positions in source B. Instead, they appear at different wavelengths (Figure 3.13 panel (b)). We find the H$\beta$ at 7670.1 Å and [O III] at 7899.7 Å. This gives a redshift of 0.5778. We see that part of the H$\beta$ emission line profile is affected by the 7600 Å sky absorption. We tried to reconstruct the profile in line fitting (Figure 3.13 panel (c)). The bottom left figure was a trial with broad H$\beta$ component that matches the profile of H$\beta$ emission well. Then we tried to fit the profile with narrow components only. We find that narrow H$\beta$ only could not fully represent the profile. This indicates the necessity of the broad component in this source. The velocity width (FWHM) is $3407.7 \pm 308.0$ km s$^{-1}$. Therefore, we classify this target as a projected quasar pair. The H$\alpha$ line of the companion should be located at around 10250 Å, buried in the noise of the red end of our spectrum.

### 3.2.5 Quasar-galaxy pairs

In two cases, we found the companion to be a galaxy at the same redshift as the quasar.

#### SDSS J022105.64-044101.5

SDSS BOSS program reports the left source shown in Figure 3.14 panel (a) as a broad line quasar at $z = 0.1986$. The fiber diameter is $2''$. According to the HSC image, the sources have very similar colors located at the lower right side of the stellar locus (figure 3.6), a relatively sparse region for quasars.

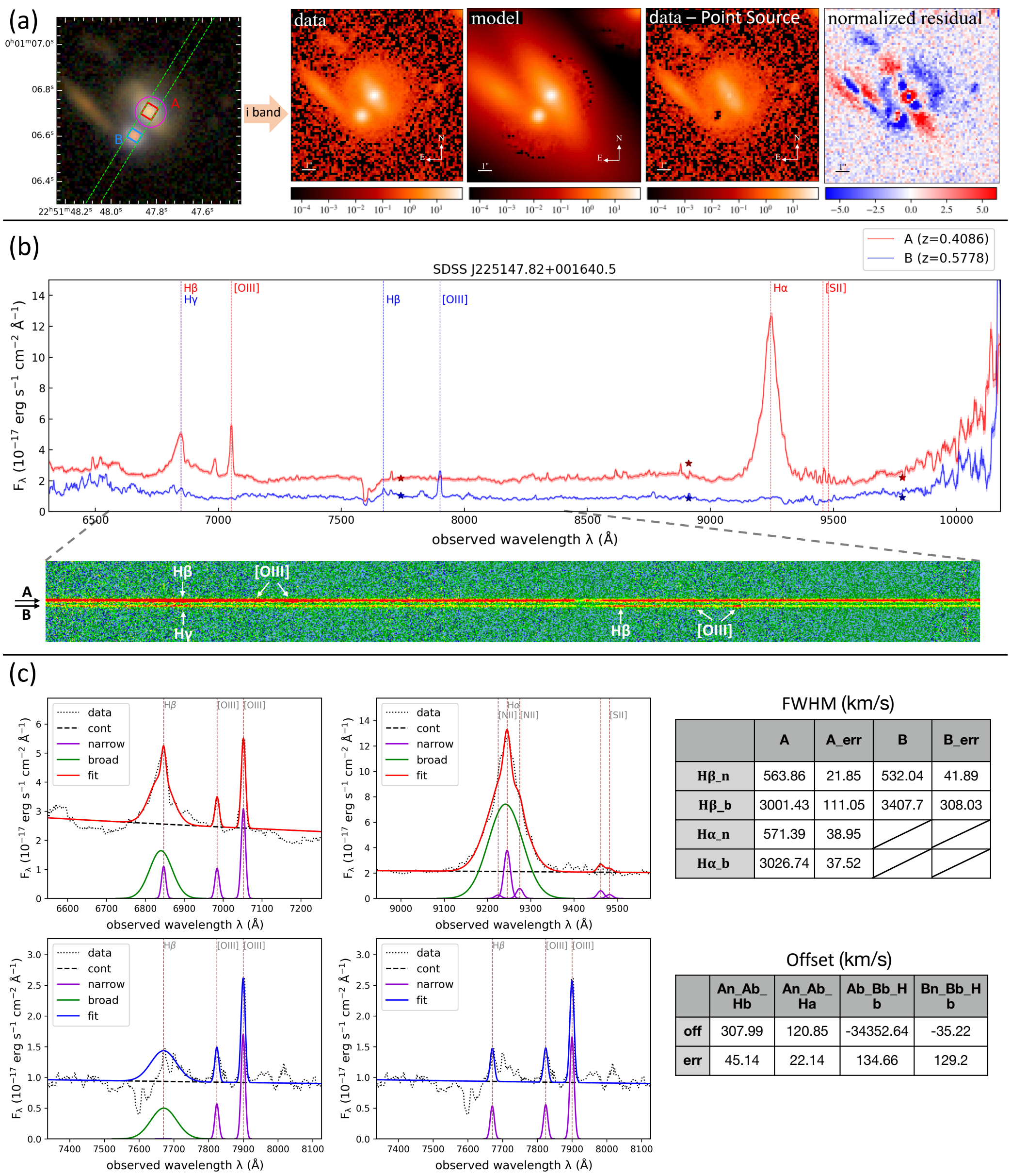


FWHM (km/s)

| | A | A_err | B | B_err |
|---|---|---|---|---|
| Hβ_n | 563.86 | 21.85 | 532.04 | 41.89 |
| Hβ_b | 3001.43 | 111.05 | 3407.7 | 308.03 |
| Hα_n | 571.39 | 38.95 | | |
| Hα_b | 3026.74 | 37.52 | | |

Offset (km/s)

| | An_Ab_Hb | An_Ab_Ha | Ab_Bb_Hb | Bn_Bb_Hb |
|---|---|---|---|---|
| off | 307.99 | 120.85 | -34352.64 | -35.22 |
| err | 45.14 | 22.14 | 134.66 | 129.2 |

Fig. 3.13: A kaleidoscope of J225147.82+001640.5. Panel (a): image information of the HSC data and decomposition. Panel (b): 1D and 2D spectrum information. Panel (c): Supplementary information, the line fitting results and parameters.

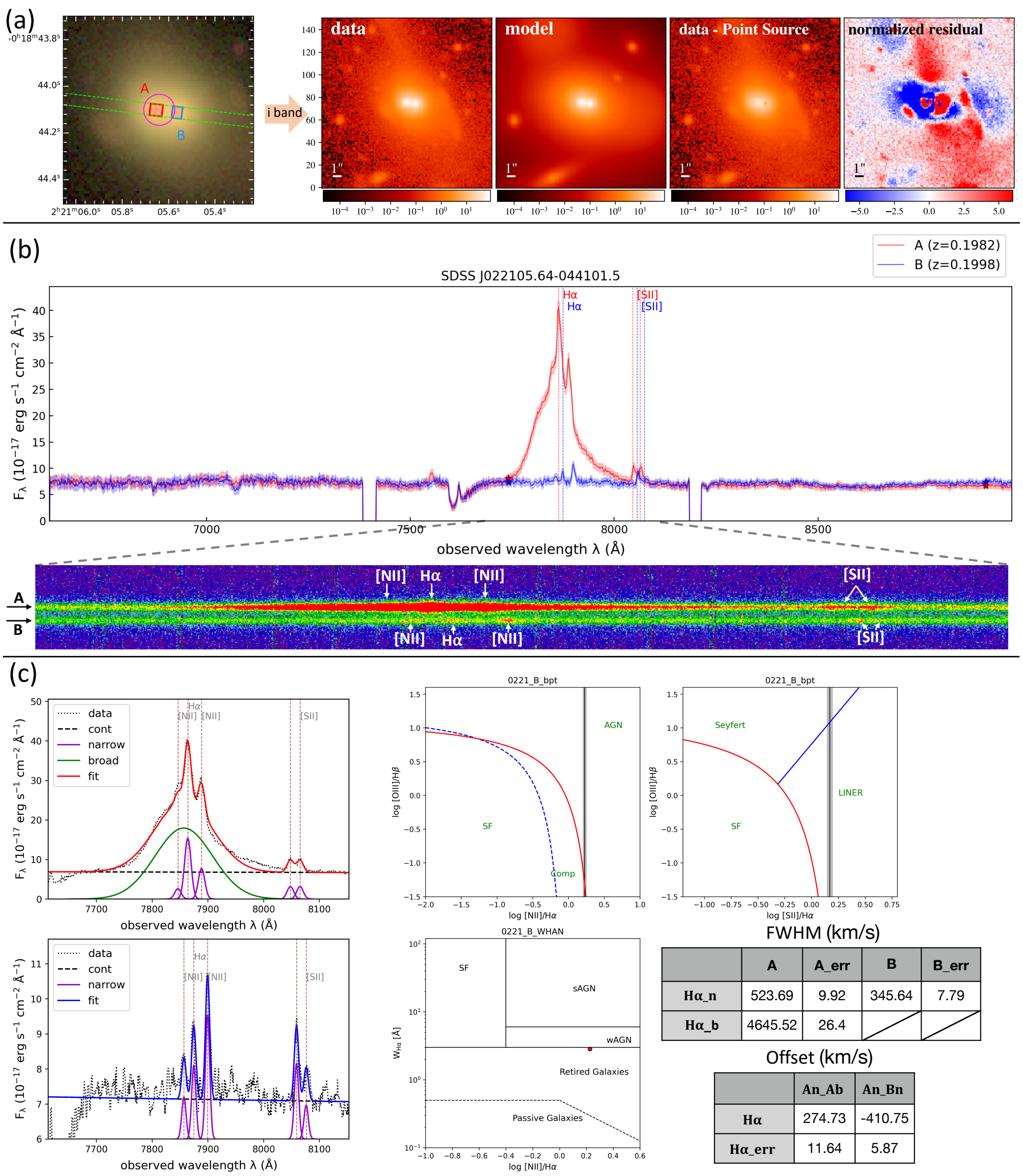


FWHM (km/s)

| | A | A_err | B | B_err |
|---|---|---|---|---|
| Hα_n | 523.69 | 9.92 | 345.64 | 7.79 |
| Hα_b | 4645.52 | 26.4 | | |

Offset (km/s)

| | An_Ab | An_Bn |
|---|---|---|
| Hα | 274.73 | -410.75 |
| Hα_err | 11.64 | 5.87 |

Fig. 3.14: A kaleidoscope of J022105.64-044101.5. Panel (a): image information of the HSC data and decomposition. Panel (b): 1D and 2D spectrum information. Panel (c): Supplementary information, the line fitting results and parameters.

The GMOS spectrum of this target was taken with R831+OG515 grism. $H\alpha$ is observed at the center of the spectrum. The 2D traces are well separated (Figure 3.14 panel (b)). We see moderate $H\alpha$ emission in the spectrum of source B. However, no broad component is required in the fitting (panel (c) left bottom figure). Similar to J0219, we also consider the emission-line ratios using the BPT and WHAN diagrams. Again, due to the lack of the information regarding [O III] and $H\beta$, we can only plot one axis on the BPT. Here, the situation is clearer for this target. Our data basically locate at the AGN and LINER region. Therefore, our first conclusion was a LINEAR type AGN. However, as mentioned by [136], the LINER region of BPT diagrams actually consists of two distinct classes: weakly active galactic nucleus (wAGNs) and retired galaxies. The later is also referred as "fake AGN" by them because the ionization photons are thought to be supplied by hot evolved low-mass stars instead of AGN. One purpose of the WHAN diagram is to distinguish these two classes. Notice that source B has a very high [N II]/H$\alpha$ ratio, up to 1.686, thus place it at the right side of the diagram. The continuum level of this source is around $7.134\times10^{-17}$ erg s$^{-1}$ cm$^{-2}$Å$^{-1}$, comparing to a flux of $20.275\times10^{-17}$ erg s$^{-1}$ cm$^{-2}$Å$^{-1}$ of H$\alpha$. This gives an equivalent width of 2.842 Å, very close to the 3 Å criterion suggested by [136] to distinguish wAGN and RGs. Our data point almost fall on the borderline of these two classes (Figure 3.14 panel (c) middle bottom figure). Of course, this diagnostic is not a dichotomy, but a continuous evolution from one to another. At the $W_{H\alpha}$ borderline, the AGN contributes between $\sim 1/3$ and 2/3 of the ionizing power and decreases as $W_{H\alpha}$ decreases. In our case, this fraction is not negligible. We argue that there is AGN contribution to some level on the lines, but it could come from the main quasar, thus the AGN source could even be weaker in the companion. According to the diagnostic diagram, we classify this as a galaxy. We do not use the word "retired" here, because this is rather a "new employee" source that is expected to have stronger and stronger emission in the future than a quenching system according to the merger triggering accretion hypothesis [52].

Back to panel (a), the two point sources are very close to each other, separated by only $1''.23$ according to our decomposition algorithm. This projects to 4.04 kpc at redshift 0.199. Our model only applied one Sérsic profile to describe the host galaxy, which has its major axis along the horizontal direction. From the normalized residual, we find another host galaxy component is possibly along the vertical direction (the underfitting red residuals). Therefore, we suggest this is a system with a large merging angle and just undergoing their first passage so that their host galaxies have not merged into one yet and one of the SMBH as not been strongly activated yet.

**SDSS J231152.90-001335.0**

The SDSS reports the source (figure 3.15 panel (a)) as a broad line quasar at $z = 0.3473$. The spiral arms of its host galaxy are resolved by HSC imaging. The fainter red companion resides at the southeast of the main source with an angular separation of $1.''75$. The PSF magnitudes of the main source are between 18 and 19 over all five bands, while the companion is very faint in the g band, down to 22.82 and roughly 20 to 21 magnitudes in other four bands. The continuum level of the main source is about seven times that of the companion. The spectrum of source B is relatively noisy (figure 3.15 panel (b)).

The redshift of the companion is supported by both the absorption lines and the H$\alpha$ line. We matched the H$\beta$, Mg and Na absorption features in the spectrum to a passive galaxy template shifted to $z = 0.345$, i.e. the same redshift as the main source (figure 3.15 panel (c) upper figure). At the corresponding position, we find the bump that is expected to be H$\alpha$ and tried to fit it with a broad component (figure 3.15 panel (c) lower figures). Although we matched the peak position in two sources, the other components in the companion's spectrum are not quite convincing. It is hard to say whether a broad component is really required there. If we believe the sharp peak there is H$\alpha$, then the velocity offset between the two sources is $417.68 \pm 22.65$ km s$^{-1}$. Our classification here is mainly based on the absorption lines, which leads to a result of a passive galaxy.

Back to figure 3.15 panel (a), considering the morphology of the host galaxy of the main quasar, although our decomposition model does not do a good work to reconstruct the features of the galaxy, the normalized residual helps to view that. It appears to be a SBb to SBc type galaxy according to the Hubble class. The south arm is slightly deformed while the north arm almost keeps the shape. Getting all these evidence together, we suggest it to be a minor merger system so that the primary galaxy is not heavily deformed. On the other hand, the primary galaxy should be gas rich and the SMBH is activated, while the secondary galaxy is a gas poor passive galaxy, the SMBH is not activated.

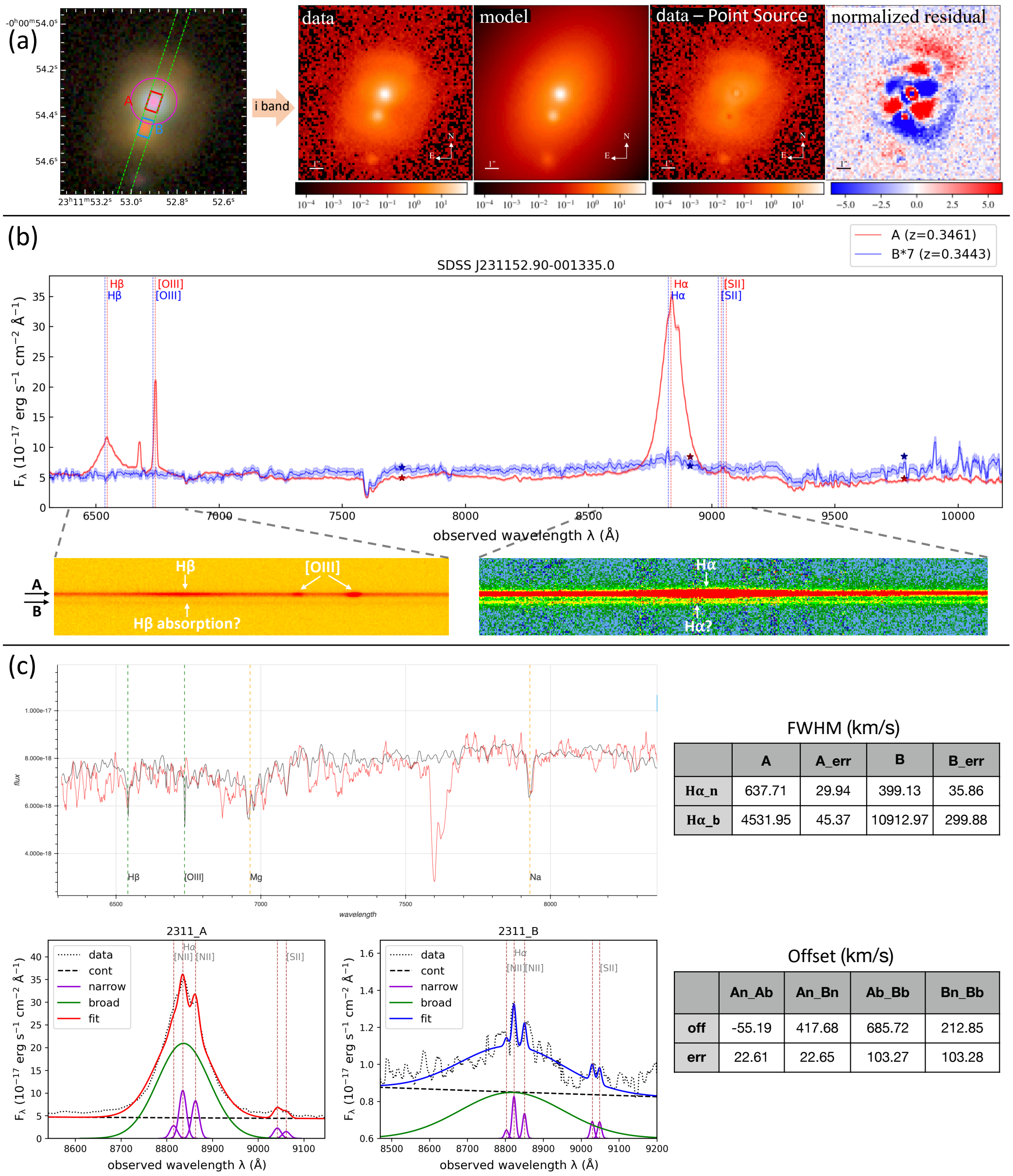


FWHM (km/s)

| | A | A_err | B | B_err |
|---|---|---|---|---|
| Hα_n | 637.71 | 29.94 | 399.13 | 35.86 |
| Hα_b | 4531.95 | 45.37 | 10912.97 | 299.88 |

Offset (km/s)

| | An_Ab | An_Bn | Ab_Bb | Bn_Bb |
|---|---|---|---|---|
| off | -55.19 | 417.68 | 685.72 | 212.85 |
| err | 22.61 | 22.65 | 103.27 | 103.28 |

Fig. 3.15: A kaleidoscope of J2311. Panel (a): image information of the HSC data and decomposition. Panel (b): 1D and 2D spectrum information. Panel (c): Supplementary information, the line fitting results and parameters.

# Chapter 4

# Detailed Physical Properties

## 4.1 Broad Line Region and Black Hole Mass Estimates

At least one broad emission line is included in the spectrum of each confirmed dual quasar system. This helps us to identify whether the source has AGN activity and to estimate the BH mass using the viral method [20]. Among our dual candidates (including the projected one), 5 pairs have $H\beta$ estimation, 5 have $H\alpha$ estimation, 4 have Mg II, and 3 have C IV. We fit the lines using models described in section 3.2.1. Taking the output of line width (FWHM) and monochromatic luminosity from the best fit model, we apply equations 1.13, 1.14, 1.15, and 1.16 to estimate the black hole mass

In Figure 4.1, we plot the black hole mass for our sample as a function of the spectroscopic redshift. We indicate the values for both quasars in each dual quasar system and label them with the same colored symbol. To aid in matching the quasars, dashed lines are added to which also provide the value of the mass ratio of the two. For comparison, we also provide the values for the full SDSS quasar sample as indicated by the hexagons with a shading indicative of the number density. The comparison sample covers a redshift range from 0 to 4.0. The range in black hole mass is from 7.0 to 10.0. Histograms are added on top and on the right to further demonstrate the sampling of both mass and redshift. Our dual quasars appear to follow the distribution of the parent SDSS population. Uncertainties are calculated based on the propagation of error from line fitting with the python **uncertainty** package. When we have multiple estimations from different emission lines for a single pair, we take the average values. It is overlaid on [14]'s catalog in the logBH vs Redshift space.

We find that the SMBHs of our quasar pairs do not appear to be less

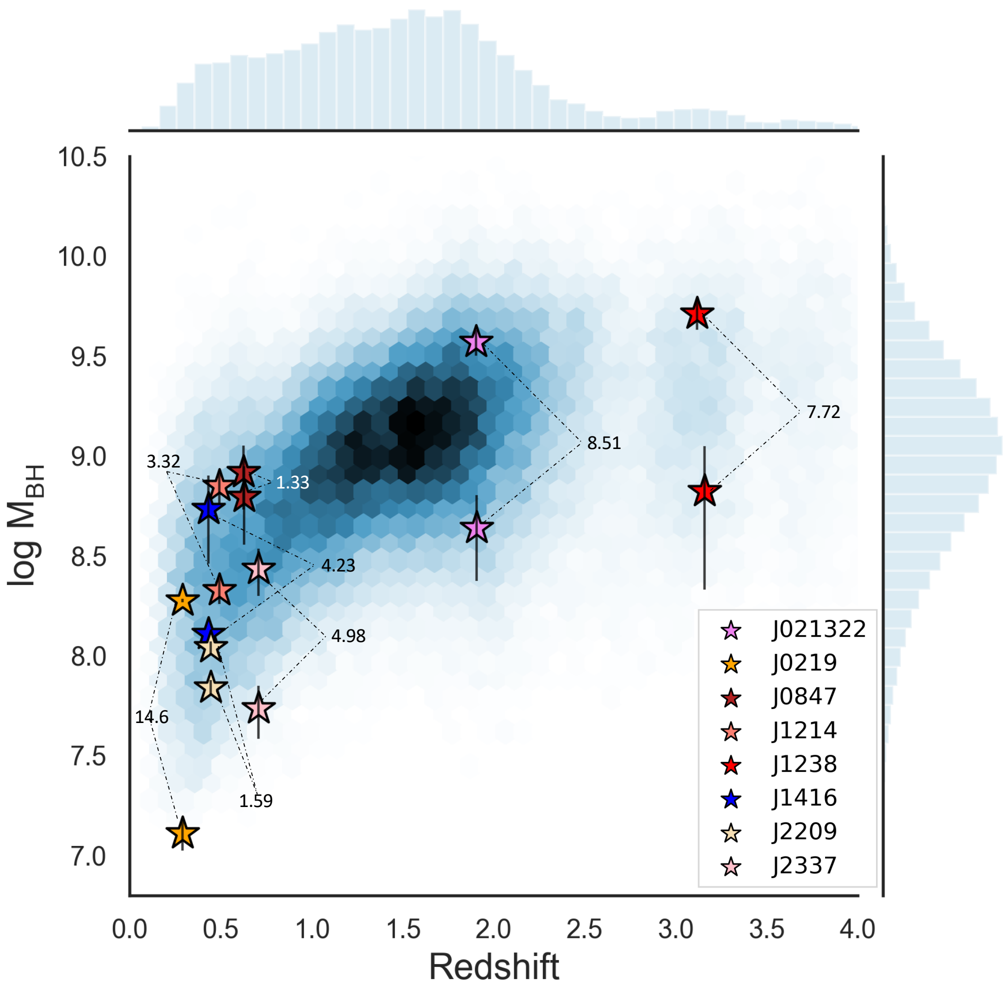


Fig. 4.1: Quasar pairs in black hole mass vs redshift space. The hexagons and histograms on the two sides show the distribution of the quasars in the DR7 quasar catalog [14]. The colors of the data points are set to imitate the real RGB color of the main sources in of pairs in HSC image, e.g. J1238 is a very red source, thus colored in red. But this is not a very precise notation, just for reference.

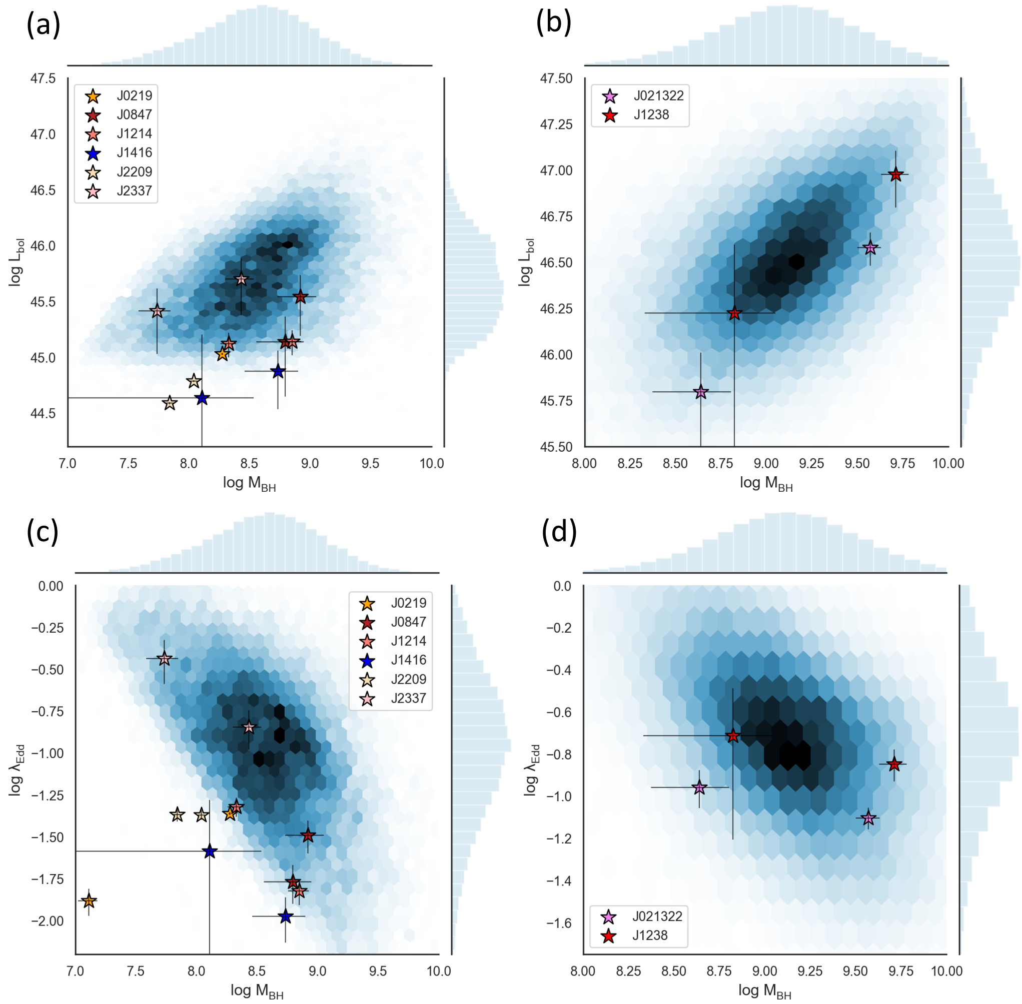


Fig. 4.2: Bolometric luminosity and Eddington ratio as a function of black hole mass in log scale. Panels (a) and (b) show the distribution of our quasar pairs in $L_{\rm bol} - M_{\rm BH}$ space, separated by $z <= 1$ and $z > 1$. So does the distribution of the histogram on the top and the 2D histograms representing [14]'s catalog for comparison. Our quasar pairs are plotted using the same markers as in Figure 4.1. The companion of J0219 is out of the range in panel (a), it is located at $\log M_{\rm BH} = 7.11$, $\log L_{\rm bol} = 43.34$. Panels (c) and (d) are the same targets and catalog plotted in $\lambda_{\rm edd} - M_{\rm BH}$ space.

massive than the single quasars. They spread rather averagely in SDSS DR7 catalog. The reason that most of these pairs locating at the low redshift ($z < 1$) region is an observational bias. As listed in Table 2.2, all our Keck targets are at low redshift. In FOCAS run, we separated our candidates into two groups to match the redshift with the grism coverage. The first night was for the low redshift candidates and the weather condition was good. The second night was for the high redshift candidates but the seeing was worse, leading to several unclassified cases. The Gemini run has no such bias but the total number is small. Therefore, the lack of quasar pairs at redshift between 1 and 3 in Figure 4.1 is possibly a observational bias.

Considering the mass ratio of the pairs, we find 5 out of 8 have black hole mass ratio within 5:1, and 3 out of 8 are larger than that. However, the mass measurements of the mergers with large BH mass ratios are somewhat problematic: For J0219, the one has the largest mass ratio 14.6, recall the line fitting result in figure 3.10, the existence of the broad component is uncertain, while our mass measurement assumes it was there. For J021322, the one with mass ratio of 8.51, is the source purely from SDSS, possibly suffering from contamination issues. For J1238, the one with mass ratio 7.72, is the quasar-BAL quasar pair, the mass measurement is based on C IV$\lambda$1549, which could be underestimated in source B due to the BAL feature. The mass ratio of J021322 and J1238 could also be real, supported by the explanation that at high redshift, the environment is gas richer, even less massive black holes can accrete enough matter onto itself to get activated.

In Figure 4.2, we plot the bolometric luminosity and Eddington ratio of our dual quasars as a function of black hole mass in the same fashion as Figure 4.1. The log scale of bolometric luminosity spreads from 44.2 to 47.5, while the log scale of Eddington ratio spreads from -2.2 to 0. The bolometric luminosity $L_{\rm bol}$ in the upper panel of Figure 4.2 is calculated using monochromatic luminosity and corresponding bolometric correction factors provided by [138] so that BC5100 = 9.26, BC3000 = 5.15, and BC1350 = 3.81. Eddington luminosity $L_{\rm edd}$ is estimated from BH mass via equation 1.8. The Eddington ratio is then calculated by $L_{\rm bol}/L_{\rm edd}$. We again provide the same full SDSS quasar samples as in Figure 4.1 in all panels of Figure 4.2 but separated at $z = 1$. Panels (a) and (c) include the low-redshift targets, (b) and (d) include the high-redshift ones. Compared to the distribution of the hexagons, we find that our low-redshift dual quasars tend to be fainter at the same level of black hole mass as single quasars. We suggest that they have not reach their maximum luminosity during the merger. Also, the Eddington ratios of such systems tend to be smaller, thus the SMBHs are growing moderately. For the high-redshift pairs, we don't see the bias clearly, possibly due to the small sample size. Recall the possible underestimation of

$M_{\rm BH}$ in some cases as mentioned in the discussion of Figure 4.1. This may shift the data points in the upper panels (a) and (b) to the left hand side, and shift the data points in the lower panels (c) and (d) to the upper-left side. Thus the data points in the upper panels of Figure 4.2 are upper limits for x-axis and in the lower panels, they are upper limits for x-axis and lower limit for the y-axis.

## 4.2 Stellar Mass and optical Color

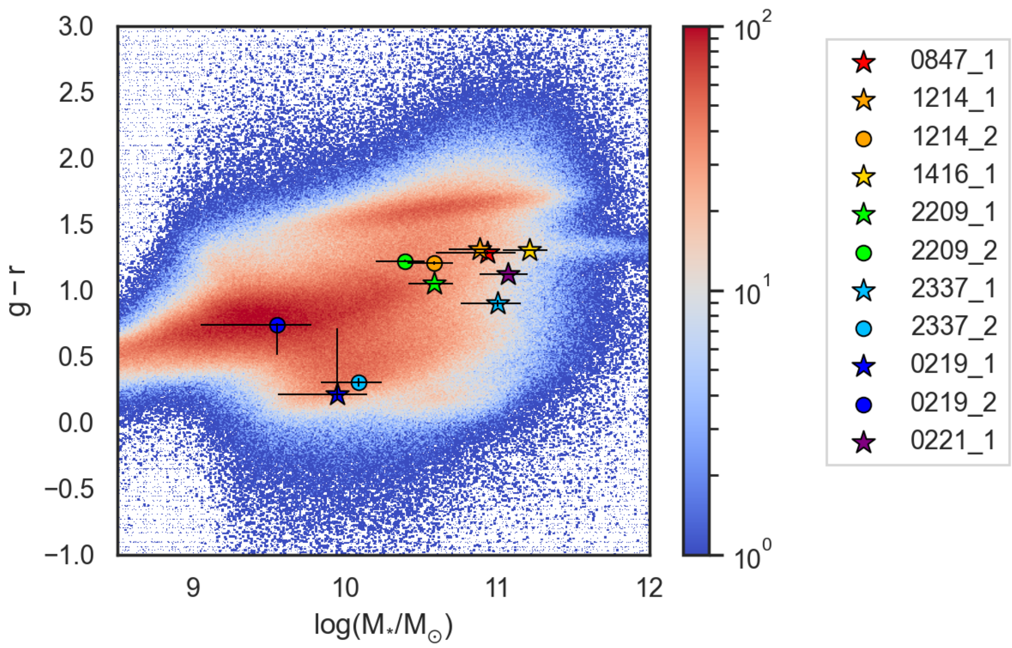


Fig. 4.3: Host galaxy properties of our dual quasar systems plotted in color-$M_*$ space. For those being modeled with two galaxy components, the star markers correspond to the primary source and the circular markers with the same color correspond to the companion. For those being modeled with one galaxy component, only the star markers are plotted. The density map shows a sample set of 2,173,627 normal galaxies selected from HSC catalog. The bins are set to be 438 × 500 for x- and y-axis. The color bar on the right hand side shows the density level.

Our decomposition algorithm returns five bands photometry magnitudes of the host galaxies of our dual quasar systems based on the model with Sérsic profiles (section 2.1.2). Our team carried out the stellar mass estimation for those systems at $z < 1$ using CIGALE (Code Investigating GALaxy Emission [139]) in python. It deals with the different physical processes in galaxies progressively, starting from the star formation history (SFH), then stellar emission, nebular emission, attenuation, dust emission (not included in our cases due to the lack of IR data), AGN emission (not included in our cases because we have already subtracted the point sources), finally generates a modelling SED to fit the magnitudes we provide and return the properties, including the mass of stars formed in the evolution.

We then plot the g - r color of the host galaxies of our dual quasars as a function of the stellar mass in Figure 4.3. The error is originally from the image analysis (y-axis), then transposed to the CIGALE program (x-axis). Recall that we modeled either one or two galaxy components for the pairs, the star markers represent the host galaxy of the main source , while the circular markers with the same color represent that of the secondary source if two galaxy components are applied. We provide a sample set of 2,173,627 normal galaxies selected from HSC as the overlaid density map for comparison. The density level is shown by the color bar. We find the host galaxies of our quasar pairs mostly belong to the massive galaxies, and bluer than red sequence galaxies in spite of how many galaxy components are modeled. Capelo et al. (2015) suggested in their simulation that the interaction of galaxies may trigger star formation in the merger stage ([6] Figure 1 and 2). This could possibly explain the bluer color of the host galaxies of our dual quasar systems.

## 4.3 BH-host Mass Correlation

As described in section 1.2.2, the correlation between the black hole and its host galaxy have been supported by many studies, but the reason for this remains mysterious. Studies such as [53, 54, 55] suggested that merger works as a global process to build up the correlation. If this is true, we should expect to see systems before merging have an offset from the correlation, then the mergers bring them onto that. Our estimation of both black hole mass and stellar mass based on the image decomposition enables us to test this hypothesis using our dual quasars, as they represent one scene during the merger. X.Ding et al. (2019) provided a fitting result to the $M_{\rm BH} - M_*$ correlation based on the data set of local AGNs:

$$\log\left(\mathrm{M_{BH}}/10^7\mathrm{M_\odot}\right) = 0.27 + 0.98\log\left(\mathrm{M_*}/10^{10}\mathrm{M_\odot}\right) \tag{4.1}$$

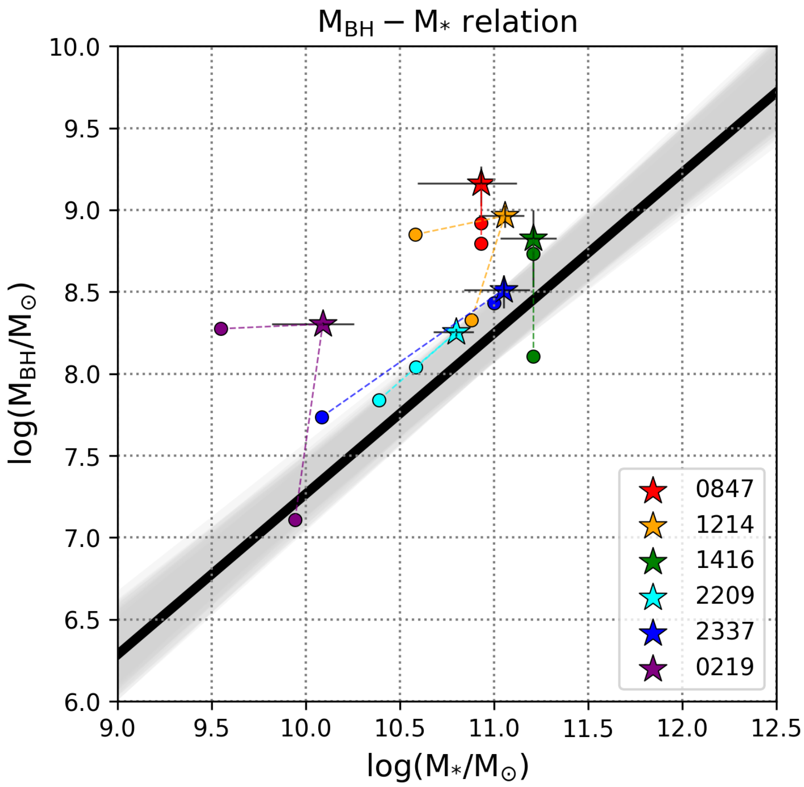


Fig. 4.4: Black hole mass versus stellar mass. The thick black line is the best fitting model from [15] figure 7, $1\sigma$ confidence interval is indicated by the grey region. Our dual quasars are plotted as colored dots, same color stand for sources in the same pair.

It is reproduced here in figure 4.4, the thick black line is the best fitting results to the local data (from [140, 42], not plotted here). The $1\sigma$ confidence interval is indicated by the grey region. Our quasar pairs are plotted as colored points. Dots with the same color stand for the separated two sources in a pair. They are summed up to the star marks indicating their possible final state after coalescence. In two cases: J0847 and J1416, we fitted only one Sérsic profile in the model, thus have only one measurement for the stellar mass. We take the same values for the separated sources (the dots). We found that our dual quasars basically follow the correlation, slightly above that line, so do their expected final stages after merger.

However, here we are just summing up the masses, do not consider the star formation and BH accretion during the future evolution of the system. Fortunately, simulations provide us traceable cases that could be analogues of

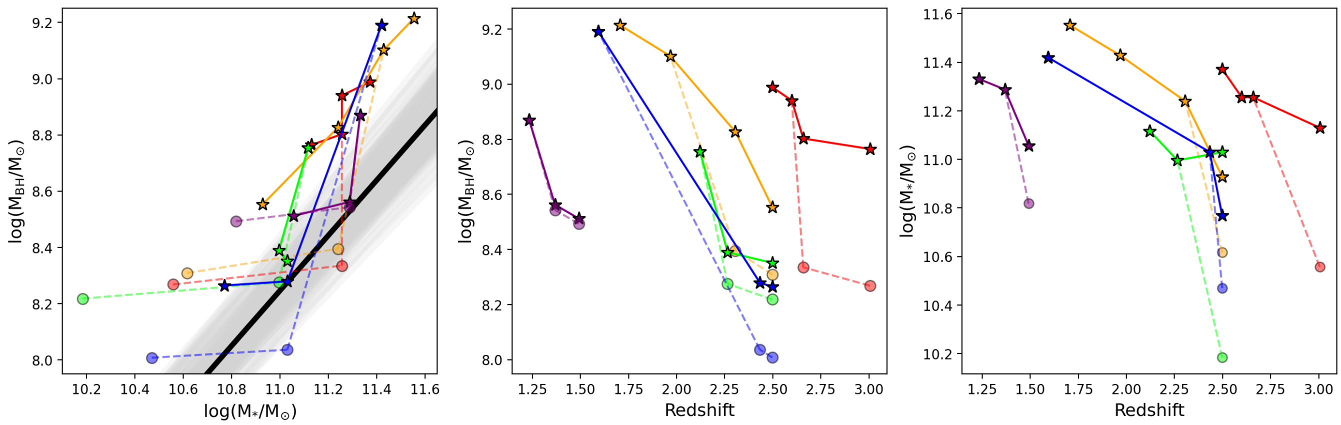


Fig. 4.5: Evolution traces of five AGN pairs obtained from Horizon simulation. Left panel: evolution of $M_{\rm BH} - M_*$ during the four stages of merger. One color stands for one pair. Star marks are the primary source of the pairs, connected with solid lines to show their evolution trajectories. Dot marks are the secondary source of the pairs, connected with dashed lines. The BHs form a unresolved binary at the third stage, after that, only the star marks are left. The thick solid black line is the same as that in figure 4.4. Middle panel: evolution of BH mass with redshift. Right panel: evolution of stellar mass with redshift.

our candidates. We obtained five AGN pairs from Horizon-AGN simulation by Volonteri, M. et al. [141] (introduced in section 1.3.1). The black hole mass and stellar mass are recorded in four stages in the merge scenario: starting from a stage when both sources are labeled as AGN but separated, at the second stage, the host galaxies merge first, then the BHs form a close SMBH binary, they become unresolved at this stage, thus the $M_{\rm BH}$ is the total mass of the pair. Finally they coalesce into one single source. The evolution trace of these five AGN pairs are plotted in Figure 4.5. In some cases, the final coalescence stage is very close to the SMBH binary stage, thus only three stages are visible. We found similar tendencies in the left panel of Figure 4.5 and in our results (Figure 4.4). No matter before or after the merger, most of the targets are located above the local correlation. This indicates that the BHs have already grown massive before the merge, which agree with the distribution of our data in figure 4.1. And the mergers do not bring them closer to the correlation, but further above that (compare the first stages and the final stages of the star marks). We may trace the evolution of the Horizon AGNs with redshift in Figure 4.5 middle and right panels.

We find that the mergers do lead to a boost in the BH mass (see where the dashed lines and solid lines merge), especially the blue one. However, the gain in stellar mass is not as dramatic. Even in one case (the green one), we see a decrease in stellar mass during the merger. We suggest that during the merger, the systems lost matter due to the interaction, while the central black holes do not get lighter. That is the reason why we see the mergers bring the AGN pairs above the local correlation.

# Chapter 5

# Conclusion

Dual quasars are very rare sources in literature. Especially those with separations closer than 30 kpc. However, they play an important role in constraining the simulation of galaxy mergers, unveiling the possible mechanism to form a quasar, explaining the gravitational wave background in nanohertz (nHz) band, and etc. In this thesis, we report our newest findings of a observational project searching for dual quasars using optical ground-based telescopes including SDSS, Keck, Subaru, and Gemini. We summarize the observational findings of this thesis as following:

- We utilized a method to systematically search for close separated ($0''.6-4''$) dual quasar candidates based on Subaru/HSC-SSP imaging data and viewed preliminary success (Section 2.1.2).
- We implemented a method to separate quasars from stars in the color-color diagram based on the distance to the stellar locus, and estimated the success rate in different regions of the color-distance diagram (Figure 3.4).
- We acquired spectroscopy data of 33 candidates, among which we discovered 7 physically associated quasar pairs (Table 2.2, Table 3.1, Section 3.2).
- We compared the color of our dual quasars to that of SDSS quasars, and found that these dual systems tend to be redder, which could be caused by dust extinction from the merger itself (Figure 3.6).

Based on observational data, we further carried out detailed analysis on the physical properties of our dual quasar systems:

- We estimated the BH mass of our dual quasars using the viral methods and found that they have already grown high and similar to the overall

SDSS BH mass population. Most of the pairs have comparable black hole masses (within 5:1), while the high-z pairs tend to have a larger ratio, which could be due to an underestimation of the mass or a gas richer environment (Figure 4.1).

- We estimated the bolometric luminosity and Eddington ratio of our dual quasars using monochromatic luminosity and bolometric correction factor. We found the pairs tend to be fainter and accrete more moderately than the single quasars in SDSS catalog (Figure 4.2).
- We estimated the stellar mass of the host galaxies of our dual quasars using CIGALE and compared that to normal galaxies. We found most of them represent massive galaxies bluer than the red sequence, which could be due to an increasing star forming activity (Figure 4.3).
- We estimated the $M_{\rm BH} - M_*$ correlation of our quasar pairs and compared to five quasar pairs selected from Horizon simulation. We found they agree with each other in that both reside above the local relationship no matter before or after merging. This indicates that the $M_{\rm BH} - M_*$ correlation is possibly not established via mergers as some studies suggested (Figure 4.4).

This thesis is still at an early stage of the project. More candidates will be followed up in the near future, also, multi-wavelength observation including X-ray and IR are under planning to study the confirmed pairs from different views. In the future, we expect to compare the dual fraction of our study to simulation works, estimate the impact of such systems on PTA/LISA signals, estimate the contribution of galaxy mergers to quasar activities, and study the detailed dynamics of the black holes and matter in such systems.

# Acknowledgement

This thesis is under the instruction of Prof. Hiroaki Aihara and Prof. John D. Silverman. I would like to show my greatest gratitudes to them. This work could not be finished without their supports. I also would like to thank to: My families, who give me spiritual and financial support on my life in Japan; Malte Scharamm, who offered a lot of help on the observation and data reduction; Xuheng Ding, who worked the decomposition on the images. Junyao Li, who helped on estimating the stellar mass; Andy Goulding and Tilman Hartwig, who provided the idea of applying machine learning strategies on sample selection; My friends and collegues in Kavli IPMU, ICRR and Aihara-Yokoyama lab for useful communications during this work.

# Bibliography


[1] H. Netzer, *The physics and evolution of active galactic nuclei.* Cambridge University Press, 2013.

[2] V. Beckmann and C. R. Shrader, "The agn phenomenon: open issues," *arXiv preprint arXiv:1302.1397*, 2013.

[3] A. Toomre and J. Toomre, "Galactic bridges and tails," *The Astrophysical Journal*, vol. 178, pp. 623–666, 1972.

[4] J. Kormendy and L. C. Ho, "Coevolution (or not) of supermassive black holes and host galaxies," *Annual Review of Astronomy and Astrophysics*, vol. 51, pp. 511–653, 2013.

[5] P. F. Hopkins, L. Hernquist, T. J. Cox, and D. Kereš, "A cosmological framework for the co-evolution of quasars, supermassive black holes, and elliptical galaxies. i. galaxy mergers and quasar activity," *The Astrophysical Journal Supplement Series*, vol. 175, no. 2, p. 356, 2008.

[6] P. R. Capelo, M. Volonteri, M. Dotti, J. M. Bellovary, L. Mayer, and F. Governato, "Growth and activity of black holes in galaxy mergers with varying mass ratios," *Monthly Notices of the Royal Astronomical Society*, vol. 447, no. 3, pp. 2123–2143, 2015.

[7] L. K. Steinborn, K. Dolag, J. M. Comerford, M. Hirschmann, R.-S. Remus, and A. F. Teklu, "Origin and properties of dual and offset active galactic nuclei in a cosmological simulation at," *Monthly Notices of the Royal Astronomical Society*, vol. 458, no. 1, pp. 1013–1028, 2016.

[8] A. De Rosa, C. Vignali, T. Bogdanović, P. R. Capelo, M. Charisi, M. Dotti, B. Husemann, E. Lusso, L. Mayer, Z. Paragi, *et al.*, "The quest for dual and binary supermassive black holes: A multi-messenger view," *New Astronomy Reviews*, p. 101525, 2020.

[9] Y. M. Rosas-Guevara, R. G. Bower, S. McAlpine, S. Bonoli, and P. B. Tissera, "The abundances and properties of dual agn and their host galaxies in the eagle simulations," *Monthly Notices of the Royal Astronomical Society*, vol. 483, no. 2, pp. 2712–2720, 2019.

[10] I. Pâris, P. Petitjean, É. Aubourg, A. D. Myers, A. Streblyanska, B. W. Lyke, S. F. Anderson, É. Armengaud, J. Bautista, M. R. Blanton, *et al.*, "The sloan digital sky survey quasar catalog: fourteenth data release," *Astronomy & Astrophysics*, vol. 613, p. A51, 2018.

[11] H. Aihara, Y. AlSayyad, M. Ando, R. Armstrong, J. Bosch, E. Egami, H. Furusawa, J. Furusawa, A. Goulding, Y. Harikane, *et al.*, "Second data release of the hyper suprime-cam subaru strategic program," *Publications of the Astronomical Society of Japan*, vol. 71, no. 6, p. 114, 2019.

[12] K. R. Covey, Ž. Ivezić, D. Schlegel, D. Finkbeiner, N. Padmanabhan, R. H. Lupton, M. A. Agüeros, J. J. Bochanski, S. L. Hawley, A. A. West, *et al.*, "Stellar seds from 0.3 to 2.5 $\mu$m: Tracing the stellar locus and searching for color outliers in the sdss and 2mass," *The Astronomical Journal*, vol. 134, no. 6, p. 2398, 2007.

[13] G. T. Richards, X. Fan, D. P. Schneider, D. E. V. Berk, M. A. Strauss, D. G. York, J. E. Anderson Jr, S. F. Anderson, J. Annis, N. A. Bahcall, *et al.*, "Colors of 2625 quasars at 0¡ z¡ 5 measured in the sloan digital sky survey photometric system," *The Astronomical Journal*, vol. 121, no. 5, p. 2308, 2001.

[14] Y. Shen, G. T. Richards, M. A. Strauss, P. B. Hall, D. P. Schneider, S. Snedden, D. Bizyaev, H. Brewington, V. Malanushenko, E. Malanushenko, *et al.*, "A catalog of quasar properties from sloan digital sky survey data release 7," *The Astrophysical Journal Supplement Series*, vol. 194, no. 2, p. 45, 2011.

[15] X. Ding, J. Silverman, T. Treu, A. Schulze, M. Schramm, S. Birrer, D. Park, K. Jahnke, V. N. Bennert, J. S. Kartaltepe, *et al.*, "The mass relations between supermassive black holes and their host galaxies at 1¡ z¡ 2 hst-wfc3," *The Astrophysical Journal*, vol. 888, no. 1, p. 37, 2020.

[16] E. Salpeter, "Accretion of interstellar matter by massive objects." *The Astrophysical Journal*, vol. 140, pp. 796–800, 1964.

[17] D. Lynden-Bell, "Galactic nuclei as collapsed old quasars," *Nature*, vol. 223, no. 5207, pp. 690–694, 1969.

[18] B. M. Peterson, I. Wanders, R. Bertram, J. F. Hunley, R. W. Pogge, and R. M. Wagner, “Optical continuum and emission-line variability of seyfert 1 galaxies,” *The Astrophysical Journal*, vol. 501, no. 1, p. 82, 1998.

[19] S. Kaspi, D. Maoz, H. Netzer, B. M. Peterson, M. Vestergaard, and B. T. Jannuzi, “The relationship between luminosity and broad-line region size in active galactic nuclei,” *The Astrophysical Journal*, vol. 629, no. 1, p. 61, 2005.

[20] M. Vestergaard and B. M. Peterson, “Determining central black hole masses in distant active galaxies and quasars. ii. improved optical and uv scaling relationships,” *The Astrophysical Journal*, vol. 641, no. 2, p. 689, 2006.

[21] A. Schulze, M. Schramm, W. Zuo, X.-B. Wu, T. Urrutia, J. Kotilainen, T. Reynolds, K. Terao, T. Nagao, and H. Izumiura, “Near-ir spectroscopy of luminous lobal quasars at 1¡ z¡ 2.5,” *The Astrophysical Journal*, vol. 848, no. 2, p. 104, 2017.

[22] N. Bennert, B. Jungwiert, S. Komossa, M. Haas, and R. Chini, “Size and properties of the narrow-line region in seyfert-2 galaxies from spatially-resolved optical spectroscopy,” *Astronomy & Astrophysics*, vol. 456, no. 3, pp. 953–966, 2006.

[23] A. Lawrence and M. Elvis, “Obscuration and the various kinds of seyfert galaxies,” *The Astrophysical Journal*, vol. 256, pp. 410–426, 1982.

[24] H. D. Curtis, “Descriptions of 762 nebulae and clusters photographed with the crossley reflector,” *Publications of Lick Observatory*, vol. 13, pp. 9–42, 1918.

[25] D. L. Meier, S. Koide, and Y. Uchida, “Magnetohydrodynamic production of relativistic jets,” *Science*, vol. 291, no. 5501, pp. 84–92, 2001.

[26] R. D. Blandford and R. L. Znajek, “Electromagnetic extraction of energy from kerr black holes,” *Monthly Notices of the Royal Astronomical Society*, vol. 179, no. 3, pp. 433–456, 1977.

[27] M. Rowan-Robinson, “On the unity of activity in galaxies,” *The Astrophysical Journal*, vol. 213, pp. 635–647, 1977.

[28] R. Antonucci, "Unified models for active galactic nuclei and quasars," *Annual review of astronomy and astrophysics*, vol. 31, pp. 473–521, 1993.

[29] A. Soltan, "Masses of quasars," *Monthly Notices of the Royal Astronomical Society*, vol. 200, no. 1, pp. 115–122, 1982.

[30] J. E. Barnes, "Evolution of compact groups and the formation of elliptical galaxies," *Nature*, vol. 338, no. 6211, pp. 123–126, 1989.

[31] F. Schweizer, "Colliding and merging galaxies," *Science*, vol. 231, no. 4735, pp. 227–234, 1986.

[32] J. E. Barnes and L. Hernquist, "Dynamics of interacting galaxies," *Annual review of astronomy and astrophysics*, vol. 30, no. 1, pp. 705–742, 1992.

[33] J. Kormendy and G. Illingworth, "Rotation of the bulge components of disk galaxies," *The Astrophysical Journal*, vol. 256, pp. 460–480, 1982.

[34] J. L. Sersic, "Atlas de galaxias australes," *Cordoba, Argentina: Observatorio Astronomico, 1968*, 1968.

[35] J. Kormendy, D. B. Fisher, M. E. Cornell, and R. Bender, "Structure and formation of elliptical and spheroidal galaxies," *The Astrophysical Journal Supplement Series*, vol. 182, no. 1, p. 216, 2009.

[36] A. Dressler and D. O. Richstone, "Stellar dynamics in the nuclei of m31 and m32-evidence for massive black holes?" *The Astrophysical Journal*, vol. 324, pp. 701–713, 1988.

[37] A. Dressler, "Observational evidence for supermassive black holes," in *Symposium-International Astronomical Union*, vol. 134. Cambridge University Press, 1989, pp. 217–232.

[38] D. Merritt and L. Ferrarese, "Black hole demographics from the $m_\bullet - \sigma$ relation," *Monthly Notices of the Royal Astronomical Society*, vol. 320, no. 3, pp. L30–L34, 2001.

[39] J. Kormendy and K. Gebhardt, "Supermassive black holes in nuclei of galaxies," *arXiv preprint astro-ph/0105230*, 2001.

[40] R. J. McLure and J. Dunlop, "On the black hole-bulge mass relation in active and inactive galaxies," *Monthly Notices of the Royal Astronomical Society*, vol. 331, no. 3, pp. 795–804, 2002.

[41] A. Marconi and L. K. Hunt, "The relation between black hole mass, bulge mass, and near-infrared luminosity," *The Astrophysical Journal Letters*, vol. 589, no. 1, p. L21, 2003.

[42] N. Häring and H.-W. Rix, "On the black hole mass-bulge mass relation," *The Astrophysical Journal Letters*, vol. 604, no. 2, p. L89, 2004.

[43] K. Gebhardt, R. Bender, G. Bower, A. Dressler, S. Faber, A. V. Filippenko, R. Green, C. Grillmair, L. C. Ho, J. Kormendy, *et al.*, "A relationship between nuclear black hole mass and galaxy velocity dispersion," *The Astrophysical Journal Letters*, vol. 539, no. 1, p. L13, 2000.

[44] L. Ferrarese and H. Ford, "Supermassive black holes in galactic nuclei: past, present and future research," *Space Science Reviews*, vol. 116, no. 3-4, pp. 523–624, 2005.

[45] K. Gültekin, D. O. Richstone, K. Gebhardt, T. R. Lauer, S. Tremaine, M. C. Aller, R. Bender, A. Dressler, S. Faber, A. V. Filippenko, *et al.*, "The m-$\sigma$ and ml relations in galactic bulges, and determinations of their intrinsic scatter," *The Astrophysical Journal*, vol. 698, no. 1, p. 198, 2009.

[46] A. Beifiori, S. Courteau, E. Corsini, and Y. Zhu, "On the correlations between galaxy properties and supermassive black hole mass," *Monthly Notices of the Royal Astronomical Society*, vol. 419, no. 3, pp. 2497–2528, 2012.

[47] N. J. McConnell and C.-P. Ma, "Revisiting the scaling relations of black hole masses and host galaxy properties," *The Astrophysical Journal*, vol. 764, no. 2, p. 184, 2013.

[48] J. Hu, "The black hole mass–stellar velocity dispersion correlation: bulges versus pseudo-bulges," *Monthly Notices of the Royal Astronomical Society*, vol. 386, no. 4, pp. 2242–2252, 2008.

[49] A. W. Graham, "Populating the galaxy velocity dispersion: Supermassive black hole mass diagram, a catalogue of (mbh, $\sigma$) values," *Publications of the Astronomical Society of Australia*, vol. 25, no. 4, pp. 167–175, 2008.

[50] J. Kormendy, R. Bender, and M. Cornell, "Supermassive black holes do not correlate with galaxy disks or pseudobulges," *Nature*, vol. 469, no. 7330, pp. 374–376, 2011.

[51] L. Hernquist, “Tidal triggering of starbursts and nuclear activity in galaxies,” *Nature*, vol. 340, no. 6236, pp. 687–691, 1989.

[52] T. Di Matteo, V. Springel, and L. Hernquist, “Energy input from quasars regulates the growth and activity of black holes and their host galaxies,” *nature*, vol. 433, no. 7026, p. 604, 2005.

[53] J. Silk and M. J. Rees, “Quasars and galaxy formation,” *arXiv preprint astro-ph/9801013*, 1998.

[54] A. Fabian, “The obscured growth of massive black holes,” *Monthly Notices of the Royal Astronomical Society*, vol. 308, no. 4, pp. L39–L43, 1999.

[55] A. King, “Black holes, galaxy formation, and the mbh-$\sigma$ relation,” *The Astrophysical Journal Letters*, vol. 596, no. 1, p. L27, 2003.

[56] S. M. Faber, S. Tremaine, E. A. Ajhar, Y.-I. Byun, A. Dressler, K. Gebhardt, C. Grillmair, J. Kormendy, T. R. Lauer, and D. Richstone, “The centers of early-type galaxies with hst. iv. central parameter relations,” *arXiv preprint astro-ph/9610055*, 1996.

[57] L. Lin, D. R. Patton, D. C. Koo, K. Casteels, C. J. Conselice, S. Faber, J. Lotz, C. N. Willmer, B. Hsieh, T. Chiueh, *et al.*, “The redshift evolution of wet, dry, and mixed galaxy mergers from close galaxy pairs in the deep2 galaxy redshift survey,” *The Astrophysical Journal*, vol. 681, no. 1, p. 232, 2008.

[58] S. Callegari, S. Kazantzidis, L. Mayer, M. Colpi, J. M. Bellovary, T. Quinn, and J. Wadsley, “Growing massive black hole pairs in minor mergers of disk galaxies,” *The Astrophysical Journal*, vol. 729, no. 2, p. 85, 2011.

[59] S. Van Wassenhove, P. R. Capelo, M. Volonteri, M. Dotti, J. M. Bellovary, L. Mayer, and F. Governato, “Nuclear coups: dynamics of black holes in galaxy mergers,” *Monthly Notices of the Royal Astronomical Society*, vol. 439, no. 1, pp. 474–487, 2014.

[60] P. F. Hopkins and L. Hernquist, “Fueling low-level agn activity through stochastic accretion of cold gas,” *The Astrophysical Journal Supplement Series*, vol. 166, no. 1, p. 1, 2006.

[61] P. F. Hopkins and E. Quataert, “How do massive black holes get their gas?” *Monthly Notices of the Royal Astronomical Society*, vol. 407, no. 3, pp. 1529–1564, 2010.

[62] S. J. Karl, T. Naab, P. H. Johansson, H. Kotarba, C. M. Boily, F. Renaud, and C. Theis, "One moment in time—modeling star formation in the antennae," *The Astrophysical Journal Letters*, vol. 715, no. 2, p. L88, 2010.

[63] R. Teyssier, D. Chapon, and F. Bournaud, "The driving mechanism of starbursts in galaxy mergers," *The Astrophysical Journal Letters*, vol. 720, no. 2, p. L149, 2010.

[64] J. D. Younger, P. F. Hopkins, T. Cox, and L. Hernquist, "The self-regulated growth of supermassive black holes," *The Astrophysical Journal*, vol. 686, no. 2, p. 815, 2008.

[65] P. H. Johansson, A. Burkert, and T. Naab, "The evolution of black hole scaling relations in galaxy mergers," *The Astrophysical Journal Letters*, vol. 707, no. 2, p. L184, 2009.

[66] S. L. Ellison, D. R. Patton, J. T. Mendel, and J. M. Scudder, "Galaxy pairs in the sloan digital sky survey–iv. interactions trigger active galactic nuclei," *Monthly Notices of the Royal Astronomical Society*, vol. 418, no. 3, pp. 2043–2053, 2011.

[67] J. Silverman, P. Kampczyk, K. Jahnke, R. Andrae, S. Lilly, M. Elvis, F. Civano, V. Mainieri, C. Vignali, G. Zamorani, *et al.*, "The impact of galaxy interactions on active galactic nucleus activity in zcosmos," *The Astrophysical Journal*, vol. 743, no. 1, p. 2, 2011.

[68] E. Treister, K. Schawinski, C. Urry, and B. D. Simmons, "Major galaxy mergers only trigger the most luminous active galactic nuclei," *The Astrophysical Journal Letters*, vol. 758, no. 2, p. L39, 2012.

[69] J. Gabor, C. D. Impey, K. Jahnke, B. Simmons, J. Trump, A. Koekemoer, M. Brusa, N. Cappelluti, E. Schinnerer, V. Smolčić, *et al.*, "Active galactic nucleus host galaxy morphologies in cosmos," *The Astrophysical Journal*, vol. 691, no. 1, p. 705, 2009.

[70] M. Cisternas, K. Jahnke, K. J. Inskip, J. Kartaltepe, A. M. Koekemoer, T. Lisker, A. R. Robaina, M. Scodeggio, K. Sheth, J. R. Trump, *et al.*, "The bulk of the black hole growth since z 1 occurs in a secular universe: no major merger-agn connection," *The Astrophysical Journal*, vol. 726, no. 2, p. 57, 2010.

[71] M. C. Begelman, R. D. Blandford, and M. J. Rees, "Massive black hole binaries in active galactic nuclei," *Nature*, vol. 287, no. 5780, p. 307, 1980.

[72] P. R. Capelo and M. Dotti, "Shocks and angular momentum flips: a different path to feeding the nuclear regions of merging galaxies," *Monthly Notices of the Royal Astronomical Society*, p. stw2872, 2016.

[73] J. E. Gunn and J. R. Gott III, "On the infall of matter into clusters of galaxies and some effects on their evolution," *The Astrophysical Journal*, vol. 176, p. 1, 1972.

[74] J. E. Barnes, "Formation of gas discs in merging galaxies," *Monthly Notices of the Royal Astronomical Society*, vol. 333, no. 3, pp. 481–494, 2002.

[75] Y. Gao, M. Zhu, and E. Seaquist, "Star formation across the taffy bridge: Ugc 12914/15," *The Astronomical Journal*, vol. 126, no. 5, p. 2171, 2003.

[76] S. Van Wassenhove, M. Volonteri, L. Mayer, M. Dotti, J. Bellovary, and S. Callegari, "Observability of dual active galactic nuclei in merging galaxies," *The Astrophysical Journal Letters*, vol. 748, no. 1, p. L7, 2012.

[77] L. Blecha, A. Loeb, and R. Narayan, "Double-peaked narrow-line signatures of dual supermassive black holes in galaxy merger simulations," *Monthly Notices of the Royal Astronomical Society*, vol. 429, no. 3, pp. 2594–2616, 2013.

[78] P. R. Capelo, M. Dotti, M. Volonteri, L. Mayer, J. M. Bellovary, and S. Shen, "A survey of dual active galactic nuclei in simulations of galaxy mergers: frequency and properties," *Monthly Notices of the Royal Astronomical Society*, vol. 469, no. 4, pp. 4437–4454, 2017.

[79] M. Tremmel, M. Karcher, F. Governato, M. Volonteri, T. Quinn, A. Pontzen, L. Anderson, and J. Bellovary, "The romulus cosmological simulations: a physical approach to the formation, dynamics and accretion models of smbhs," *Monthly Notices of the Royal Astronomical Society*, vol. 470, no. 1, pp. 1121–1139, 2017.

[80] M. Volonteri, Y. Dubois, C. Pichon, and J. Devriendt, "The cosmic evolution of massive black holes in the horizon-agn simulation," *Monthly*

*Notices of the Royal Astronomical Society*, vol. 460, no. 3, pp. 2979–2996, 2016.

[81] J. Surdej, H. Arp, E. Gosset, A. Kruszewski, J. Robertson, P. Shaver, and J.-P. Swings, “Further investigation of the pair of quasars q0107-025 a and b,” *Astronomy and Astrophysics*, vol. 161, pp. 209–216, 1986.

[82] C. Hazard, H. Arp, and D. Morton, “A compact group of four qsos with two appearing physically associated,” *Nature*, vol. 282, no. 5736, pp. 271–272, 1979.

[83] E. Burbidge, V. Junkkarinen, A. Koski, H. Smith, and A. Hoag, “A’cluster’of quasi-stellar objects near m82,” *The Astrophysical Journal*, vol. 242, pp. L55–L57, 1980.

[84] S. Djorgovski, R. Perley, G. Meylan, and P. McCarthy, “Discovery of a probable binary quasar,” *The Astrophysical Journal*, vol. 321, pp. L17–L21, 1987.

[85] G. Meylan, S. Djorgovski, N. Weir, and P. Shaver, “Phl 1222-an interacting quasar pair?” *The Messenger*, vol. 59, pp. 47–49, 1990.

[86] D. Crampton, T. Janson, P. Durrell, A. Cowley, and P. Schmidtke, “Quasar candidates in two extended cfht fields-1338+ 27 and 1639+ 40,” *The Astronomical Journal*, vol. 96, pp. 816–835, 1988.

[87] S. Komossa, V. Burwitz, G. Hasinger, P. Predehl, J. S. Kaastra, and Y. Ikebe, “Discovery of a binary active galactic nucleus in the ultraluminous infrared galaxy ngc 6240 using chandra,” *The Astrophysical Journal Letters*, vol. 582, no. 1, p. L15, 2002.

[88] S. Bianchi, M. Chiaberge, E. Piconcelli, M. Guainazzi, and G. Matt, “Chandra unveils a binary active galactic nucleus in mrk 463,” *Monthly Notices of the Royal Astronomical Society*, vol. 386, no. 1, pp. 105–110, 2008.

[89] P. J. Green, A. D. Myers, W. A. Barkhouse, J. S. Mulchaey, V. N. Bennert, T. J. Cox, and T. L. Aldcroft, “Sdss j1254+ 0846: a binary quasar caught in the act of merging,” *The Astrophysical Journal*, vol. 710, no. 2, p. 1578, 2010.

[90] J. Shangguan, X. Liu, L. C. Ho, Y. Shen, C. Y. Peng, J. E. Greene, and M. A. Strauss, “Chandra x-ray and hubble space telescope imaging of optically selected kiloparsec-scale binary active galactic nuclei. ii. host

galaxy morphology and agn activity," *The Astrophysical Journal*, vol. 823, no. 1, p. 50, 2016.

[91] M. Imanishi and Y. Saito, "Subaru adaptive-optics high-spatial-resolution infrared k-and l′ -band imaging search for deeply buried dual agns in merging galaxies," *The Astrophysical Journal*, vol. 780, no. 1, p. 106, 2013.

[92] S. Djorgovski, "Quasar pairs at large redshifts," *ASP Conference Series*, vol. 12, 1991.

[93] P. J. E. Peebles, *The large-scale structure of the universe.* Princeton university press, 1980.

[94] F. Hartwick and D. Schade, "The space distribution of quasars," *Annual review of astronomy and astrophysics*, vol. 28, no. 1, pp. 437–489, 1990.

[95] D. G. York, J. Adelman, J. E. Anderson Jr, S. F. Anderson, J. Annis, N. A. Bahcall, J. Bakken, R. Barkhouser, S. Bastian, E. Berman, *et al.*, "The sloan digital sky survey: Technical summary," *The Astronomical Journal*, vol. 120, no. 3, p. 1579, 2000.

[96] J. F. Hennawi, M. A. Strauss, M. Oguri, N. Inada, G. T. Richards, B. Pindor, D. P. Schneider, R. H. Becker, M. D. Gregg, P. B. Hall, *et al.*, "Binary quasars in the sloan digital sky survey: Evidence for excess clustering on small scales," *The Astronomical Journal*, vol. 131, no. 1, p. 1, 2006.

[97] J. F. Hennawi, A. D. Myers, Y. Shen, M. A. Strauss, S. Djorgovski, X. Fan, E. Glikman, A. Mahabal, C. L. Martin, G. T. Richards, *et al.*, "Binary quasars at high redshift. i. 24 new quasar pairs at z 3-4," *The Astrophysical Journal*, vol. 719, no. 2, p. 1672, 2010.

[98] S. Eftekharzadeh, A. Myers, J. Hennawi, S. Djorgovski, G. Richards, A. Mahabal, and M. Graham, "Clustering on very small scales from a large sample of confirmed quasar pairs: does quasar clustering track from mpc to kpc scales?" *Monthly Notices of the Royal Astronomical Society*, vol. 468, no. 1, pp. 77–90, 2017.

[99] A. L. Coil, A. J. Mendez, D. J. Eisenstein, and J. Moustakas, "Primus+ deep2: The dependence of galaxy clustering on stellar mass and specific star formation rate at 0.2¡ z¡ 1.2," *The Astrophysical Journal*, vol. 838, no. 2, p. 87, 2017.

[100] M. Masjedi, D. W. Hogg, R. J. Cool, D. J. Eisenstein, M. R. Blanton, I. Zehavi, A. A. Berlind, E. F. Bell, D. P. Schneider, M. S. Warren, *et al.*, "Very small scale clustering and merger rate of luminous red galaxies," *The Astrophysical Journal*, vol. 644, no. 1, p. 54, 2006.

[101] I. Zehavi, Z. Zheng, D. H. Weinberg, M. R. Blanton, N. A. Bahcall, A. A. Berlind, J. Brinkmann, J. A. Frieman, J. E. Gunn, R. H. Lupton, *et al.*, "Galaxy clustering in the completed sdss redshift survey: The dependence on color and luminosity," *The Astrophysical Journal*, vol. 736, no. 1, p. 59, 2011.

[102] Z. Zhai, J. L. Tinker, C. Hahn, H.-J. Seo, M. R. Blanton, R. Tojeiro, H. O. Camacho, M. Lima, A. C. Rosell, F. Sobreira, *et al.*, "The clustering of luminous red galaxies at z \\$sim$0.7 from eboss and boss data," *arXiv preprint arXiv:1607.05383*, 2016.

[103] I. Kayo and M. Oguri, "Very small scale clustering of quasars from a complete quasar lens survey," *Monthly Notices of the Royal Astronomical Society*, vol. 424, no. 2, pp. 1363–1371, 2012.

[104] X. Liu, J. E. Greene, Y. Shen, and M. A. Strauss, "Discovery of four kpc-scale binary active galactic nuclei," *The Astrophysical Journal Letters*, vol. 715, no. 1, p. L30, 2010.

[105] J. M. Comerford, K. Schluns, J. E. Greene, and R. J. Cool, "Dual supermassive black hole candidates in the agn and galaxy evolution survey," *The Astrophysical Journal*, vol. 777, no. 1, p. 64, 2013.

[106] J. M. Comerford, D. Pooley, R. S. Barrows, J. E. Greene, N. L. Zakamska, G. M. Madejski, and M. C. Cooper, "Merger-driven fueling of active galactic nuclei: Six dual and of agns discovered with chandra and hubble space telescope observations," *The Astrophysical Journal*, vol. 806, no. 2, p. 219, 2015.

[107] D. P. Schneider, G. T. Richards, P. B. Hall, M. A. Strauss, S. F. Anderson, T. A. Boroson, N. P. Ross, Y. Shen, W. N. Brandt, X. Fan, *et al.*, "The sloan digital sky survey quasar catalog. v. seventh data release," *The Astronomical Journal*, vol. 139, no. 6, p. 2360, 2010.

[108] D. J. Eisenstein, D. H. Weinberg, E. Agol, H. Aihara, C. A. Prieto, S. F. Anderson, J. A. Arns, É. Aubourg, S. Bailey, E. Balbinot, *et al.*, "Sdss-iii: Massive spectroscopic surveys of the distant universe, the milky way, and extra-solar planetary systems," *The Astronomical Journal*, vol. 142, no. 3, p. 72, 2011.

[109] I. Pâris, P. Petitjean, É. Aubourg, S. Bailey, N. P. Ross, A. D. Myers, M. A. Strauss, S. F. Anderson, E. Arnau, J. Bautista, *et al.*, "The sloan digital sky survey quasar catalog: ninth data release," *Astronomy & Astrophysics*, vol. 548, p. A66, 2012.

[110] I. Pâris, P. Petitjean, N. P. Ross, A. D. Myers, É. Aubourg, A. Streblyanska, S. Bailey, É. Armengaud, N. Palanque-Delabrouille, C. Yèche, *et al.*, "The sloan digital sky survey quasar catalog: twelfth data release," *Astronomy & Astrophysics*, vol. 597, p. A79, 2017.

[111] H. Aihara, N. Arimoto, R. Armstrong, S. Arnouts, N. A. Bahcall, S. Bickerton, J. Bosch, K. Bundy, P. L. Capak, J. H. Chan, *et al.*, "The hyper suprime-cam ssp survey: overview and survey design," *Publications of the Astronomical Society of Japan*, vol. 70, no. SP1, p. S4, 2017.

[112] S. Birrer and A. Amara, "lenstronomy: Multi-purpose gravitational lens modelling software package," *Physics of the Dark Universe*, vol. 22, pp. 189–201, 2018.

[113] J. Kennedy and R. Eberhart, "Particle swarm optimization," in *Proceedings of ICNN'95-International Conference on Neural Networks*, vol. 4. IEEE, 1995, pp. 1942–1948.

[114] J. B. Oke, J. G. Cohen, M. Carr, J. Cromer, A. Dingizian, F. H. Harris, S. Labrecque, R. Lucinio, W. Schaal, H. Epps, and J. Miller, "The keck low-resolution imaging spectrometer," *Publications of the Astronomical Society of the Pacific*, vol. 107, p. 375, apr 1995. [Online]. Available: https://doi.org/10.1086%2F133562

[115] N. Kashikawa, K. Aoki, R. Asai, N. Ebizuka, M. Inata, M. Iye, K. S. Kawabata, G. Kosugi, Y. Ohyama, K. Okita, T. Ozawa, Y. Saito, T. Sasaki, K. Sekiguchi, Y. Shimizu, H. Taguchi, T. Takata, Y. Yadoumaru, and M. Yoshida, "FOCAS: The Faint Object Camera and Spectrograph for the Subaru Telescope," *Publications of the Astronomical Society of Japan*, vol. 54, no. 6, pp. 819–832, 12 2002. [Online]. Available: https://doi.org/10.1093/pasj/54.6.819

[116] I. Hook, I. Jørgensen, J. Allington-Smith, R. Davies, N. Metcalfe, R. Murowinski, and D. Crampton, "The gemini–north multi-object spectrograph: Performance in imaging, long-slit, and multi-object spectroscopic modes," *Publications of the Astronomical Society of the Pacific*, vol. 116, no. 819, p. 425, 2004.

[117] P. G. Van Dokkum, "Cosmic-ray rejection by laplacian edge detection," *Publications of the Astronomical Society of the Pacific*, vol. 113, no. 789, p. 1420, 2001.

[118] D. E. Osterbrock, J. P. Fulbright, A. R. Martel, M. J. Keane, S. C. Trager, and G. Basri, "Night-sky high-resolution spectral atlas of oh and o2 emission lines for echelle spectrograph wavelength calibration," *Publications of the Astronomical Society of the Pacific*, vol. 108, no. 721, p. 277, 1996.

[119] D. E. Osterbrock, J. P. Fulbright, and T. A. Bida, "Night-sky high-resolution spectral atlas of oh emission lines for echelle spectrograph wavelength calibration. ii." *Publications of the Astronomical Society of the Pacific*, vol. 109, no. 735, p. 614, 1997.

[120] R. C. Bohlin, L. Colina, and D. S. Finley, "White dwarf standard stars: G191-b2b, gd 71, gd 153, hz 43," *The Astronomical Journal*, vol. 110, p. 1316, 1995.

[121] B. D. Team, "Bokeh: Python library for interactive visualization," 2014.

[122] P. C. Hewett and C. B. Foltz, "The frequency and radio properties of broad absorption line quasars," *The Astronomical Journal*, vol. 125, no. 4, p. 1784, 2003.

[123] J. A. Baldwin, M. M. Phillips, and R. Terlevich, "Classification parameters for the emission-line spectra of extragalactic objects." *Publications of the Astronomical Society of the Pacific*, vol. 93, no. 551, p. 5, 1981.

[124] L. J. Kewley, B. Groves, G. Kauffmann, and T. Heckman, "The host galaxies and classification of active galactic nuclei," *Monthly Notices of the Royal Astronomical Society*, vol. 372, no. 3, pp. 961–976, 2006.

[125] C. Cortes and V. Vapnik, "Support-vector networks," *Machine learning*, vol. 20, no. 3, pp. 273–297, 1995.

[126] G. T. Richards, D. E. V. Berk, T. A. Reichard, P. B. Hall, D. P. Schneider, M. SubbaRao, A. R. Thakar, and D. G. York, "Broad emission-line shifts in quasars: An orientation measure for radio-quiet quasars?" *The Astronomical Journal*, vol. 124, no. 1, p. 1, 2002.

[127] M. Vestergaard and B. J. Wilkes, "An empirical ultraviolet template for iron emission in quasars as derived from i zwicky 1," *The Astrophysical Journal Supplement Series*, vol. 134, no. 1, p. 1, 2001.

[128] P. Storey and C. Zeippen, "Theoretical values for the [o iii] 5007/4959 line-intensity ratio and homologous cases," *Monthly Notices of the Royal Astronomical Society*, vol. 312, no. 4, pp. 813–816, 2000.

[129] J. E. Greene and L. C. Ho, "A comparison of stellar and gaseous kinematics in the nuclei of active galaxies," *The Astrophysical Journal*, vol. 627, no. 2, p. 721, 2005.

[130] R. Lupton, M. R. Blanton, G. Fekete, D. W. Hogg, W. O ' Mullane, A. Szalay, and N. Wherry, "Preparing red-green-blue images from ccd data," *Publications of the Astronomical Society of the Pacific*, vol. 116, no. 816, p. 133, 2004.

[131] S. Birrer, A. Amara, and A. Refregier, "Gravitational lens modeling with basis sets," *The Astrophysical Journal*, vol. 813, no. 2, p. 102, 2015.

[132] A. Sonnenfeld, J. H. Chan, Y. Shu, A. More, M. Oguri, S. H. Suyu, K. C. Wong, C.-H. Lee, J. Coupon, A. Yonehara, *et al.*, "Survey of gravitationally-lensed objects in hsc imaging (sugohi). i. automatic search for galaxy-scale strong lenses," *Publications of the Astronomical Society of Japan*, vol. 70, no. SP1, p. S29, 2018.

[133] M. Tanaka, K. C. Wong, A. More, A. Dezuka, E. Egami, M. Oguri, S. H. Suyu, A. Sonnenfeld, R. Higuchi, Y. Komiyama, *et al.*, "A spectroscopically confirmed double source plane lens system in the hyper suprime-cam subaru strategic program," *The Astrophysical Journal Letters*, vol. 826, no. 2, p. L19, 2016.

[134] R. J. Weymann, S. L. Morris, C. B. Foltz, and P. C. Hewett, "Comparisons of the emission-line and continuum properties of broad absorption line and normal quasi-stellar objects," *The Astrophysical Journal*, vol. 373, pp. 23–53, 1991.

[135] F. Hamann, K. T. Korista, and S. L. Morris, "On the geometry, covering factor, and scattering-emission properties of qso broad absorption-line regions," *The Astrophysical Journal*, vol. 415, p. 541, 1993.

[136] R. Cid Fernandes, G. Stasińska, A. Mateus, and N. Vale Asari, "A comprehensive classification of galaxies in the sloan digital sky survey: how to tell true from fake agn?" *Monthly Notices of the Royal Astronomical Society*, vol. 413, no. 3, pp. 1687–1699, 2011.

[137] A. More, M. Oguri, I. Kayo, J. Zinn, M. A. Strauss, B. X. Santiago, A. M. Mosquera, N. Inada, C. S. Kochanek, C. E. Rusu, *et al.*, "The sdss-iii boss quasar lens survey: discovery of 13 gravitationally lensed quasars," *Monthly Notices of the Royal Astronomical Society*, vol. 456, no. 2, pp. 1595–1606, 2016.

[138] G. T. Richards, M. Lacy, L. J. Storrie-Lombardi, P. B. Hall, S. Gallagher, D. C. Hines, X. Fan, C. Papovich, D. E. V. Berk, G. B. Trammell, *et al.*, "Spectral energy distributions and multiwavelength selection of type 1 quasars," *The Astrophysical Journal Supplement Series*, vol. 166, no. 2, p. 470, 2006.

[139] M. Boquien, D. Burgarella, Y. Roehlly, V. Buat, L. Ciesla, D. Corre, A. Inoue, and H. Salas, "Cigale: a python code investigating galaxy emission," *Astronomy & Astrophysics*, vol. 622, p. A103, 2019.

[140] V. N. Bennert, M. W. Auger, T. Treu, J.-H. Woo, and M. A. Malkan, "The relation between black hole mass and host spheroid stellar mass out to z  2," *The Astrophysical Journal*, vol. 742, no. 2, p. 107, 2011.

[141] M. Volonteri, H. Pfister, R. S. Beckman, Y. Dubois, M. Colpi, C. J. Conselice, M. Dotti, G. Martin, R. Jackson, K. Kraljic, *et al.*, "Black hole mergers from dwarf to massive galaxies with the newhorizon and horizon-agn simulations," *arXiv preprint arXiv:2005.04902*, 2020.